8-2018

Flow Modeling of Synthetic Pitch Extrusion through Spinnerets for Continuous Fibers

Bushra Rahman
Clemson University, bushrar@g.clemson.edu

FLOW MODELING OF SYNTHETIC PITCH EXTRUSION THROUGH SPINNERETS FOR CONTINUOUS FIBERS

A Thesis
Presented to
the Graduate School of
Clemson University

In Partial Fulfillment
of the Requirements for the Degree
Master of Science
Chemical Engineering

---

by
Bushra Rahman
August 2018

Accepted by:
Dr. Amod A. Ogale, Committee Chair
Dr. Douglas Hirt
Dr. Christopher L. Cox

ABSTRACT

The understanding of precursor flow profiles during melt spinning is a step towards producing desirable carbon fibers for structural applications from mesophase pitch. During the melt spinning process, flow during extrusion determines the cross-sectional fiber microstructure, which is crucial to carbon fiber strength. The subsequent fiber draw down is not known to alter the microstructure within the cross section. Also, prior modeling studies have varied fluid complexity but have not examined the details of spinneret geometry, such as a filter in the counterbore and capillary placement. Therefore, this study aimed to investigate fluid behavior during the extrusion component of melt spinning, through geometrically complex spinnerets.

Modeling was conducted using finite element analysis (FEA) software package, ANSYS, version 17.0. The geometries and meshes were constructed with the Design Modeler module, whereas material and boundary conditions were established on the Polyflow solver. This study was initiated by validating the modeling protocol with prior literature results [Kundu and Ogale 2006] on AR-HP mesophase pitch rheology data on the ACER rheometer. Good agreement was observed between ANSYS and experimental viscosities, with a 7-14% difference in a Newtonian viscosity and a 0.1 - 5% difference in fitted Power Law models. For complex spinneret geometries, the Newtonian model was used to represent the fluid, since it approximates the viscosity of mesophase pitch under steady state conditions.

The geometry graduated to modeling batch melt spinning equipment, comprised of a barrel/plunger assembly and a spinneret, consisting of a counterbore and capillary,

and was examined across various barrel diameters. This comparison assessed the impact that the degree of transition from barrel to counterbore has on resulting flow fields and profiles. Smoother transition barrel to counterbore led to smaller vortex formations, as well as enhancing computational accuracy. With the addition of the filter at the barrel exit, pressure drop from barrel to counterbore exit showed an approximately 30% increase. However, no visible impact was noted on capillary pressure drop. Also because of this additional contraction, vortices were formed at the upper corners of the counterbore. Since an overall good agreement between ANSYS and analytical predictions was observed, a more complex geometry was examined.

Spinnerets with multiple off-center capillaries, with respect to the counterbore, was also modeled. This geometry was of interest since machining imprecision leads to counterbore-capillary eccentricity. Thus, simulations were conducted at various inter-capillary distances. Wider inter-capillary distances (i.e. wider distance from counter center) resulted in more pronounced flow division, leading to larger area of vortex formation.

DEDICATION

This work is dedicated to my family, who loved and supported me unconditionally.

ACKNOWLEDGMENTS

I would like to extend my gratitude to the following individuals, without whom this work could not have been completed.

Firstly, I would like to thank my advisor Dr. Ogale for his invaluable guidance and encouragement towards the successful completion of this project. I also thank him for fostering a stimulating and supportive workplace culture in his research group. I must also express my appreciation towards everyone in the group. Thank you to Dr. Sam Lukubira, Dr. Steve Tang, Dr. Tugba Demir, Ozgun Ozdemir, Jing Jin, Victor Bermudez, and Sagar Kanhere, for their friendship and support. I would like to especially thank Sam and Victor for helping me understand the experimental set ups I modeled, as well as Ozgun for helping me learn the ropes on ANSYS Polyflow. I must also single out our undergraduate, Caroline Christopher, for the immense help she provided with separate concurrent work.

I would like to thank Dr. Hirt and Dr. Cox for agreeing to serve on my committee and for their feedback to this work. I would also like to thank Bill Coburn for all of his technical assistance and Joy, Terri, Diana for their administrative help and support throughout my time in the ChBE department.

Finally, I would like to thank my friends and family for all their support and friendship. Thanks to my incoming ChBE graduate class of 2015 and the Bangladeshi Association of Clemson (BAC) for bringing fun to my time in Clemson. Special thanks is given to Mr. Darnell Oglesby and Ms. Sylvia Cole for their valuable help in settling in at Clemson.

There are not enough words to thank my parents for their unconditional love and support. Without their presence, I could not have kept my spirits up through the unpredictable nature of research (and life). I would also like to thank my brother, Tawhid and my sister-in-law Katie for their valuable support; and of course my nephews Ilyas and Yusha for their precious smiles.

Above all, I give my thanks to God, the Almighty, for all the blessings He has provided me.

TABLE OF CONTENTS

LIST OF TABLES

LIST OF FIGURES

Figure Page

LIST OF EQUATIONS

CHAPTER 1
INTRODUCTION

1.1 Carbon Fiber Overview

Carbon fibers exhibit outstanding strength, stiffness, thermal, and electrical properties, which enable their use as a reinforcing agent in a wide array of applications in the automotive, aerospace, sporting goods industries, and energy storage [Matsumoto, T. (1985); Arai, Y. (1993); Morgan, P. (2005); Yang, K.S. (2014)]. Compared to steel, carbon fibers possess over twice the maximum tensile strength and modulus, at a quarter of steel's density (Table 1.1).

Table 1.1: Comparison of Mechanical Properties between Carbon Fibers and Steel [Fitzer, E.; Manocha, L. M (1998)]

	Tensile Strength (GPa)	**Modulus (GPa)**	**Density (g/m^3)**
Steel	0.4-2.7	210-400	7.9
Carbon Fiber	3.0-7.0	250-700	1.75-2.15

However, since carbon does not melt, fibers must be produced from a solution- or melt-processable polymeric precursors. These polymeric precursor fibers are crosslinked into their thermoset equivalent through a step called "stabilization". Finally, carbon fibers are obtained from stabilized fibers, by carbonization above 1000 °C (Figure 1.1).

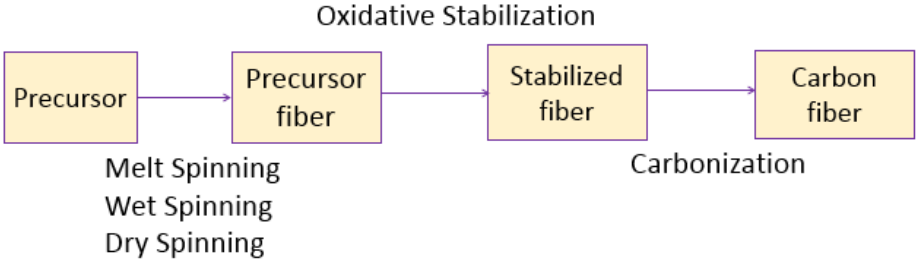

Figure 1.1: Carbon fiber manufacturing process flow chart

The most prevalent precursor is polyacrylonitrile (PAN), accounting for 90 % of global carbon fiber production [Liu, Y.; Kumar, S. (2012)]. PAN-based carbon fibers are costly due to the precursor itself, as well as the wet-spinning process that requires an expensive chemical bath. The search for high performance fibers from cheaper precursors spurred the development of mesophase pitch based carbon fibers [Edie, D.D; Dunham, M.G 1989]. The main difference between PAN-and mesophase pitch-based carbon fibers lies in the spinning process. Fibers from the latter are produced by melt-spinning, which involves extrusion of the precursor melt through a spinneret, followed by stretching it down to a desired finer diameter [Matsumoto, T. 1985]. The mechanical properties are attributed to mesophase pitch having the distinct advantage of orienting during spinning, and then developing graphitic properties after heat treatment [Cato, A.D.; Edie, D.D, 2003 & 2005].

Although, superior electrical and thermal properties are observed in mesophase pitch-based carbon fibers, the average tensile strength for mesophase pitch-based precursors is lower than those of PAN-based carbon fibers [Matsumoto,T. (1985), Mochida,I. et al. (1993)]. The determining factor in carbon fiber strength is the microstructure formation when the pitch melt flows through the spinneret [Diefendorf, R.J (2000)]. Thus, developing an understanding of flow behavior during mesophase pitch extrusion is important to obtain carbon fibers with the desired microstructure and enhanced strength.

1.2 Mesophase Pitch Characteristics

Structure

Liquid Crystalline Behavior

Mesophase pitch is a polynuclear aromatic compound that possesses liquid crystalline behavior with optical anisotropy. It consists of a nematic phase, where discotic molecules have orientational, but no positional order [Singh, A.P 2000]. The uniaxial, discotic nature of mesophase pitch is represented by the schematic in Figure 1.2.

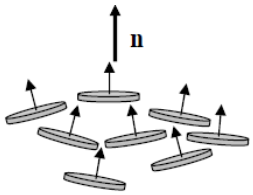

Figure 1.2: Uniaxial, discotic orientation of liquid crystals where n stands for the average orientation of the normals to each individual disc like molecules [Singh, A.P 2000]

Mesophase pitch is classified as a thermotropic material, where the orientational order of the molecules is dependent on temperature. If the temperature exceeds the isotropic-nematic transition, the increased kinetic energy in the components can lead to a phase transition, from a liquid crystal to an isotropic liquid. The thermotropic property of mesophase pitch is observed when it fuses into a melt and viscosity is lowered at high temperatures. Micrographs and diffraction patterns, by Nishizawa, Sakata [1991] showed optical anisotropy and stacking of aromatic planes were maintained. ^{13}C-NMR showed that aromatic alignment was retained [Mochida et al. 2000]. However, the nematic to

isotropic transition is not clearly observed in mesophase pitch because at elevated temperatures the hydrocarbon based pitch starts to disintegrate and begins to "coke".

Some studies have considered mesophase pitch lyotropic due to its composition of several species, with components possessing properties equivalent of solvents. Changing the concentration of low molecular weight species concentration is an important factor in modifying its properties as a carbon fiber precursor. Increasing the concentration of high molecular weight species, by vaporization, polymerization, and solvent extraction of low molecular weight species, can convert isotropic pitch to mesophase pitch [Rand, 1985; Hurt and Hu, 1999]. Sawa et al [1991] showed that by adding or removing small particles, respectively reduction and restoration of stacking of aromatic planes occurred [Mochida et al. 2000]. Stacking of the aromatic planes results in anisotropy observed in the mesophase pitch microstructure.

Components

Pitches usually consist of fractions of low molecular weight aliphatic components, low molecular weight naphthenic compounds, polar heterocyclic aromatics, and high molecular weight aromatic asphaltene. A high proportion of asphaltene is characteristic of most grades of spinnable pitch [Park, S.J; Hao, G.Y 2015].

Brooks and Taylor proposed the first model of mesophase pitch, comprising individual mesophase structures (nematic liquid crystals) of planar aromatic ring oligomers stacked in an approximately parallel manner. The aromatic sheets are perpendicularly arranged along the diameter of the spherical droplet formations the mesophase takes on after separating from the liquid isotropic phase. Mesophase pitch

was first observed during examination of heat-treated coal tar based isotropic pitch under an optical microscope with cross-polarized light. Optical anisotropy, arranged in a mosaic texture, was interspersed throughout the isotropic matrix. The optically anisotropic phase was defined as “mesophase”, i.e. part liquid and part crystalline (ordered). During treatment, mesophase initially separated out of the isotropic liquid as ordered spherical droplets, with layered aromatic sheets in a parallel array. Throughout heat treatment progression, spheres swelled and coalesced, forming bulk anisotropic mesophase [Brooks,J.D; Taylor,G.H ,1965, Mochida,I., Yoon, S.H.; Korai,Y., 2002; Castro, L.D.D ,2006].

Molecular weight and molecular weight distribution of mesophase pitches factor into the determination of their properties. The molecular weight of spinnable mesophase pitches depends on processing variables, such as hydrocarbon feedstock, and severity of processing conditions. Since mesophase pitch consists of a wide range of molecular constituents, ranging from no monomeric units to high aromaticity, no solvent can dissolve every constituent of spinnable mesophase pitch. Thus, an exact determination of molecular has been considered a difficult undertaking. Despite the hindrances in obtaining a comprehensive molecular characterization of mesophase pitch, numerous studies have been conducted to identify its constituents [Mochida, I. et al. 2002]. FD-mass spectrometry (MS) and MALDI spectra indicated that the molecular weight distribution for naphthalene-derived mesophase pitch ranges from 150 to 1500 a.mu. Based on the molecular weight distribution curve, it was suggested that the various

mesogen units (Figure 1.3) came from different starting materials [Mochida,I. et al. 2000; Mochida,I. et al. 2002] .

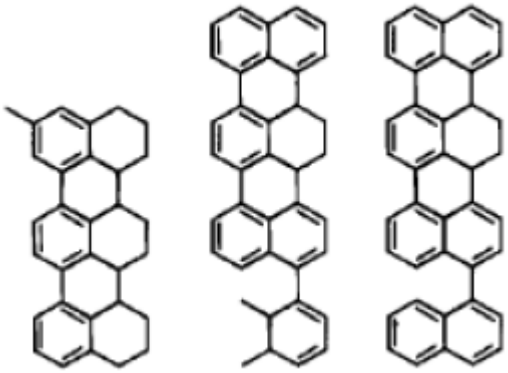

Figure 1.3: Typical mesogen units for naphthalene derived mesophase pitch [Mochida, I et al. 2000, 2002]

Kulkarni and Thies [2011] structurally characterized petroleum based pitches by separation of the pitch into oligomeric fractions vis dense gas extraction (DGE), followed by MALDI, MALDI-PSD, and FD-MS analysis. The dominant species were methylated derivatives of the polycyclic aromatic hydrocarbons (PAH) benzofluorene (216.4 m/z), chrysene, (228.3 m/z), benzofluoranthene (252.3 m/z), and their isomers.

The characteristics of aromatics, alkyl substituents, and naphthenic groups vary between different precursors of mesophase pitch. Coal tar and fluidized catalytic cracking decant oil (FCC-DO) derived pitches have a diverse composition of molecules, given the complex components in their feeds. FCC-DO pitches tend to be alkyl group rich, while coal tar pitch is highly aromatic. Synthetically produced mesophase pitches tend to inherit the aromatic structure of their precursors [Mochida, I. et al. 2002]

Production

Singer et al. from Union Carbide established a way to commercially produce higher mesophase content pitch, though extended heat treatment of petroleum, coal tar, and acenaphthylene from 350 to 500°C [Singer, L.S., 1975]. Throughout the duration of the heat treatment, mesophase spheres coalesced into a continuous phase. The pitches were heated in the presence of nitrogen to purge low molecular weight isotropic phase species. Due to reduction of low molecular weight species, it was concluded that better spinnability of mesophase pitch was observed. However, the long heat treatment time could not circumvent the excessive polymerization of larger anisotropic phase forming molecules at temperatures above 380°C. Thus, pitch had to be spun around 350°C, and even so, instability was observed during spinning due to pyrolysis [Mochida et al. 2000].

To concentrate a suitable fraction of mesophase from low aromatic content pitches, Diefendorf and Exxon introduced solvent extraction, where the lightest and heaviest fractions were removed [Mochida et al. 2000, 2002]. The heavy fraction is heat treated for about 10 minutes to temperatures ranging from 230 to 400°C [Yoon et. Al. 1994]. However, this approach posed issues with removing solvent residue, which made spinning difficult. For a more selective extraction of high molecular weight content, Thies and Cervo used dense gas extraction, with supercritical toluene as the solvent. This technique yielded a narrow molecular weight distribution for mesophase pitch [Cato, A.D.; Edie, D.D,2003]

The complexity of pitch from petroleum and coal tar was a hindrance to yielding high quality mesophase pitch, due to its composition of diverse hydrocarbons, with

varying reactivities and thermal properties. The level of purification needed to reduce fine particles of nano-scale contaminants such as coke, catalysts, and mineral particles is extremely costly [Mochida et al. 2000].

The alternative to producing pitches via heat treatment are synthetic methods, using catalysts. Mesophase pitch was prepared with high spinnability from naphthalene and ethylene tar, catalyzed by $AlCl_3$. The pitch was still heat treated after removing the catalyst, and retained a high level of naphthenic groups, accounting for a low softening point. The issue encountered with this technique is the difficulty in completely removing solid aluminum hydroxide and alumina residue. The presence of these solid particles led to defects and resulted in poor quality of carbon fibers. To address this problem, HF/BF_3 was used as a condensation catalyst to produce spinnable mesophase pitch. HF/BF_3 brings about protonated complexes of aromatic hydrocarbons, such as naphthalene. A dimer with two naphthenic hydrogens is produced when the complex attacks the aromatic molecule with the highest basicity. Condensation polymerization repeats, producing trimers to decamers with a mesophase yield above 90 weight percent. The catalyst is also easily recoverable through atmospheric distillation and can be recycled. Given the reduced cost and higher yield compared to using $AlCl_3$, this process has been commercialized [Mochida et al. 2000].

Rheology

The thermoplastic, liquid crystalline properties of mesophase pitch allow it to reach its softening point and flow around 250 to 350 °C, enabling spinnability. Thus, numerous studies have been conducted to study the rheology of various mesophase

pitches.

In naphthalene-based mesophase pitches, two- and three-region steady shear viscosities have been observed. Three-region behavior was seen in HF/BF_3 catalyzed naphthalene based pitch. In high shear rheology experiments, conducted by Yoon et al. [1994], the flow curves show initial shear thinning up to about 3000 s^{-1}, followed by a plateau, and then a high degree of shear thinning from 10,000 s^{-1} (Figure 1.4) [Yoon et al., 1994].

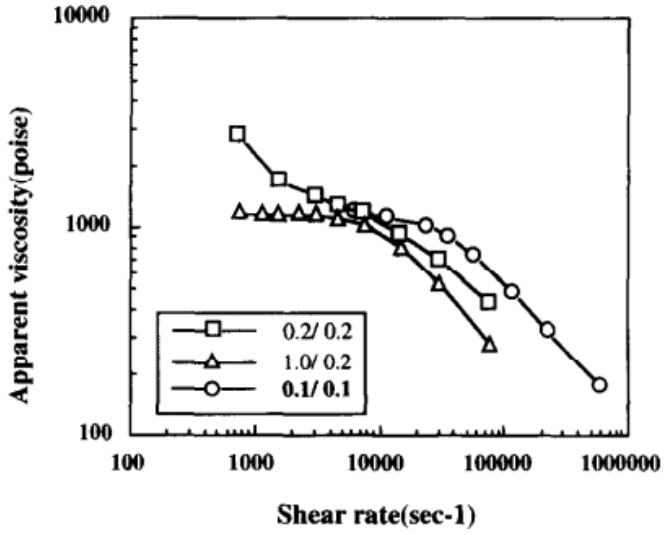

Figure 1.4: Three region viscosity behavior in NP1 naphthalene based mesophase pitch [Yoon et al., 1994]

For ARA24R naphthalene-derived mesophase pitch, the two-region curve showed strong shear thinning below 1 s^{-1} (Region I), followed by a constant viscosity (Region II). At the transition region, a kink was seen in the viscosity-shear rate curve (Figure 1.5a), which is accounted by a change in overall orientation of the poly-domain network. In the pre-kink, low shear region, the alignment of individual domains were mostly "edge-on".

At higher shear rates, the orientation transitioned to both edge-on and face on orientation, resulting in lower viscosities (Figure 1.5 b) [Cato, A.D.; Edie, D.D,2003]. The two-region behavior was confirmed with high shear rheology experiments, which demonstrated the region II plateau up to about 1000 s^{-1} [Cato, A.D.; Edie, D.D; Harrison, G.M. 2005].

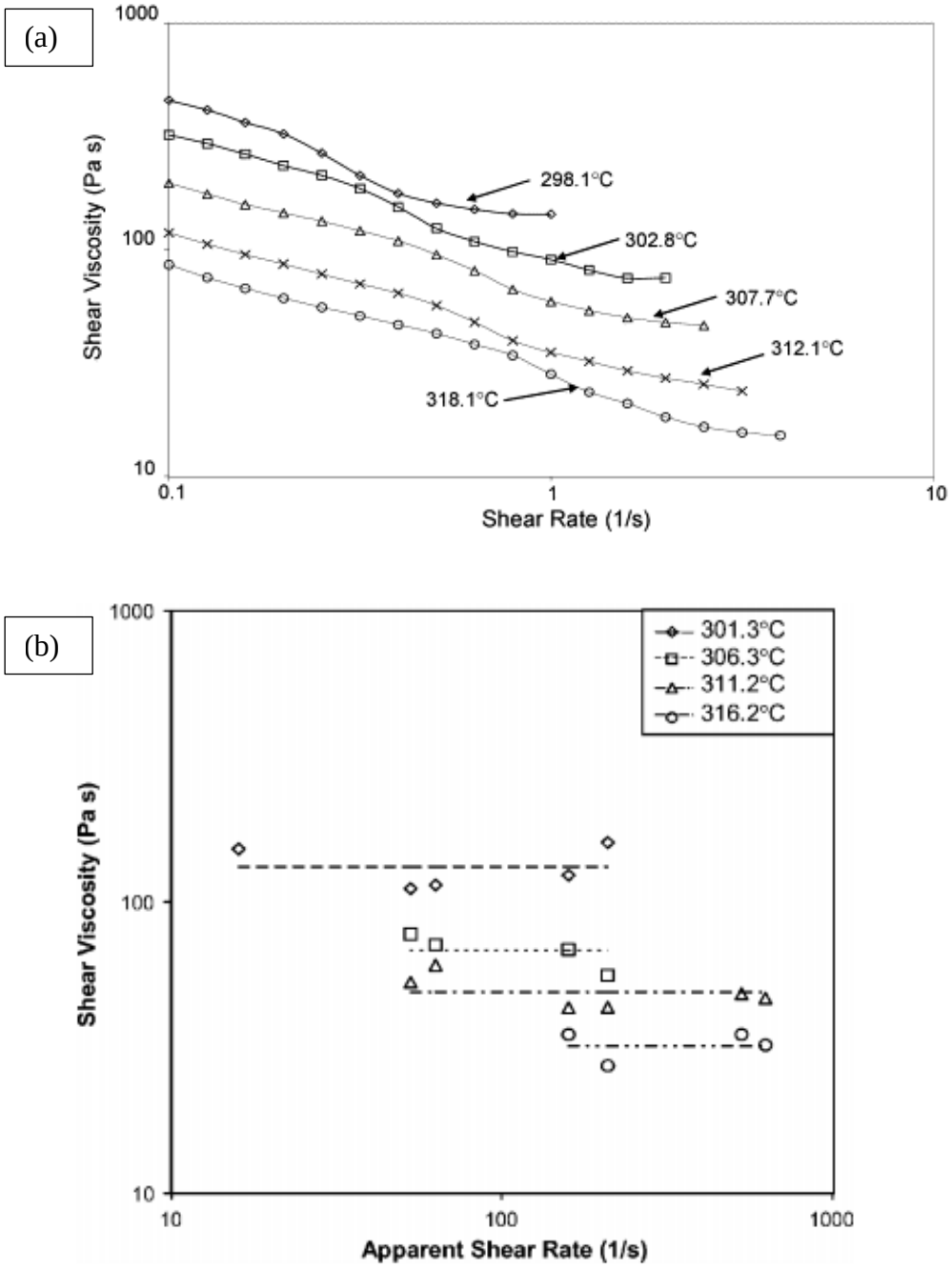

Figure 1.5: (a)Two region viscosity behavior in ARA24R from cone-plate rheometer [Cato, A.D.; Edie, D.D,2003] (b) high shear viscosity from capillary rheometer [Cato, A.D.; Edie, D.D; Harrison, G.M. 2005]

Kundu and Ogale reported [2006b] steady shear rheological studies on synthetically derived AR-HP mesophase pitch and observed two distinct regions in the viscosity-shear rate curves. Region I consisted of shear thinning, up to 2.5 s^{-1}, followed up by the Newtonian plateau in Region II, as displayed in Figure 1.6a. Within region I, a higher degree of shear thinning was observed in AR-HP, compared to ARA24R and ARA24. It was also demonstrated that the mesophase structure strongly affects viscosity at low shear rates. Once the domain structure has broken down, the mesophase pitch showed a fairly steady viscosity. After this "broken-down" structure was subjected to shearing, the lower viscosity was retained even at the low shear rates during ramp down (Figure 1.6b).

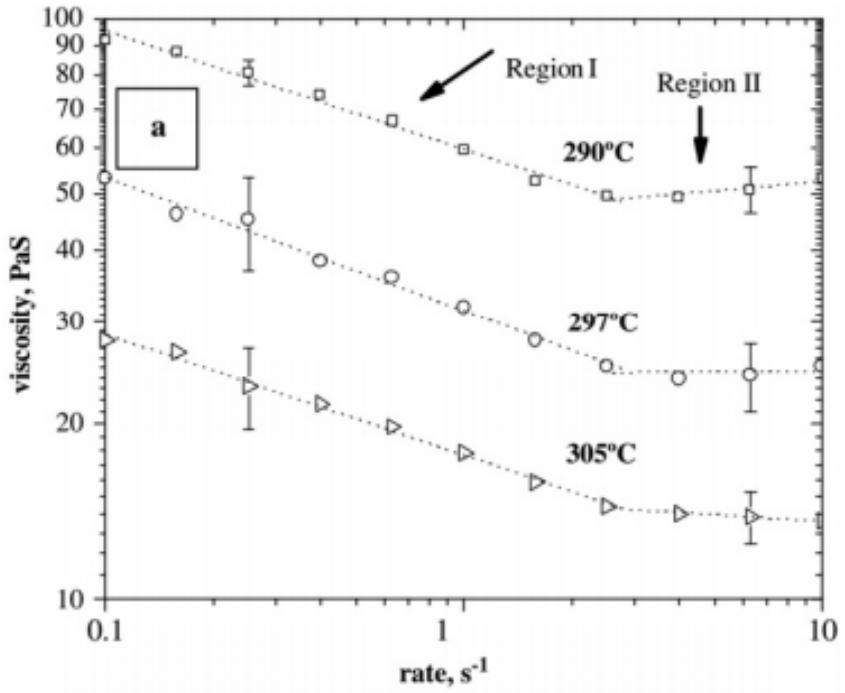

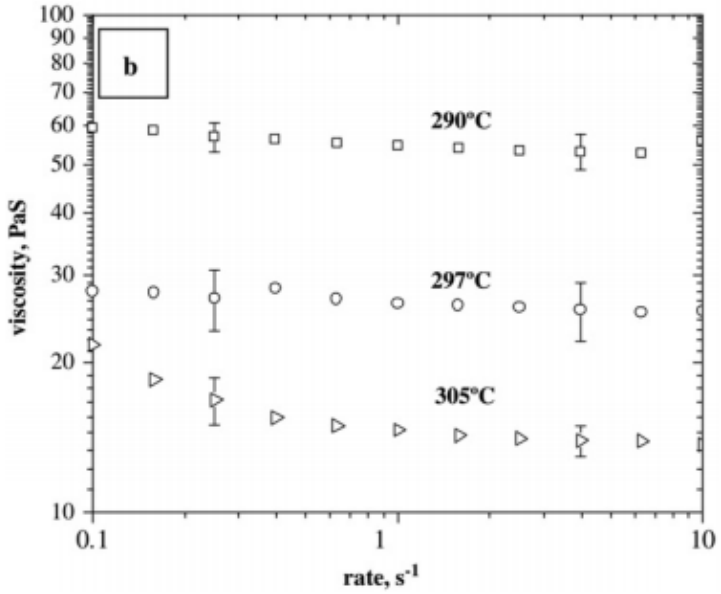

Figure 1.6: Steady shear viscosity cone-and-plate experiments in rate sweep mode at [Kundu,S; Ogale, A.A,2006 a &b] (a)increasing shear rates (b) decreasing shear rates

Further, as displayed in Figure 1.7, high shear rheology studies showed that apparent viscosities were not strongly dependent on shear rates. The lack of significant shear thinning is a consequence of the prior breakdown of liquid crystalline domains [Kundu,S; Ogale, A.A,2010] . Prior literature studies also note that molten mesophase pitch does not exhibit die-swell upon exiting a spinneret [Figueiredo, J.L.; Bernardo, C.A 1989]. This is consistent with the fact that there is no relaxation of the molecular order as the melt exits the die because the mesophase consists of disks, no long-chain polymers. Also, retaining orientational order in the die indicates the importance of studying flow behavior in fiber spinnerets. It should also be noted that, unlike polymer fibers, mesophase pitch fibers cannot be post-stretched.

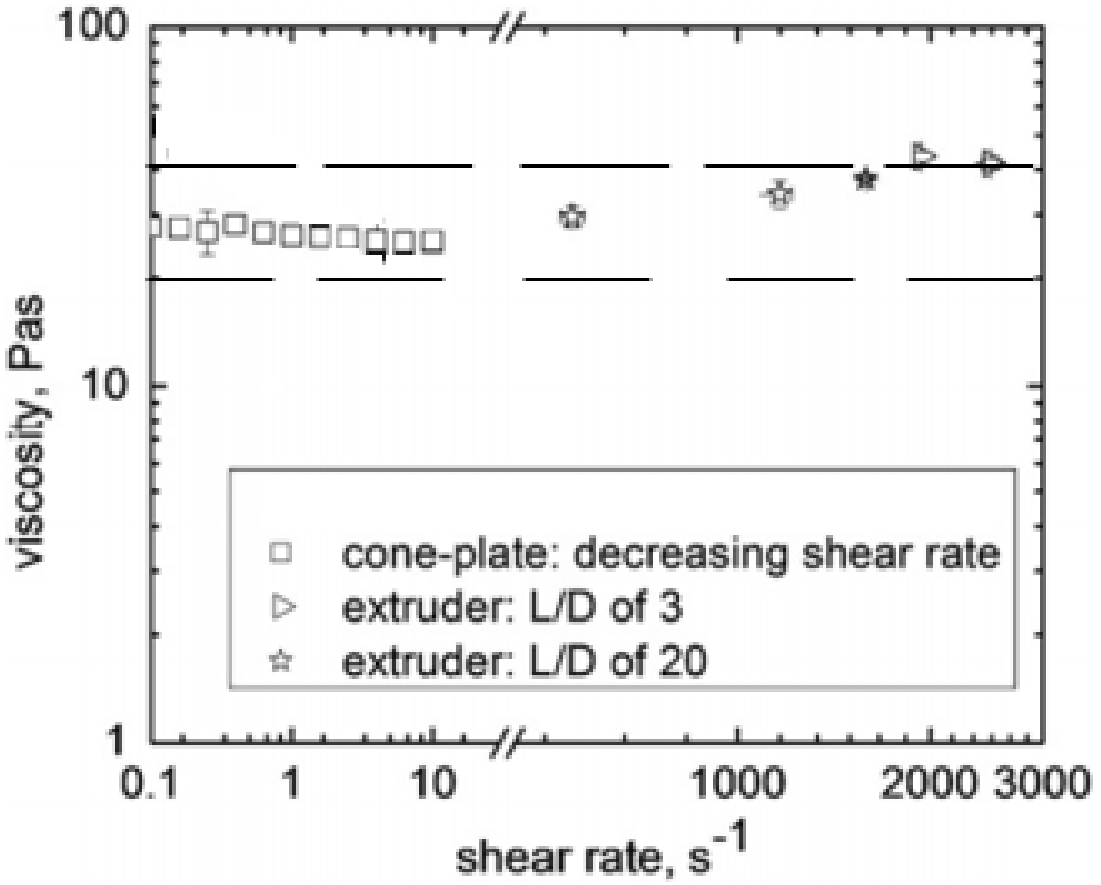

Figure 1.7: ARHP mesophase pitch viscosities as a function of shear rate. Low shear measurements were obtained from a cone-and-plate rheometer, while high shear viscosities were measured using a single screw extruder, with capillaries of 2 L/D ratios [Kundu,S; Ogale, A.A,2010]

In summary, at high shear rates such as those encountered during fiber extrusion, mesophase pitch does not display any die swell or any significant variation in its viscosity as a function of shear rate. Therefore, its flow behavior can be simplified as Newtonian. The near Newtonian behavior of mesophase pitch, after the breakdown of its domain structure, can be attributed to its low molecular weight between 150 to 1500 amu [Mochida,I. et al. 2000; Mochida,I. et al. 2002]. A small extent of shear thinning is also observed for some polymers. A comparison of two grades of polypropylene (with different molecular weights) both showed rapid shear thinning from 4 to 2000 s^{-1} (Figure 1.8a and b), with the lower molecular weight grade leading not only to lower viscosities but also weak shear thinning (Figure 1.8b) [Brandao,J. et al. 1996].

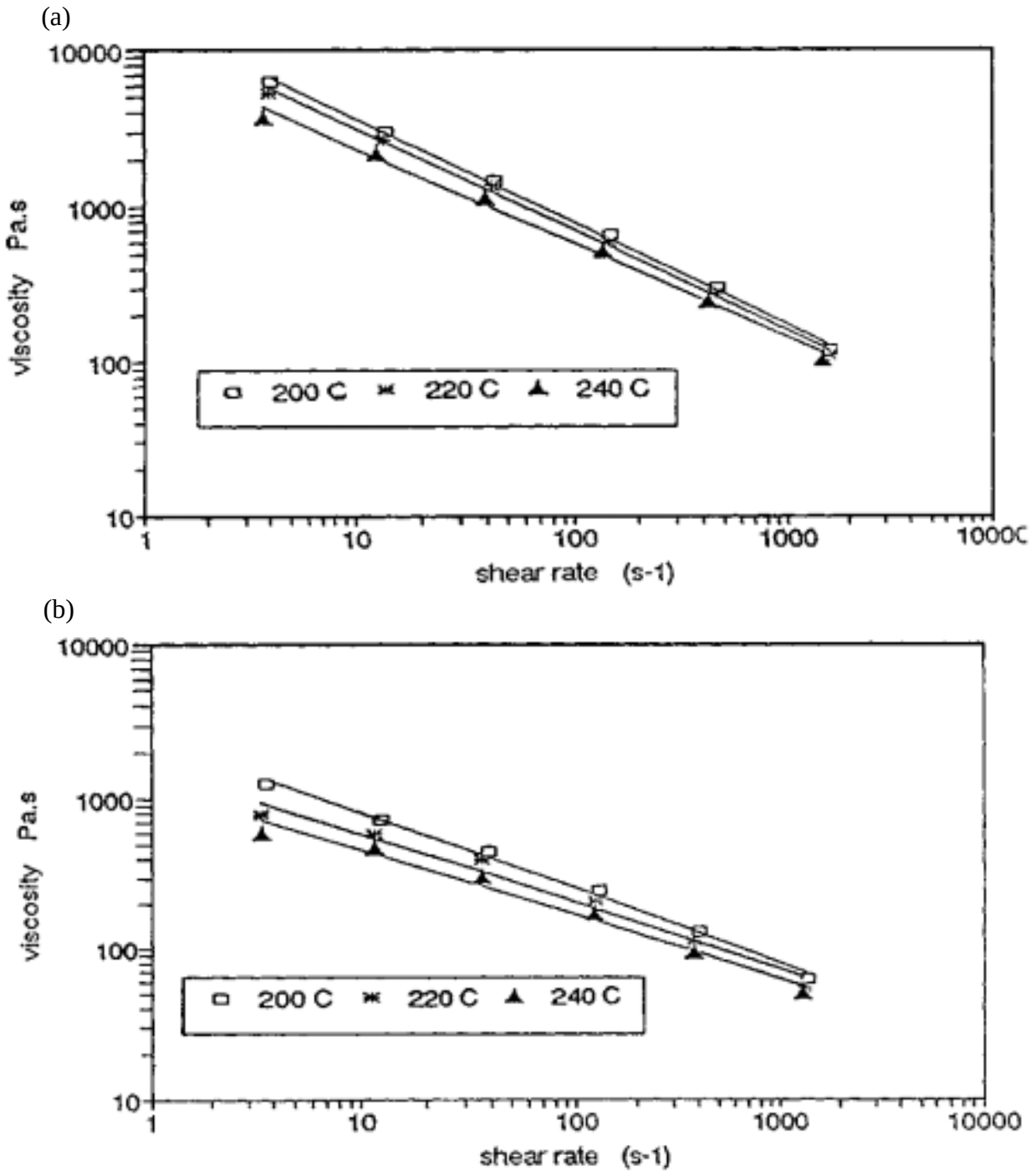

Figure 1.8: Viscosity-shear rate curves for (a) polypropylene weight average molecular weight= 503,000 (b) polypropylene weight average molecular weight= 254,000 [Brandao,J. et al. 1996].

Other lower molecular weight polymers, such as polyethylene terephthalate (PET), with weight average molecular weight = 82,000, have shown even lower viscosities and rate of shear thinning compared to that of polypropylene (Figure 1.9) [Jiang, Z. et al. 2014].

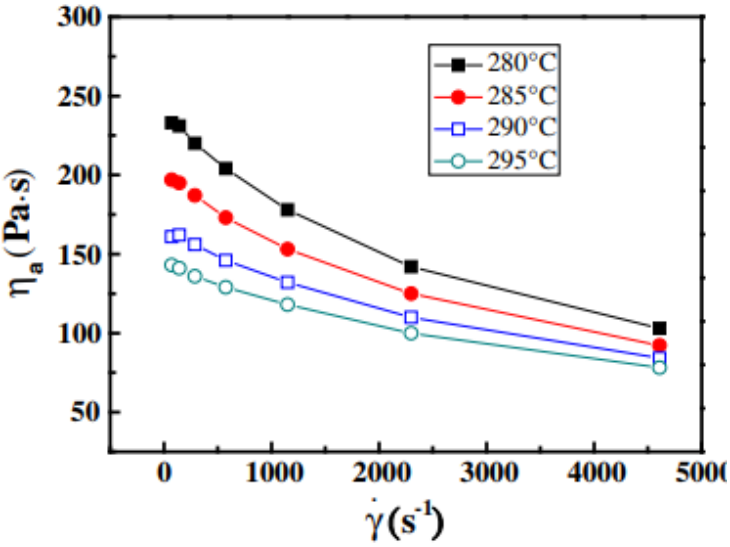

Figure 1.9: Viscosity-shear rate curves for PET [Jiang, Z. et al. 2014]

1.3 Mesophase-Pitch Based Carbon Fiber Production

In the melt spinning of mesophase pitch fibers, the solid precursor is heated to a molten state in a closed system, and then extruded through a spinneret. The spinning temperature needs to be closely regulated due to the high temperature dependence of mesophase pitch viscosity. Once the melt passes through the spinneret, it proceeds to be drawn and stretched to a smaller fiber diameter.

The mesophase pitch fibers have to undergo oxidative stabilization, below softening point, to prevent inter-fiber fusion, as well as preparing the pitch as-spun fibers to withstand the extreme conditions of carbonization. The fibers are subjected to

temperatures from 150-300°C in air for a period ranging from 3 to 30 hours. Unlike PAN-based fibers, mesophase pitch-based fibers do not need tension applied at the ends to ensure fiber axis alignment of molecules, since the alignment of disk-like molecules formed during extension does not relax during stabilization.

Following thermosetting, the oxidized fibers undergo carbonization, where at least 95% of non-carbon elements are removed in an inert environment. Pre-carbonization involves a gradual temperature ramp to reduce gas evolution rate. Carbonization is conducted at 1200-1500 °C and graphitization around 2400-3000 °C. With higher heat treatment temperatures, resulting carbon fibers have a higher modulus due to the formation of more graphitic crystallinity [Edie, D., Dunham, M (1989); Edie, D. D., Diefendorf, R. J. (1993), Liu, C. (2010)].

1.4 Carbon Fiber Microstructure

As stated above, mesophase pitch fiber microstructure development occurs in spinning during extrusion, when large planar aromatic molecules align with the direction of the flow. The resulting structure at capillary cross section greatly depends on process conditions and spinneret geometry. Various microstructures (Figure 1.8) and cross section geometries (Figure 1.9 and 1.10) have been formed in mesophase pitch based carbon fibers, due to spin filter pack induced deformation above the spinneret. Orientational discontinuities or defects, also defined as “disinclinations”, dissipate before mesophase pitch enters the spinneret if there is sufficient distance between filter pack and spinneret or if the melt temperature is high enough. At a lower temperature with minimal flow deformation, the radial microstructure is typically formed (Figure 1.8a).

Disinclinations disappearing from high spinning temperatures induce the formation of an onion skinned cross-sectional microstructure (Figure 1.8b). Lower spinning temperatures can also cause some of the filter mesh geometry to be retained in the pitch fiber, producing a more random cross sectional microstructure (Figure 1.8c) [Diefendorf, R.J. (2000)].

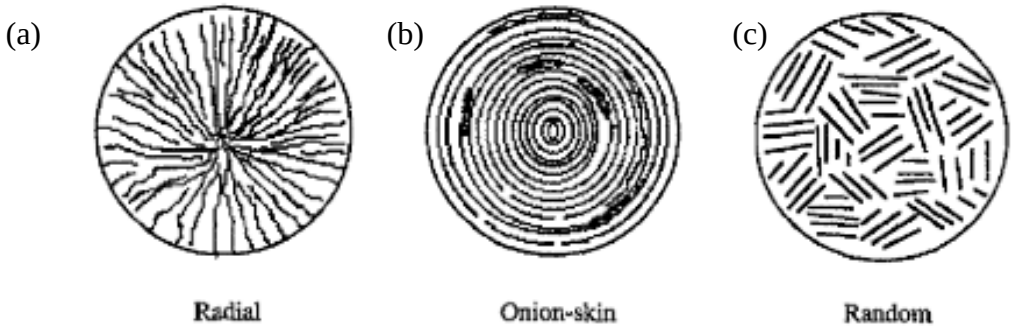

Figure 1.10: Mesophase pitch based carbon fiber microstructures

The shape of the spinneret capillaries directly determines the fiber cross sectional geometry. Commercially, circular fibers are the most frequently produced. However, circular fibers with radial texture have shown cracking and splitting during intense heat treatments, due to geometric constraints tampering shrinkage. This led to the development of spinning noncircular ribbon fibers (Figure 1.11), which enabled shrinkage and dissipating stress concentration. Lower electrical resistivity has also been observed in ribbon shaped fibers, compared to circular ones, due to their linear textures [Edie et al. (1993)]. The molecular orientation of as-spun ribbon fibers is more parallel to the fiber axis, compared to conventional round fibers, in addition to graphitizing more easily, which led to lower carbonization temperatures and costs [Gallego, N., Edie, D.D. (1999)]. However, due to small asymmetry of cross section of such trilobal and ribbon

fibers, they tend to twist along their length. This twist results in fiber breakage when such fibers are taken up on high speed during fiber spinning. Therefore, such noncircular shapes have not been commercialized.

Figure 1.11: Ribbon shaped fiber SEM showing transverse texture [Edie et al. 1993] and capillary cross section on spinneret

1.5 Finite Element Based Flow Modeling

Finite element analysis (FEA) has been utilized in polymer flow modeling to examine various flow geometries during processing. It was first implemented for die swell of Newtonian flows with creeping jets, assuming incompressibility and negligible surface tension constraints. FEA obtained jet expansion showed strong agreement with experimental results [Nickell, R. E.; Tanner, R. I., and Caswell, B., 1974]. FEA capabilities have been extended to generalized and non-Newtonian fluids, through slit and circular die swell flows [Chang, P.W.; Patten, T.W. ; Finlayson, B.A., 1979].

FEA simulations graduated to using multimodal constitutive equations to model viscoelastic flow and extrudate swell. Mu et al. [2011] investigated the flow of low-density-polyethylene (LDPE) through a hollow profile extrusion die, based on multi-mode Phan-Thien and Tanner (mPTT) constitutive model. Extrudate distortion was observed along the flow channel due to the polymer melt's swell behavior. Contour plots showed more abrupt shifts in velocity profiles at die structure transitions. In the 'parallel zone', where the die cross sections remained unchanged, uniform flow distribution was observed. The die swell studies also compared modeling with the following constitutive models: PTT, Giesekus, and the finite extensible nonlinear elastic dumbbell with a Peterlin closure approximation (FENE-P) model, through a circular die [Mu,Y. et al. 2013]. Swelling ratio predicted with FENE-P was smaller compared to PTT and Giesekus models. For all three models, the predicted swelling ratios approached each other at smaller volumetric flow rates.

Other rheological phenomena associated with polymers have also been investigated using FEA simulations. Stress relaxation behavior of polypropylene was compared between experimental and FEA studies, with the Computation Fluid Dynamics based software, ANSYS. Using the Generalized Maxwell Model for the material equation, little difference was revealed between the experimentally and numerically obtained transient stresses [Min,Yu et al. 2007]. Villacorta, Hulseman, and Ogale [2014] applied ANSYS for prediction of microtextured polypropylene (i-PP) film extrudate properties out of a rectangular-semicircular micro patterned die. The Polyflow module, tied in with Cross and Giesekus models, were used for pressure drop and extrudate shape

and die swell predictions. The isothermal, three parameter Cross model yielded accurate pressure drop predictions, but significantly deviated from the experimentally determined extrudate dimensions. Whereas, the Giesekus model's pressure drop predictions overshot the experimental results by almost two fold, but accurately predicted extrudate dimensions, within a 15 % error. This is attributed to the Giesekus model considering viscoelastic effects.

Jeon and Cox [2008] modeled multifilament melt spinning of PET, accounting for fiber viscoelasticity and crystallinity, as well as the air-quenching environment. Validation of the modelling results with industry measurements showed ~ a 10% difference in air temperature on the downwind side of the fibers. High fiber draw down speeds showed a noticeable crystallization. The study extended to isotactic PP, in addition to PET, under various process conditions [Jeon, Y.P. and Cox, C. 2009]. Higher mass flow rates resulted in lower PET fiber velocity, higher temperature, and a larger radius. Comparison between draw down and air quenching speeds for PP showed more discernible differences in fiber properties throughout the bundle at lower viscosities.

Microstructure resulting from mesophase pitch flow through round capillaries was predicted using ANSYS Polyflow, which utilizes FEA for calculation of velocity, stress, and pressure during extrusion [Fleurot, Edie 1998]. Upper convective Maxwell (UCM) was chosen as the rheological model since it successfully explained carbonaceous deformation, considers viscoelastic behavior, and has only two adjustable parameters. Optical micrographs of capillary cross sections showed similarities with the modeling predictions. However, the micrograph measurements indicated a smaller structure size

compared to what the model predicted. Good agreement was observed between the modeling and qualitative experimental observations of the converging entrance regions in the capillaries.

FEA based studies of polymer processing have focused on computing rheological properties of polymers using fluid models with a wide range of complexity. In varying the complexity of the fluid, the geometry constructed for the extruders have mostly taken on a simple configuration of a capillary or a counterbore followed by a capillary. Systematic studies have not been reported on fluid behavior in a spinning set up with the presence of a filter before the spinneret, nor examined the impact of capillary placement. Thus, a step in moving forward to improve the properties of carbon fibers will be understanding flow patterns before and through the spinneret during extrusion.

1.6 Objectives

The overall goal of this study was to examine flow patterns through complex die geometries, using FEA-based simulations. To keep simulations tractable, the viscosity models were kept limited to Generalized Newtonian Fluids (GNF). The specific objectives were:

(i) To use FEA based modeling to examine flow under high shear conditions through a barrel, counterbore, and single capillary used in batch melt spinning;

(ii) To examine the impact of a filter before the spinneret on flow pattern; and

(iii) To model flow through multiple capillary spinnerets in novelty dies for batch melt spinning;

Chapter 2 describes the framework of modeling flow through various spinnerets. Computational fluid dynamics simulations were carried out using the Polyflow module of the FEA based software ANSYS. Inputs consist of a CAD construction of the spinneret, followed by setting up the mesh for the FEA calculations and the material and flow parameters. The methodology was followed up by validation of the ANSYS modeling protocol with previously published work. Finally, Chapter 3 examines simulation results of flow through complex melt-spinning die geometries. It consists of results of the simulation of extrusion through a single capillary spinneret, as well as one with the addition of a filter, and finally a counterbore off-center with respect to multiple capillaries.

CHAPTER 2
MODELING FRAMEWORK

This chapter focuses on modeling methodology. First, the fundamental flow equations are discussed. Material properties and boundary conditions are examined, followed by geometry and mesh.

2.1 Governing Equations

With the assumptions of steady state, incompressible, and axisymmetric flow, the continuity and motion equations adhere to the following forms, with $\boldsymbol{v}$ as the velocity vector. (respectively equation 2-1 and 2-2) [Bird, R.B.; Stewart,W.E.; Lightfoot, E.N 2007].

$$\nabla \cdot \boldsymbol{v} = 0 \qquad 2\text{-}1$$

$$\rho(\boldsymbol{v} \cdot \nabla \boldsymbol{v}) = -\nabla p + \eta \nabla^2 \boldsymbol{v} \qquad 2\text{-}2$$

Since flow was assumed parallel to the walls, only one-dimensional flow was examined. Additionally, the isothermal assumption was in place, since extrusion of mesophase pitch does not start until the barrel housing to spinneret set up has been heated long enough to reach thermal equilibrium.

The constitutive equations adopted in this study were used for validation purposes, as well as the basis for modeling flow behavior in spinning conditions. Generalized Newtonian Fluids (GNF) were used for validation, starting with, Newtonian fluids:

$$\tau = \eta \dot{\gamma} \qquad 2\text{-}3$$

$\dot{\gamma}$ is the shear rate, representing the symmetric part of the velocity gradient and η represents constant viscosity. The rate of shearing is given in terms of velocity,

applicable to capillary flow, as follows:

$$\dot{\gamma} = -\frac{dv_z}{dr} \qquad \dot{\gamma} = -\frac{dv_z}{dy} \tag{2-4}$$

For model validation simulations, Ostwald's Power Law was also considered (equation 2-5).

$$\eta = \eta_0 \dot{\gamma}^{n-1} \tag{2-5}$$

The power law consistency coefficient is denoted by η_0, while n stands for the power law index ranging from 0 to 1. Non-Newtonian behavior is more pronounced with the power law index showing a greater departure from 1.

2.2 ANSYS 17.0 Flow Modeling

The modeling process consists of creating a geometry, mesh, and setting up material and boundary conditions before running the simulation. The CAD based ANSYS Design Modeler, was used to create geometries representative of the media fluids travel through. Appropriate meshes were customized for each geometry to set up the nodes where the software would run calculations. Subsequently, the meshed geometry was exported to the Polyflow module, to set material and boundary conditions to be factored into the calculations.

Meshing Method: Sizing Methods and Parameters

Meshing was also carried out on ANSYS Design Modeler. For the rheometer and single capillary spinneret assemblies, global sizing was used to control the growth and distribution of the mesh, which ensured similar mesh size throughout the geometry. The resulting mesh, using these settings, consisted of various mixtures of tetrahedral and hexahedral elements. The final mesh sizing was selected based on how close to zero the

resulting capillary centerline shear rate was, as well as the computational threshold.

The off-center counterbore-multi-capillary dies generated more mesh elements in the capillaries, due to the presence of multiple capillaries and more sudden contractions compared to single capillary geometries. To keep the number of elements manageable (with the available computational space), meshes were selectively sized for parts of these geometries, with finer meshes allocated to the capillaries.

Material & Boundary Conditions

In melt spinning extrusion, mesophase pitch does not show die swell or significant variation in viscosity, as a function of shear rate. Thus, its fluid behavior can be simplified to Newtonian. For all geometries, a unit viscosity (1 Pa. s) was used as the fluid model. The boundary conditions designated to all geometries were inlet flow rate, no slip for walls, planes of symmetry and outlet forces.

The *inlet fluid volumetric flow rate*, Q, through geometry entrance was given. The value of Q for the whole single capillary spinneret geometry was 1 cc/min, while flow rate through the multiple capillary spinneret was 1.7 cc/min. The flow rates assigned for each geometry fall within the range of stable spinning observed in AR-HP mesophase pitch. With a given value of Q, the circular capillary shear rate was calculated with equation 2-6.

$$\dot{\gamma} = \frac{4Q}{\pi r^3} \qquad 2\text{-}6$$

The average axial velocity through the circular capillary, barrel, or counterbore is the ratio of the volumetric flow rate to cross sectional area. The maximum velocity,

occurring at the centerline, is twice the average (equation 2-7) [Bird, R.B.; Stewart,W.E.; Lightfoot, E.N 2007].:

$$\frac{1}{2}v_{z,max} = v_{z,avg} = \frac{Q}{\pi r^2} \qquad 2\text{-}7$$

Q denotes volumetric flow rate, γ stands for shear rate, and r represents radius of the cross section of interest. The inflow calculation mode chosen in Polyflow reports a fully developed velocity profile.

No-slip conditions were imposed on the barrel and die walls, where the velocity is zero. *Planes of symmetry* are assigned to the planes slicing the geometry into even sectors. This boundary condition specifies zero normal velocity and zero surface force.

To achieve numerical convergence, an *outlet* condition had to be implemented, since pressure is assumed to drop to zero at the exit of the capillary. On Polyflow, this was accounted for by imposing normal and tangential forces equal to zero. This condition is typically used along the outlet of the extrudate. However, in this case it is given at the capillary outlet since examination of the extrudate is outside the interest of this study (Figure 2.1).

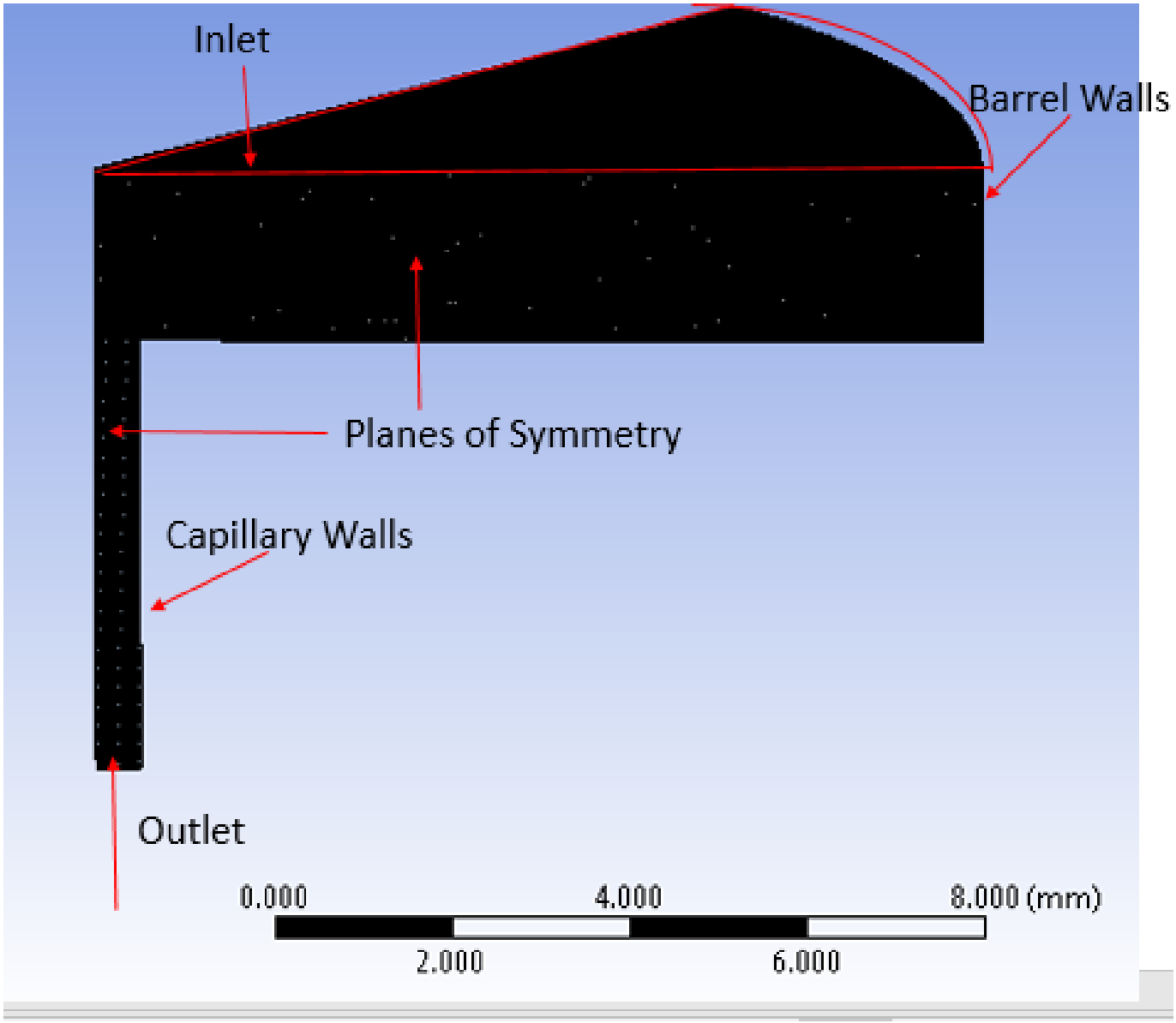

Figure 2.1: Locations for boundary conditions on sudden contraction geometry

2.3 Modeling Framework for Each Geometry

High Shear Rheology: ACER Capillary Rheometer

Most reported mesophase pitch high shear rheology data have been obtained from capillary rheometer experiments. To validate the general flow modelling protocol used in this study, the geometry and flow conditions from Kundu, Ogale [2006] ACER high shear rheology experiments were modeled and compared to the experimental results. The capillary rheometer consists of two domains: barrel followed by a single capillary, with dimensions from the experimental set up. The modeled barrel dimensions are a diameter of 20 mm and length of 2 mm, between the barrel and capillary entrances. The diameter of the capillary is 1 mm, with lengths: 5 and 30 mm modeled (Figure 2.2). To reduce computational memory usage and time , the length of the barrel was shortened, and split into one-eighths.

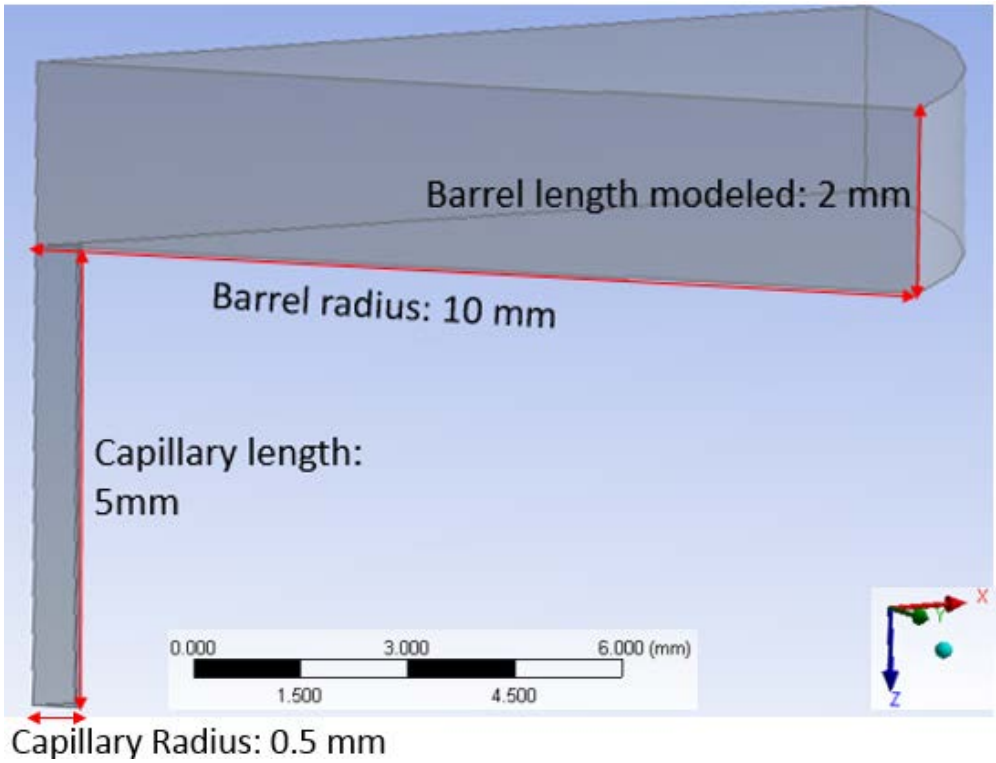

Figure 2.2: Sudden contraction barrel to capillary (L/D=10)

The mesh sizing was determined through trial and error, by inputting the element size. The generated mesh shows the number of elements produced. After running the meshed geometry through the Polyflow solver, the centerline to wall shear rate ratio was used to assess the model's accuracy (Table 2.1). The shear rate at the centerline in laminar pipe flow is zero, given that the gradient distance is measured at from the center to the walls. Thus, the accuracy was judged by how closely the center to wall shear ratio approached zero. The ANSYS provided coarse default mesh only generated about 4.5 thousand elements, resulting in a center to wall shear rate ratio of 38%. Thus, increasing the number of elements was crucial in enhancing accuracy. The barrel length was changed from 3 to 2 mm in order to increase the number of elements and reduce the

computational time. The element face length was minimized to 0.035 mm, producing over 2 million elements, significantly reducing the center to wall shear ratio to ~7%. It should be noted that after reducing barrel length, from 3 to 2 mm, the simulation ran with more elements in less time.

Table 2.1: Determination of Barrel and Element Size for Sudden Contraction Geometry

Barrel Length (mm)	Element Size (mm)	Number of Elements	Center Shear Rate (1/s)	Wall Shear Rate (1/s)	**Center/Wall Shear Rate (%)**	**Running Time (min)**
3	0.730	4,472	61	162	38	2.72
3	0.056	847,495	11.8	162	7.3	26
3	0.04	1,927,972	8.3	163	5.1	139
2	0.035	2,031,658	7.1	163	4.3	129
2	0.03	2,994,564	_____	_____	_____	Failed to run

For model validation, viscosity models used were based on data from capillary rheology studies conducted by Kundu and Ogale [2006] (Figure 2.3):

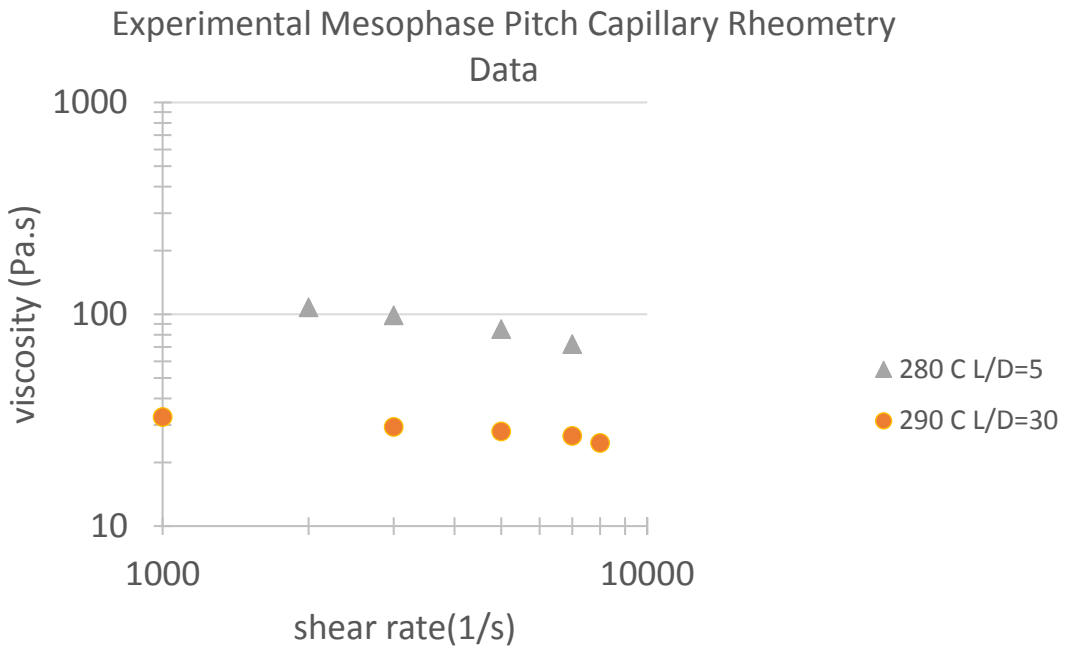

Figure 2.3: Mesophase pitch rheology experimental results used for the ANSYS model validation simulations [Kundu, S.; Ogale, A.A 2006]

The values of n ranged between 0.7 to 0.9, indicating weak shear thinning, and thus not far from a Newtonian response (Table 2.2). Thus, comparisons at each flow rate were run between experimental data, ANSYS Power Law, and ANSYS Newtonian models. Power law parameters were obtained through a curve fitting experimental data, while the Newtonian viscosity calculated from the average of the viscosities at a given temperature and capillary L/D. (Table 2.3):

Table 2.2: Newtonian Viscosities and Power Law Parameters for Each Die and Temperature

Temperature (°C), L/D	η_0	Power Law Parameter, n	Newtonian viscosity, η (Pa.s)
280 °C, L/D =5	1206	0.69	91
290 °C, L/D =30	76	0.88	28

Table 2.3: Inlet flow and Shear Rates used for Prior High Shear Mesophase Pitch Rheology Data [Kundu, S.; Ogale, A.A 2006]

Temperature (°C), L/D	Shear Rate (1/s)	Flow Rate through 1/8th of a Barrel (m^3/s)
290 °C, L/D=30	1000	$1.23x10^{-8}$
280 °C, L/D=5	2000	$2.45x10^{-8}$
280 °C, L/D=5 290 °C, L/D=30	3000	$3.68x10^{-8}$
280 °C, L/D=5 290 °C, L/D=30	5000	$6.14x10^{-8}$
280 °C, L/D=5 290 °C, L/D=30	7000	$8.59x10^{-8}$
290 °C, L/D=30	8000	$9.82x10^{-8}$

For each data set, since the shear rate was already known, the flow rate was calculated using Equation 2-6. Also given were the viscosities, so pressure drop though the capillary (vice versa with ANSYS calculated pressure drop and viscosity) were calculated using Equation 2-3 and 2-8.

$$\tau_w = \frac{\Delta P R_c}{2L_c} \qquad 2\text{-}8$$

For other geometries, pressure drops were analytically verified using Hagen Poiseulle (equation 2-9):

$$\Delta P = \frac{8\mu L Q}{\pi R^4} \qquad 2\text{-}9$$

Single Capillary Fiber Extrusion Geometry

In melt spinning, the geometry was divided into the following domains: barrel, counterbore, and capillary. The barrel dimensions consist of a diameter of 38 mm and a length of 2 mm, followed by the counterbore, serving as a transition for mesophase pitch flow between the barrel and capillary. The counterbore entrance diameter is 0.8 mm, and the length 1mm, in order to yield a frustum slant angle of about 60°, as specified for the dies custom made by machining services (Figure 2.4). This transition region leads to the capillary, where the diameter is 0.5 mm and the length extends to 5mm. The geometry was split into a one-eighth segment to reduce computational memory and time.

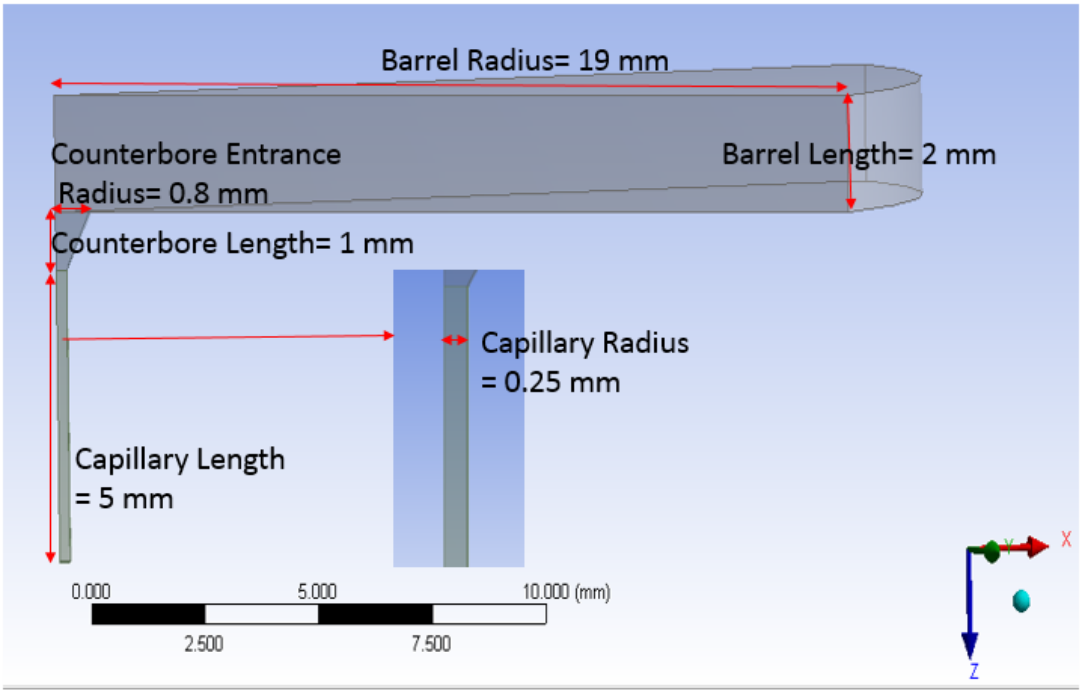

Figure 2.4: Geometry for barrel to capillary with transitory frustum counterbore region, modelling rudimentary die set up for batch unit fiber spinning

For investigation into the impact of barrel to counterbore contraction, simulations were run with various barrel diameters, with capillary diameter kept constant, at unit η=1Pa.s and fixed one-eighth geometry inlet $Q = 2.08 \times 10^{-9}$ m^3/s.

The mesh sizing was carried out to maximize the number of elements that could complete the calculation on limited computational space. At barrel diameters 38 mm, the computational space reached its limit around 3.0 million elements and lowered almost 2 fold at a barrel diameter of 3 mm. Accuracy was assessed through the proximity of centerline shear rate to zero. Centerline shear rate significantly decreased after lowering barrel diameter from 38 mm. When L/D was lowered to 1, an increase was observed.

Running time was significantly reduced with smaller barrel diameters. The stark drop from capillary L/D=10 to 1 for the 1.6 mm diameter barrel resulted in over a twofold reduction in the number of elements generated, as well as running times. Overall, decreasing barrel diameter enhanced computational accuracy, as well as lowering running times (table 2.4).

Table 2.4: Mesh Assessment for Barrel Contraction Studies

Barrel Diameter (mm)	Capillary L/D	Element Size (mm)	Number of Elements	Wall Shear Rate (1/s)	Centerline Shear Rate (1/s)	Running time (min)
38	10	0.045	3,046,206	1301	105	238
3	10	0.0125	1,673,038	1344	32	182
1.6	10	0.0120	1,301,300	1333	36	138
1.6	1	0.0120	474,912	1333	55	103

Fiber Extrusion: Addition of Filter

In the batch melt spinning process, a filter is placed under the end of the barrel to remove solid impurities. A sintered metal filter is used instead of a mesh-type filter since they lead to a higher pressure drop due to reduced area through fine filter pores, whereas the latter leads to a small-added flow resistance. In this study, the fine porous area was simplified to a reduced overall area of melt flow. While modeling the filter as a contraction incorporates its porosity, it does not take into account overall permeability, which depends on pore geometry and arrangement. The barrel diameter is 1.6 mm, with a length of 2 mm (Figure 2.5) before reaching the filter. The filter is represented by concentric circles, with an outer diameter of 1.6 mm, an inner diameter of 0.8 mm, and

0.1 mm thickness. The inner diameter represents the effective flow area through the filter (Figure 2.6). The geometry was split into a one-eighth segment to reduce computational memory and time.

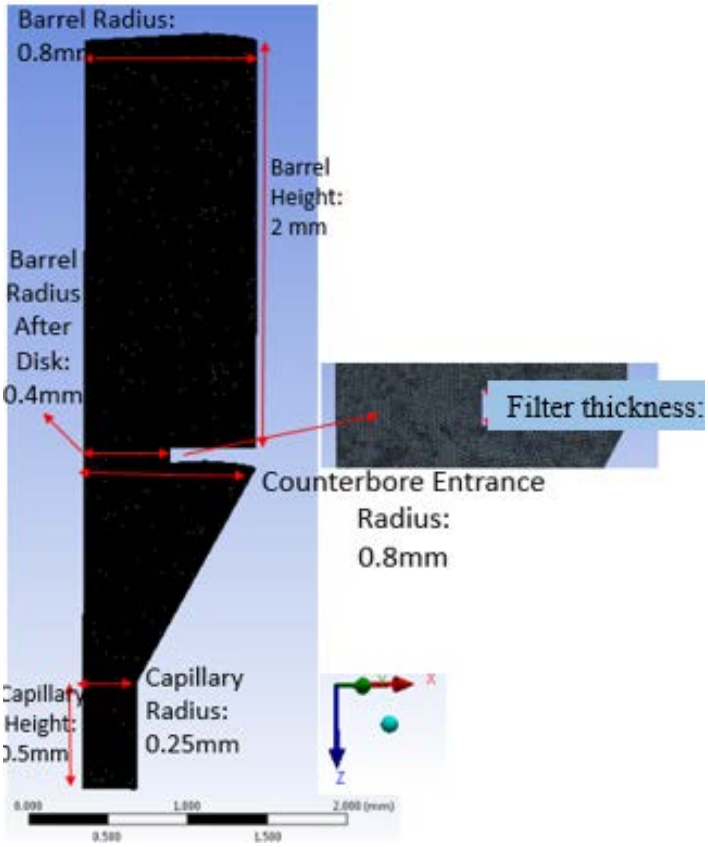

Figure 2.5: Batch melt spinning die with filter adding an extra contraction before counterbore

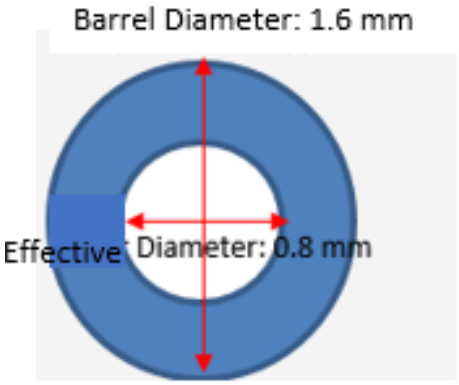

Figure 2.6: Cross section of contraction caused by filter in barrel

To examine how significantly the filter affects flow through the barrel, comparisons were conducted between the single capillary spinneret and its counterpart including the filter, at various L/D's. For both geometries, fluid was modeled with unit viscosity (1 Pa.s) and Q= 2.08×10^{-9} m^3/s. Mesh sizes for both geometries was also determined through trial and error, where the input element size, started from lowest possible value and increased until the simulation was able to complete its calculations. With the filter, the element size reached its minimum at 0.0075 mm, and 0.0125 mm without the filter. The number of elements increased proportionally with capillary length (Figure 2.7). Thus, the running time also increased proportionally (Figure 2.8).

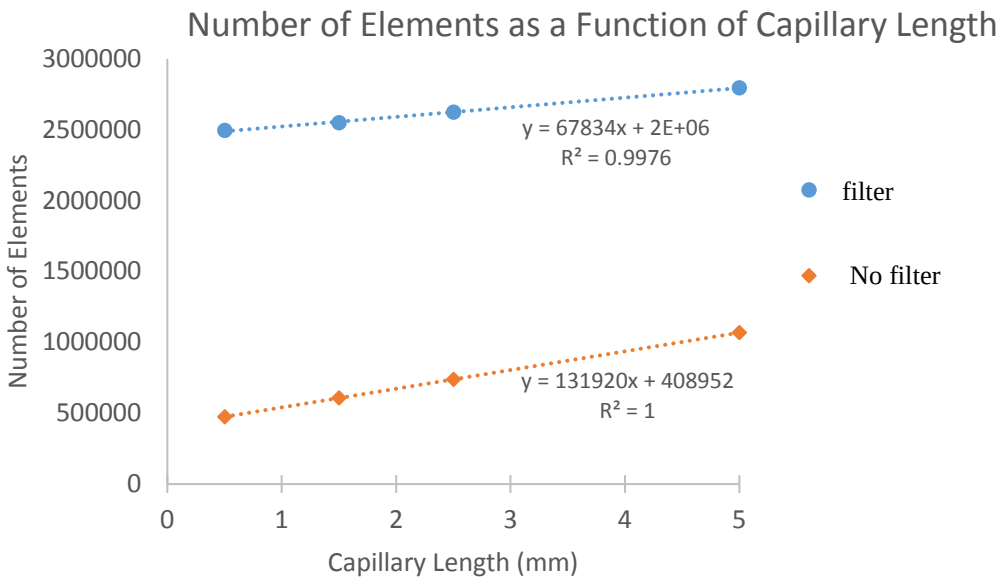

Figure 2.7: Linear progression of number of mesh elements vs. capillary length

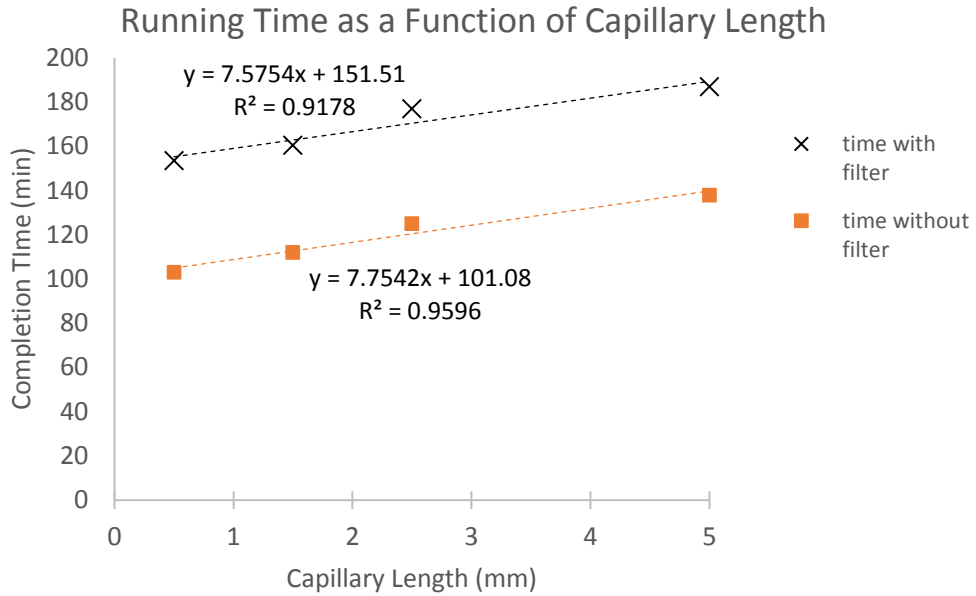

Figure 2.8: Linear progression of number of running times vs. capillary length

Model accuracy was verified by checking how close to zero centerline to wall shear rate ratios and capillary exit pressure converged to. Center to wall shear rate proportions showed a narrow range, of 2.5- ~4.0 %, at various L/Ds. From L/D of 1 to 3, a slight decline was observed (table 2.5). Overall, it showed a significant drop from the center to wall ratio of the barrel diameter at 38 mm (table 2.4). However, with 1.6 mm barrel diameter geometries, the negative exit pressure magnitude exceeded 1% of the entrance pressure . The exit to entrance pressure ratio (magnitude) declined through higher L/Ds (table 2.5). Thus, higher accuracy of the filter incorporated geometry and its counterpart is noted at longer capillary L/Ds.

Table 2.5: Mesh Accuracy Comparisons between Barrel-Counterbore-Capillary with and without Filter

Capillary L/D	Capillary Length, Z (mm)	Elements (with filter)	Center/ Wall Shear Rate (%) (with filter)	Exit/ Entrance Pressure (%) (with filter)	Elements (without filter)	Center/ Wall Shear Rate (%) (w/o filter)	Exit/ Entrance Pressure (%) (without filter)
1	0.5	2,495,818	4.1	-11	474,912	4.2	-17
3	1.5	2,548,297	3.1	-2.2	606,832	2.5	-5.1
5	2.5	2,623,194	3.1	-2.6	738,752	2.5	-3.6
10	5.0	2,796,348	3.1	-1.4	1,068,552	2.5	-1.4

Off-Center Counterbore-Capillaries

In high yield spinning processes, spinnerets with multiple capillaries are utilized, dividing the initial flow through the counterbore. The geometry consists of a 2mm long, 3mm diameter counterbore, leading to 12 uniform circular capillaries, with diameters of 0.15 mm, alternating in positional alignment, around the counterbore centerline. Capillaries at counterbore R_1 are equidistant to capillary located at R_2. To conserve computational space and time, one-sixth of the barrel, including one whole and two halves of a capillary, was modeled (Figures 2.9 and 2.10). A comparison of distances between capillaries was carried out by changing the position of the whole capillary, to investigate how misalignment influences flow patterns. The inter-capillary distance, denoted by X, ranges from 0.23 mm (where the R_2 capillary is collinear with R_1), to 0.79 mm.

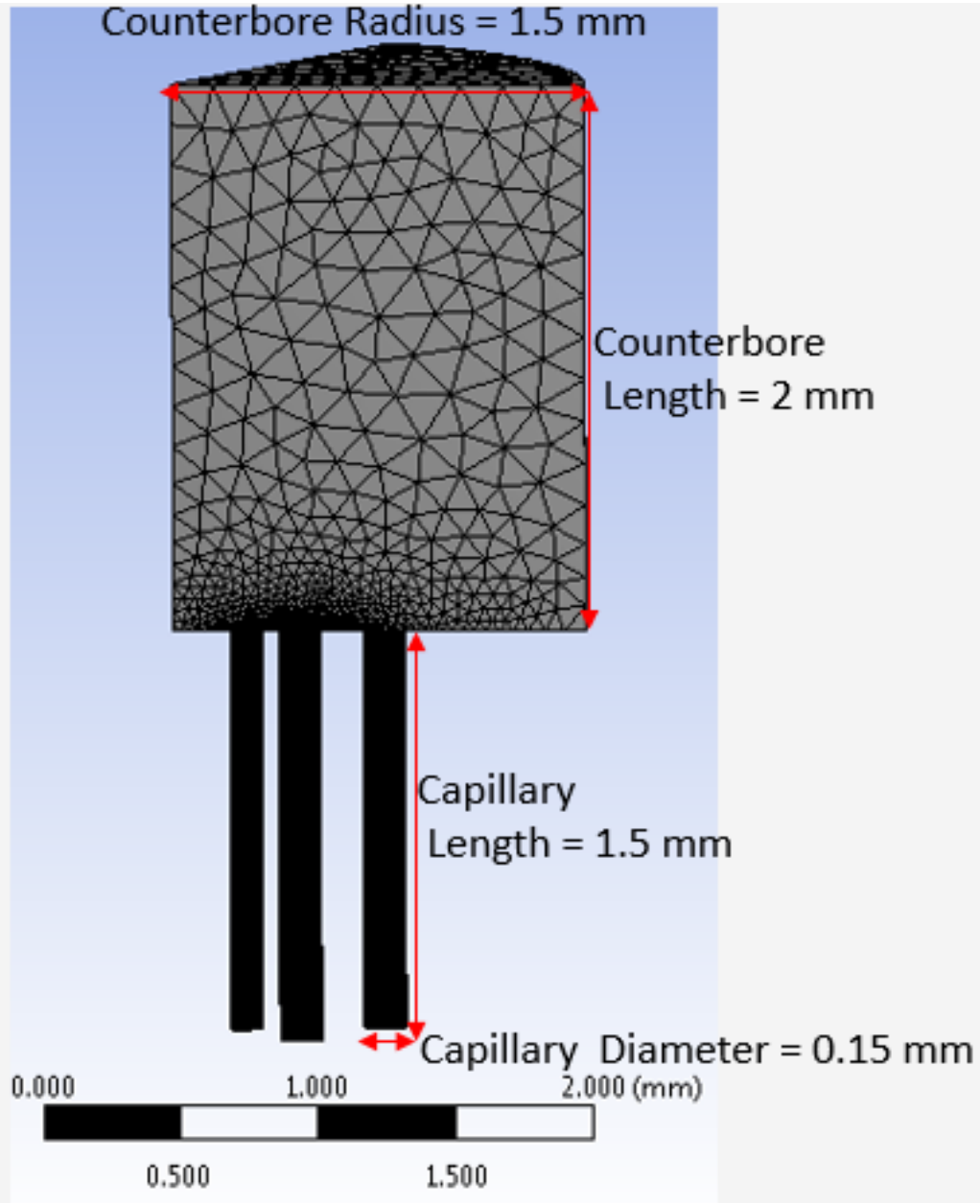

Figure 2.9: Geometry for 1/6th counterbore leading to two capillaries: two halves along the plane of symmetry and a whole

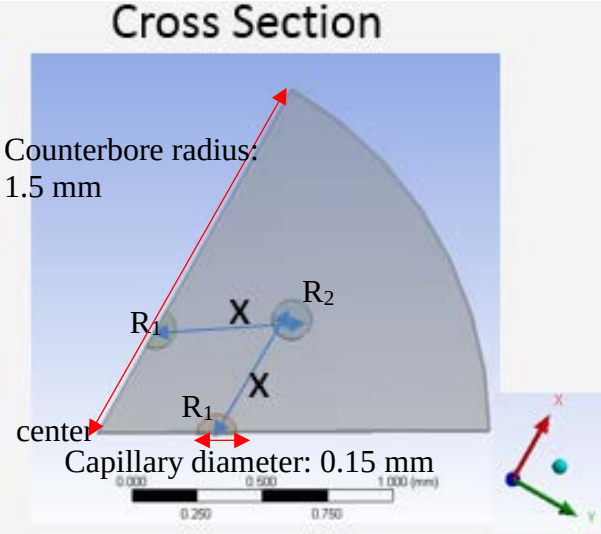

Figure 2.10: Twelve positionally alternating capillaries eccentrically placed on a counterbore, with 1/6th of the geometry modeled, at various inter-capillary distances of x. Pictured is the cross section of a die with x=0.521 mm

For this geometry, the meshing protocol included by selectively sizing capillaries. Finely meshing the capillaries yielded high accuracy and less running time. Using the 'sphere of influence' body sizing enabled allocating much smaller elements only around bodies the sphere encompasses (Figure 2.11). The mesh size assigned to the counterbore was 0.15 mm, while each of the mesh elements in the capillaries were individually sized at 0.0065mm, with a 0.76 mm radius sphere of influence. Since the sphere does not mold exclusively to the shape of capillary, some of it also touches a small portion of the counterbore surface area. This accounts for the gradual increase in the number of elements, with larger X, despite the same capillary and counterbore dimensions, (Figure 2.12).

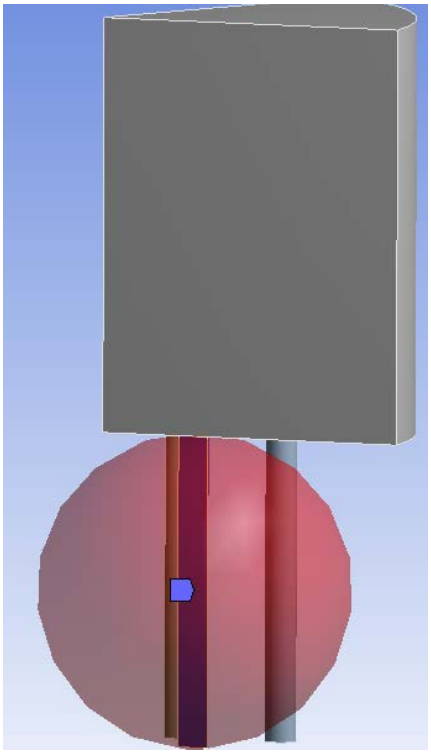

Figure 2.11: Sphere of influence surrounding one capillary as the only portion of the geometry volume to be finely meshed. Separate spheres of influence were implemented for each capillary

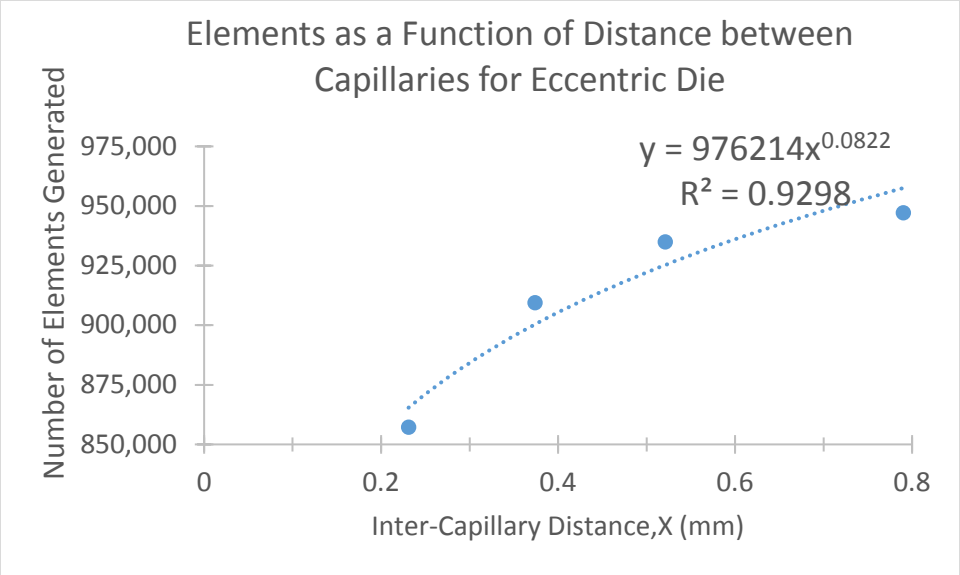

Figure 2.12: Number of mesh elements as a function of distance between capillaries for eccentric die counterbore-capillary geometry

The running time gradually increased as a function of X, as expected from the gradual increase in elements. The magnitude of the exit pressure remained at 1.3 %, through all capillary distances, at L/D= 10. Similar to the single capillary spinneret, the exit pressure magnitude increased to 11% L/D=1. Thus, the accuracy of the off-center spinneret model did not change as a function of capillary position (table 2.6).

Table 2.6: Mesh Assessment as a Function of Centerline Misalignment

Distance between capillaries at R_1 and R_2 (mm), **X**	Distance between Capillary and Counterbore Center (mm)	L/D	Number of elements	Exit/ Entrance Pressure (%)	Running time (min)
0.23	0.40	10	857,162	-1.3	32.9
0.37	0.69	10	909,364	-1.3	34.1
0.52	0.87	10	934,934	-1.3	36.0
0.79	1.16	10	947,212	-1.3	37.0

CHAPTER 3

RESULTS AND DISCUSSION

3.1: Experimental Data Validation with ANSYS Polyflow

To validate the flow modeling protocol on ANSYS, simulations were conducted based on the geometries, material, and flow conditions listed in Table 2.2 and Figures 2.7. The high shear rheology experiment results were used [Kundu and Ogale 2006] and ANSYS calculated data were checked against the experimental ones. The geometry consisted of a 20 mm diameter barrel, leading straight into a 1 mm diameter capillary, with the L/D= 5 and 30 for the three sets of data analyzed. Shear rates ranged from 1000- 10,000 1/s. Each simulation, at a given L/D and temperature, was conducted with both Newtonian and fitted Power Law viscosity models for comparison. For validation of ANSYS calculations, the experimental and modeling pressure drops were compared from experiments conducted with capillary L/D=5 at 280°C and L/D=30 at 290°C . Although viscosity-shear rate data were reported (Figure 2.7), these were in turn calculated from volumetric flow rates, Q and experimental pressure drops (equations 2-6 and 2-8).

Both experimental and ANSYS results show larger pressure drops with a longer capillary L/D, at a given shear rate. Capillary L/D=5 at 280°C showed a 9.4% difference between Power Law and experimentally obtained pressure drops, and a slightly larger difference of 14% between Newtonian and experimental results. At capillary L/D=30 at 290°C, Power Law and Newtonian models respectively showed 3.1 and 6.3% differences from experimental pressure drop (Figure 3.1). It should be recalled that the difference seen

even with a Newtonian fluid assumption (14%) is much smaller than the difference reported using a Giesekus model in prior literature studies [Villacorta and Ogale 2014].

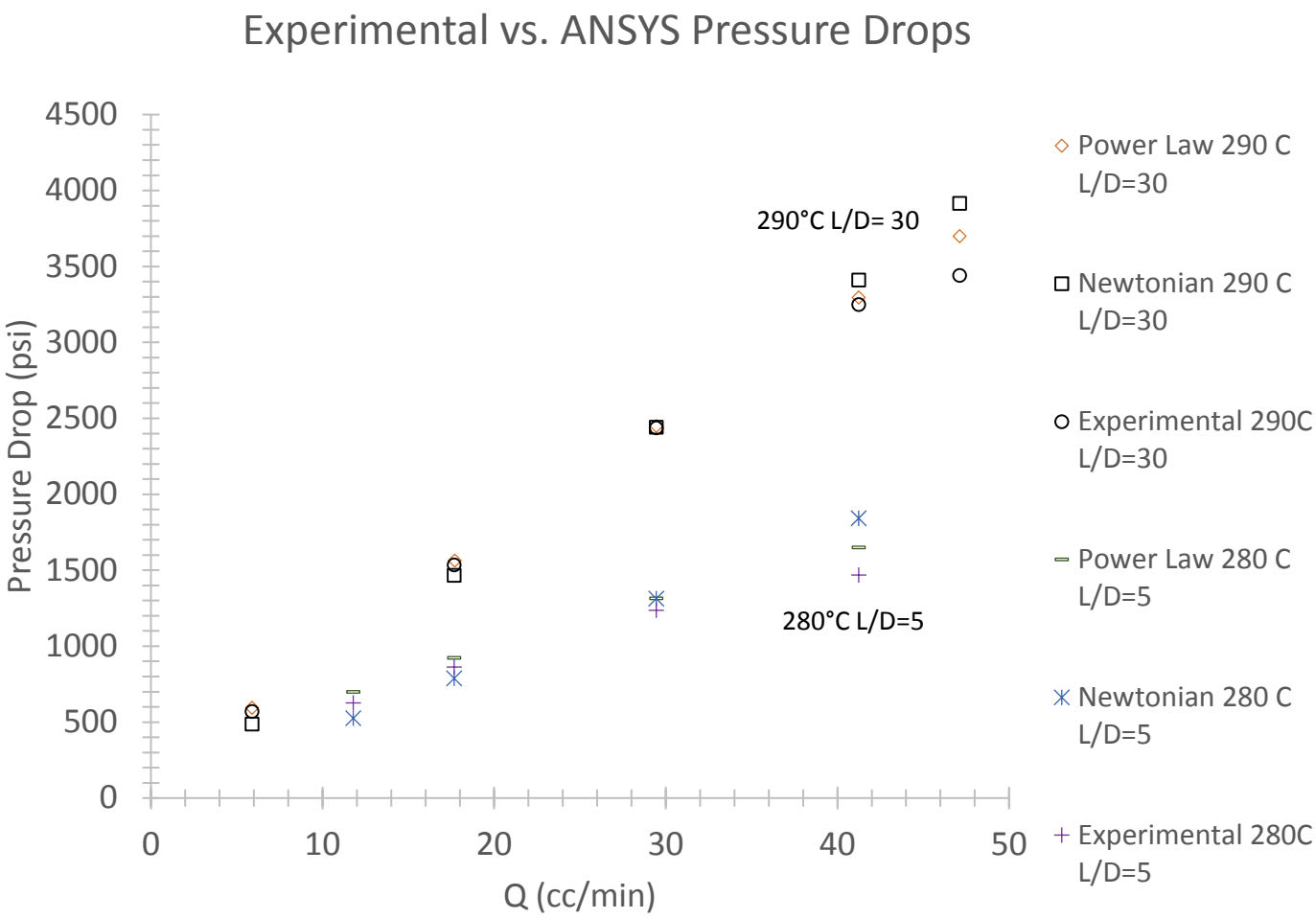

Figure 3.1: Experimental vs. ANSYS pressure drops from Kundu and Ogale [2006]

Thus, the low differences between experimental data and predicted pressure drops establish the accuracy of the current modelling approach. Further, in an effort to limit computational time, the simpler Newtonian model was used to investigate flow patterns in the complex multi-capillary spinnerets.

The rest of this chapter presents results obtained by conducting numerical simulations of various meshed geometries and ANSYS Polyflow. To assess the accuracy of the ANSYS results, the capillary shear rates, pressure drops, and velocities were compared to their analytically calculated counterparts. Simulation results were first obtained for a rudimentary spinneret model, as well as capillary L/D comparisons for the model including the addition of a simplified filter. An off-center counterbore to multi-capillary spinneret was also similarly analyzed. Comparisons for this complex geometry were conducted with various inter-capillary distances.

3.2: Single Capillary Fiber Spinneret Set Up

ANSYS calculations were first checked with shear rate profiles, as a function of radius across the capillary, for various barrel diameters. Barrel diameters ranged from 1.6 to 38 mm. Capillary diameter was fixed at 0.5 mm, with L/D at 10, and the fluid was assigned unit viscosity, $\eta = 1$ Pa.s. Due to axisymmetry, only one-eighth geometry was analyzed with a set flow rate Q of 2.08×10^{-9} m^3/s.

The analytically calculated wall shear rate (Equation 2-6) was 1358 1/s. A small deviation in wall shear rates was observed for all barrel diameters, ranging from 1301 to 1344 1/s, but no trend could be inferred. However, ANSYS calculations could not precisely predict a zero shear rate at the centerline. However, the centerline shear rate, at a fixed capillary L/D, approached closer to zero, with reduced barrel diameter (Table 3.1). This can be attributed to the contraction from barrel to counterbore becoming more gradual with smaller barrel diameters. The centerline shear rate for barrel diameter= 1.6 mm and L/D=1 increased back to 55 1/s. With a smaller L/D, flow through the capillary

does not recover from the contraction, as much as flow through longer capillaries (Table 3.1).

Table 3.1: Wall and Centerline Capillary Shear Rates at Fixed Capillary Diameter of 0.5 mm

Barrel Diameter (mm)	Capillary L/D	**Wall shear rate (1/s) d=0.25 mm**	**Center line Shear Rate (1/s)**
38	10	1301	105
3.0	10	1344	32
1.6	10	1333	34
1.6	1	1333	55

Figure 3.2 displays ANSYS predicted parabolic velocity profiles along the capillary radius. The parabolic profile is consistent throughout the capillary length, up until the exit, where the velocity vectors diverge (Figure 3.3). In the fully developed region of the capillary, analytically calculated centerline velocity was 170 mm/s (Equation 2-7), which compares well with predicted centerline velocities of 170-171 mm/s. Thus, a small difference (0.6-0.8%) was observed between ANSYS and analytically calculated centerline velocities. Based on the near overlap of the velocity profiles (Figure 3.3), it can be concluded that barrel diameter does not have a significant impact on the flow in the fully developed region.

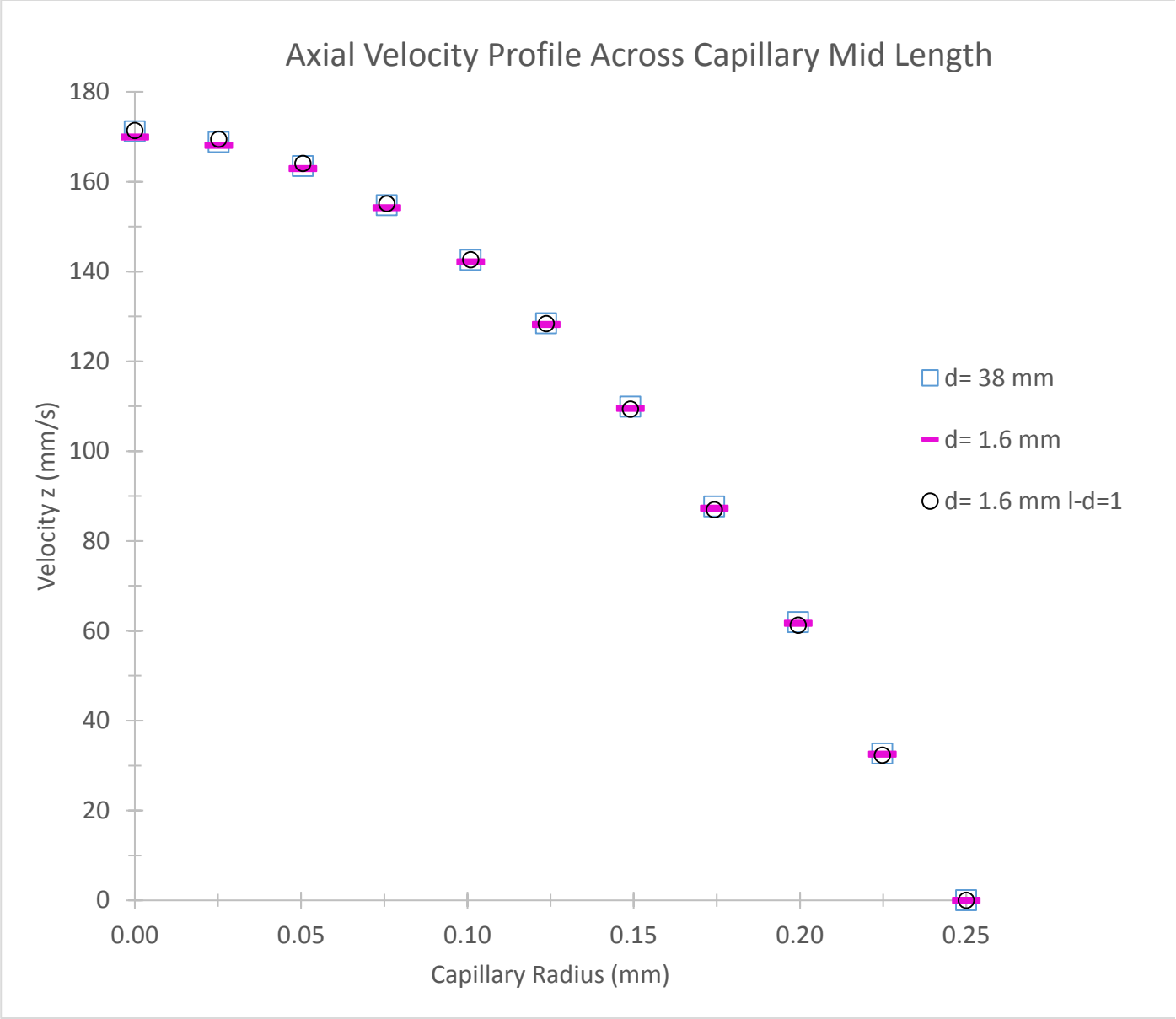

Figure 3.2: Axial velocity profiles across middle of capillary along radius at various barrel diameters, at l/d=10, except for barrel diameter= 1.6 mm at L/D=1

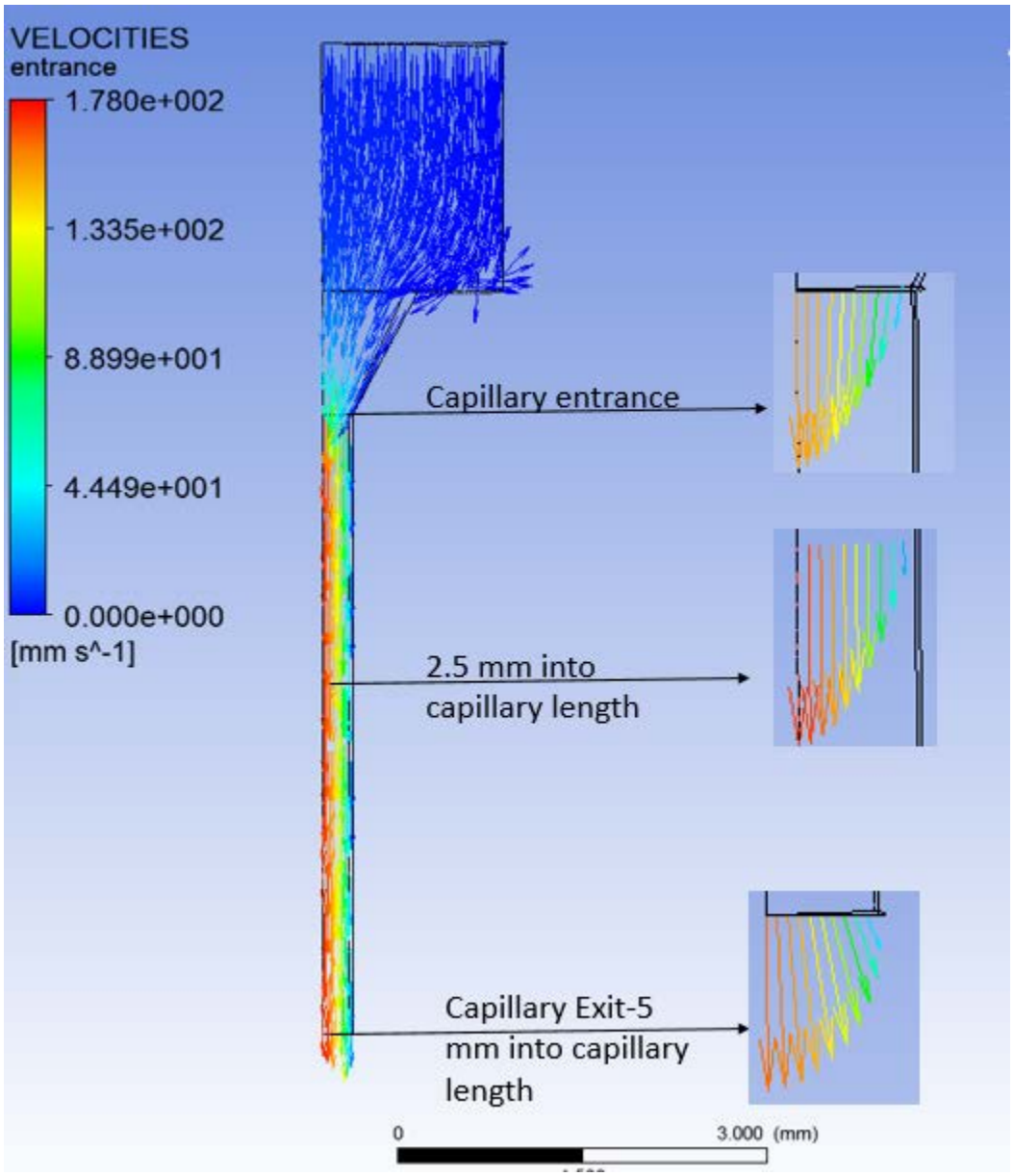

Figure 3.3: Velocity vector visual focused on capillary region

Pressure profiles were examined from the barrel entrance to capillary exit at the capillary centerline. The pressure drop was found to be negligible through the barrel. This is consistent with experimental evidence because the pressure drop scales inversely with capillary D^4 for a given volumetric flow rate (equation 2-9). The pressure drop showed a gradual decay through the counterbore, and then concluded with a linear drop to ambient pressure at exit (Figure 3.4). At L/D = 10, the pressure in the barrel ranged from 56.3 to 56.6 kPa, and pressure drop in the capillary ranged from 53.4 to 53.6 kPa, through all barrel sizes (Figure 3.16). Given this extremely low variation, the barrel size was not found to have any significant bearing on pressure drop. The difference between ANSYS and analytically calculated pressure drops through the capillary was ~4%. With the capillary L/D dropping from 10 to 1, barrel pressure dropped to 7.58 kPa, and pressure drop through the capillary decreased proportionally to 5.14 kPa.

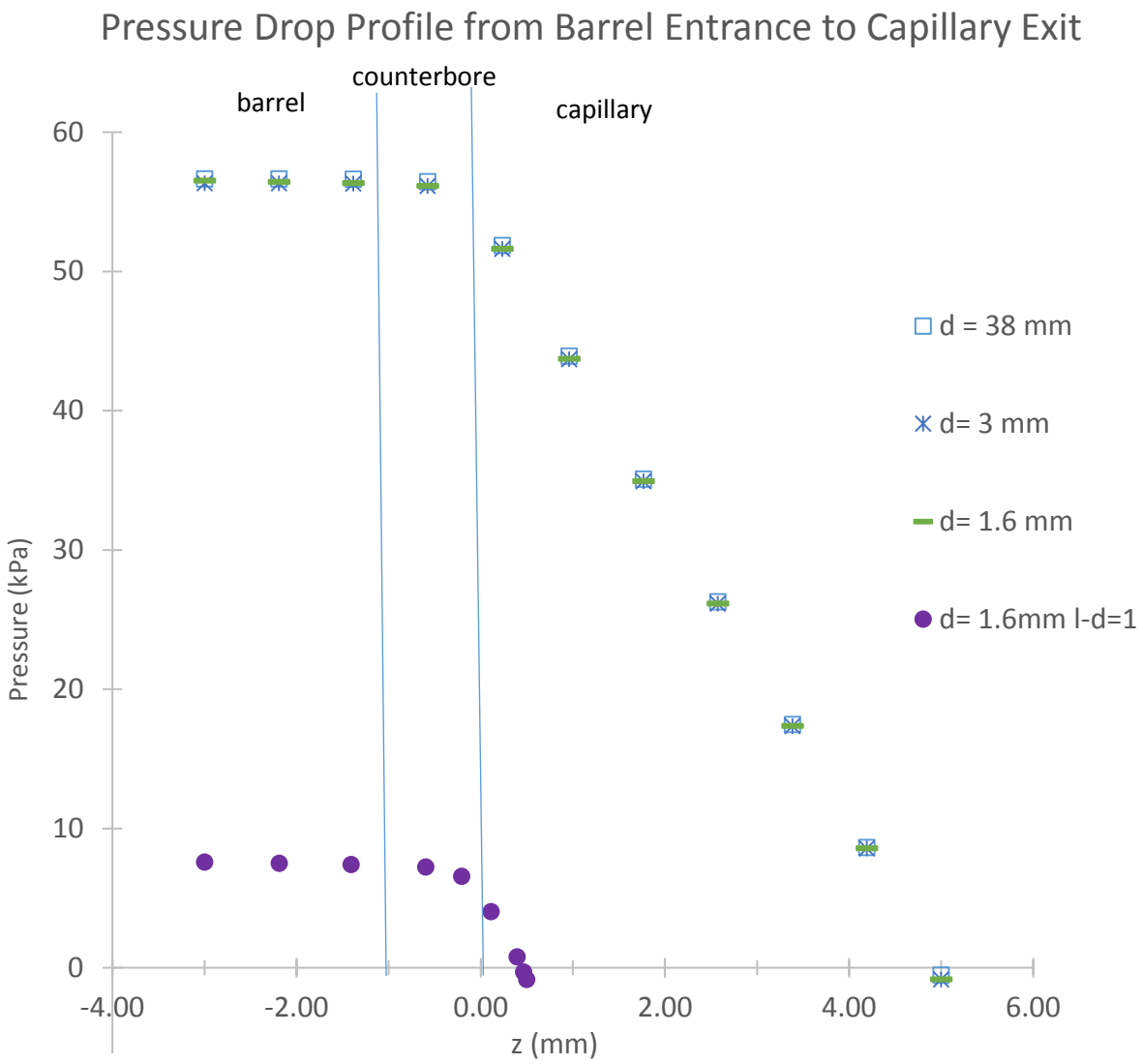

Figure 3.4: Pressure drop profiles along centerline, from barrel entrance to capillary exit, for various barrel diameters, at L/D=10, unless specified

Axial velocity profiles at capillary entrance region were of interest as another way of examining the effect of the degree of contraction from barrel to counterbore. Capillary entrance maximum velocity is notably smaller, at 155 mm/s, compared to mid-capillary velocity. This was expected because flow is not fully developed at this point, as seen by how the vectors still slightly merge toward the centerline, like the flow through the counterbore. Profiles were parabolic and almost completely overlapped, thus indicating no significant impact of barrel size on capillary entrance. The counterbore, as a transition region between the barrel and capillary, could have reduced the contraction effects to some extent, hence no clear manifestation of the effect of the barrel diameter on capillary entrance velocities could be seen.

Because there was no discernible effect of barrel size on capillary entrance, this examination was moved upstream to the counterbore. While entering the counterbore, the fluid adhered to its shape, where the vectors merged from the radius to the centerline (Figure 3.5). ANSYS predicted the centerline velocities from 20.3 to 22.1 mm/s, which were significantly smaller compared to capillary entrance center velocities around 150 mm/s. This shows how rapidly the flow accelerates through the counterbore contraction. No change in counterbore velocity profile was observed until barrel diameter was decreased to 1.6 mm, where the centerline velocity increased to 22.1 mm/s and velocities approaching the wall showed a faster rate of deceleration compared to those of other barrel sizes (Figure 3.6)

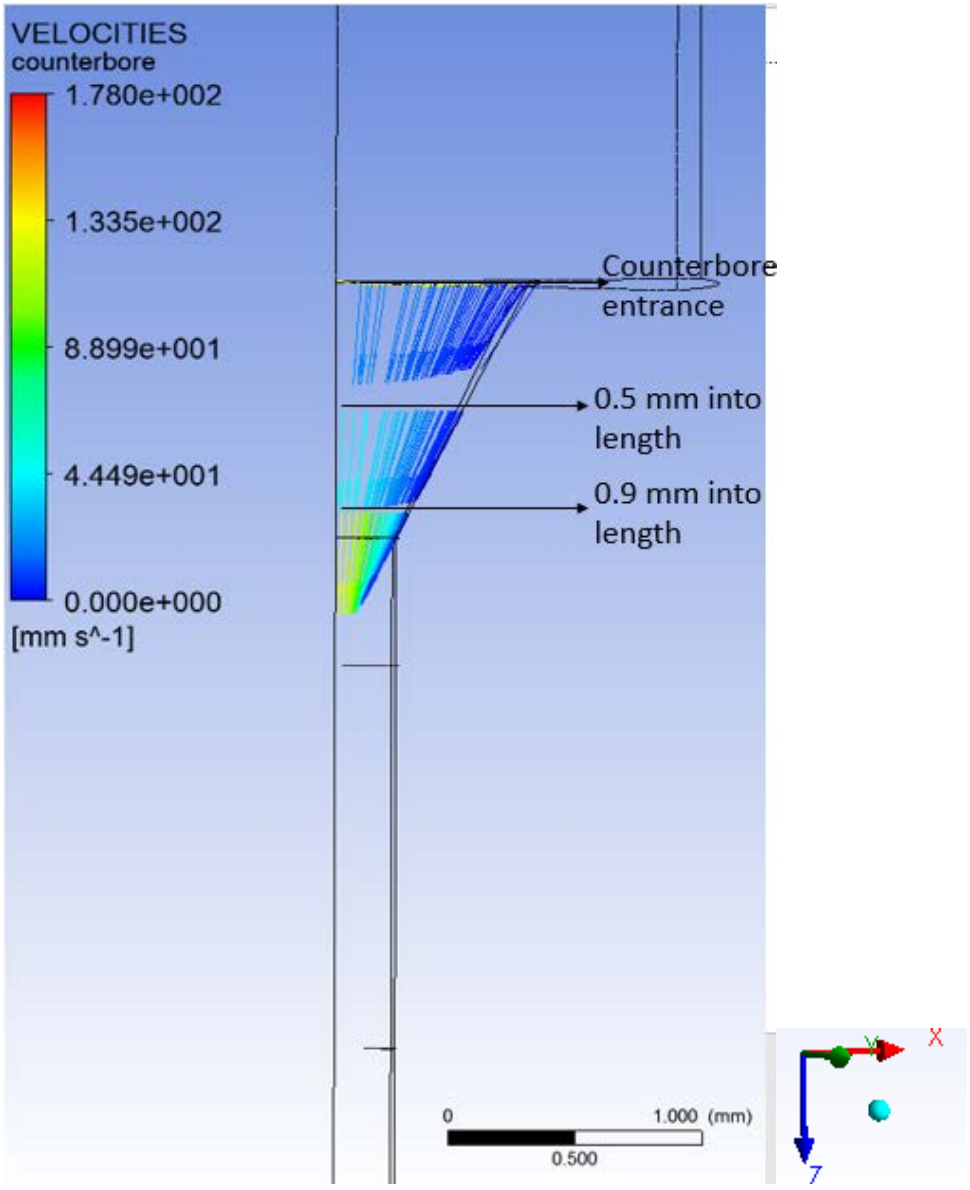

Figure 3.5: Velocity vectors through counterbore region at barrel diameter= 3 mm

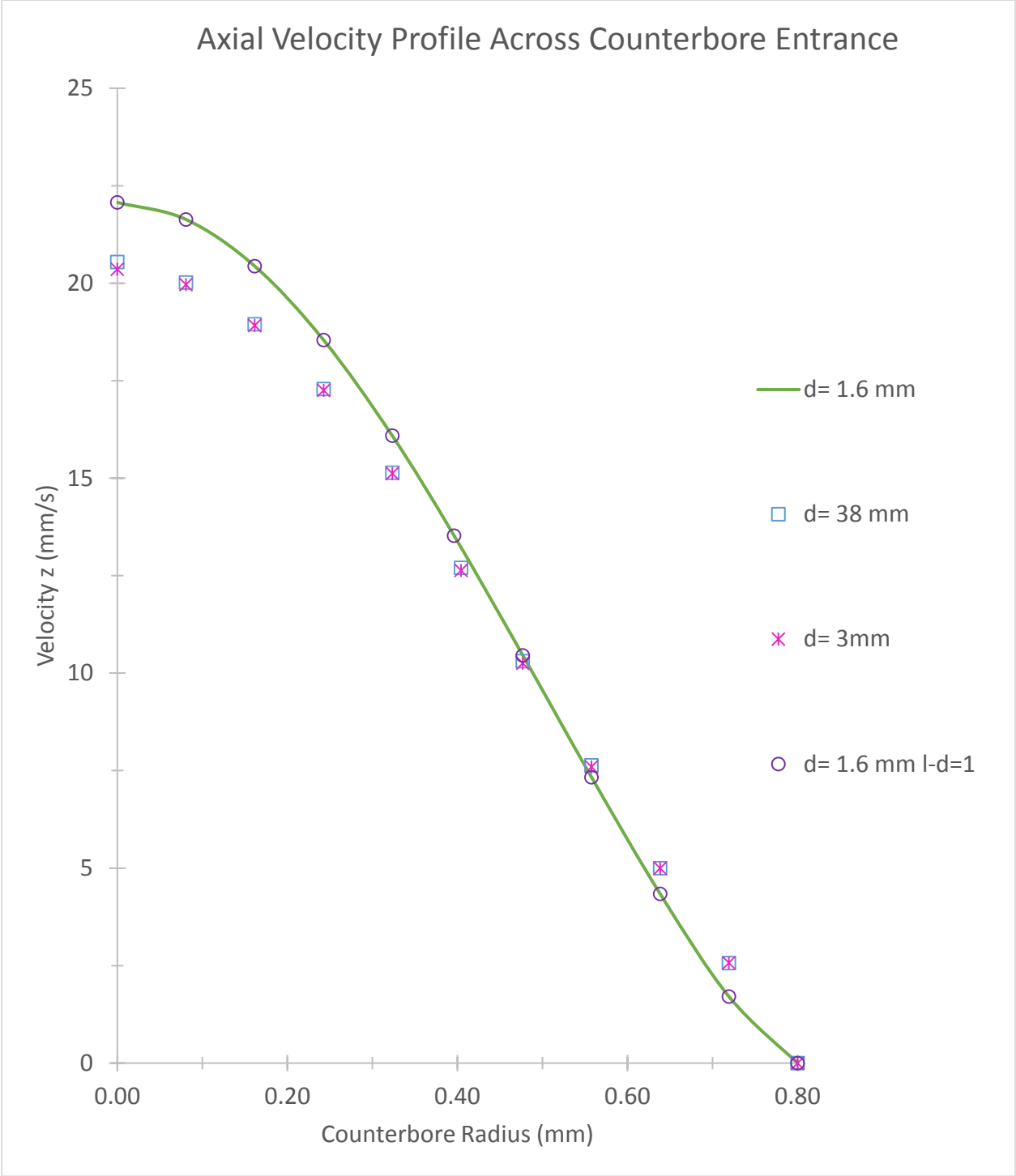

Figure 3.6: Axial velocity profiles across entrance of counterbore along radius for various barrel diameters. L/D=10, unless specified otherwise.

Flow fields through various barrel diameters are shown in Figures 3.7 and 3.8, at two different vector densities (for visual clarity). Visuals with fewer vectors give a clear indication of flow direction, while the one with higher vector density highlights vortices and flow divergences missed by the former. For all barrel sizes, flow was initially longitudinal, and then started merging towards the centerline where the counterbore and capillary are located. At the centerline, flow was oriented in the z-direction and continued as such through the capillary. Vortex formations were observed at the barrel corners. The width of the vortices decreases as the barrel diameter decreased with smaller barrel diameters. Respectively, the width of the vortices, at barrel diameters 38, 3, and 1.6 mm were 2.07, 0.99, and 0.27 mm. This is due to the extent of contraction from barrel to counterbore. For the smallest barrel diameter of 1.6 mm, the vortex was barely noticeable in the flow field visual, as expected (Figure 3.8). Although these are interesting flow patterns, vortices are not desired in actual fiber spinning runs because the melt that remains stuck in a vortex can thermally degrade due to extended residence time.

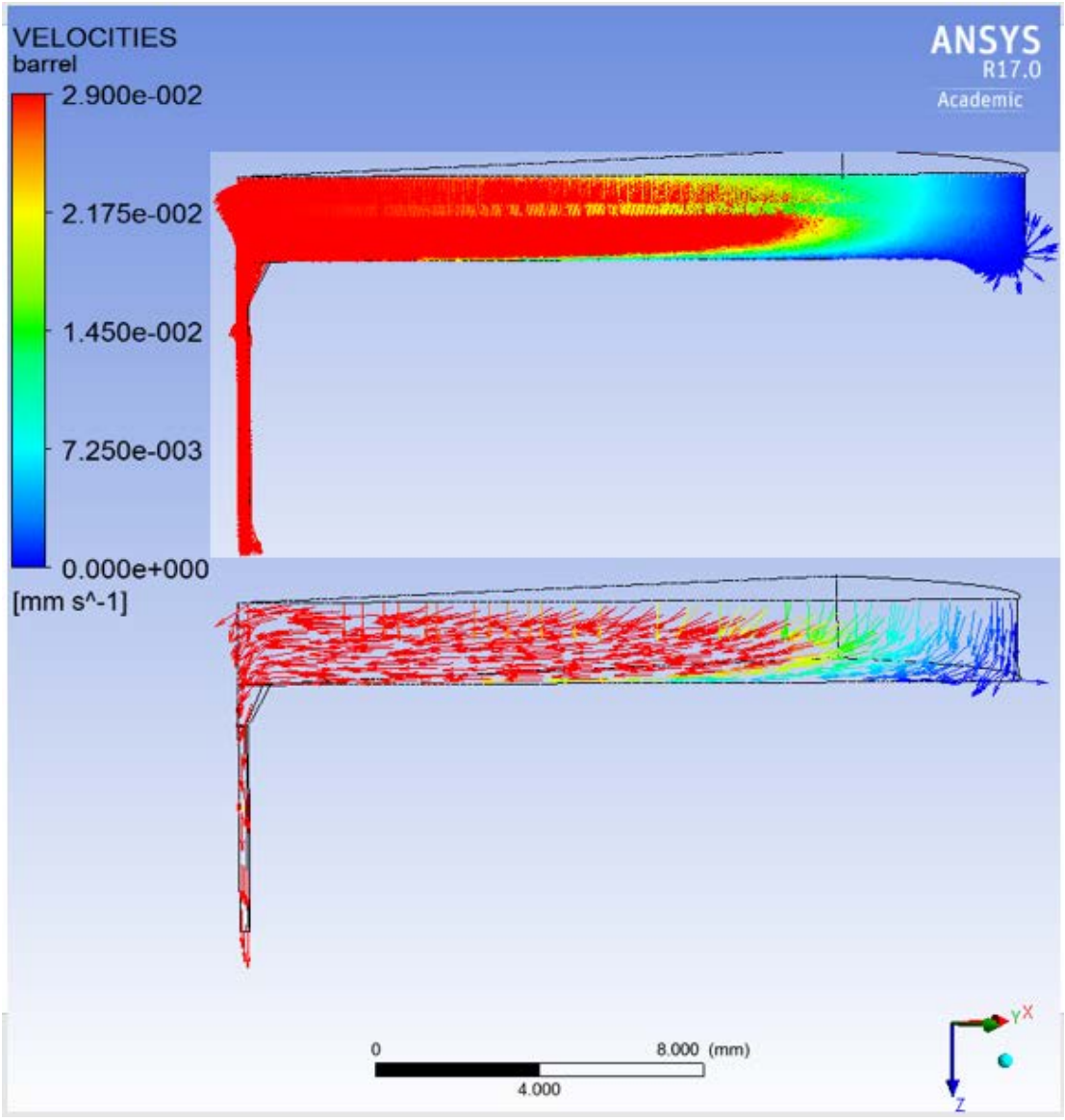

Figure 3.7: Velocity vectors from barrel to capillary at barrel diameter= 38 mm-top visual shows vectors hundred fold denser

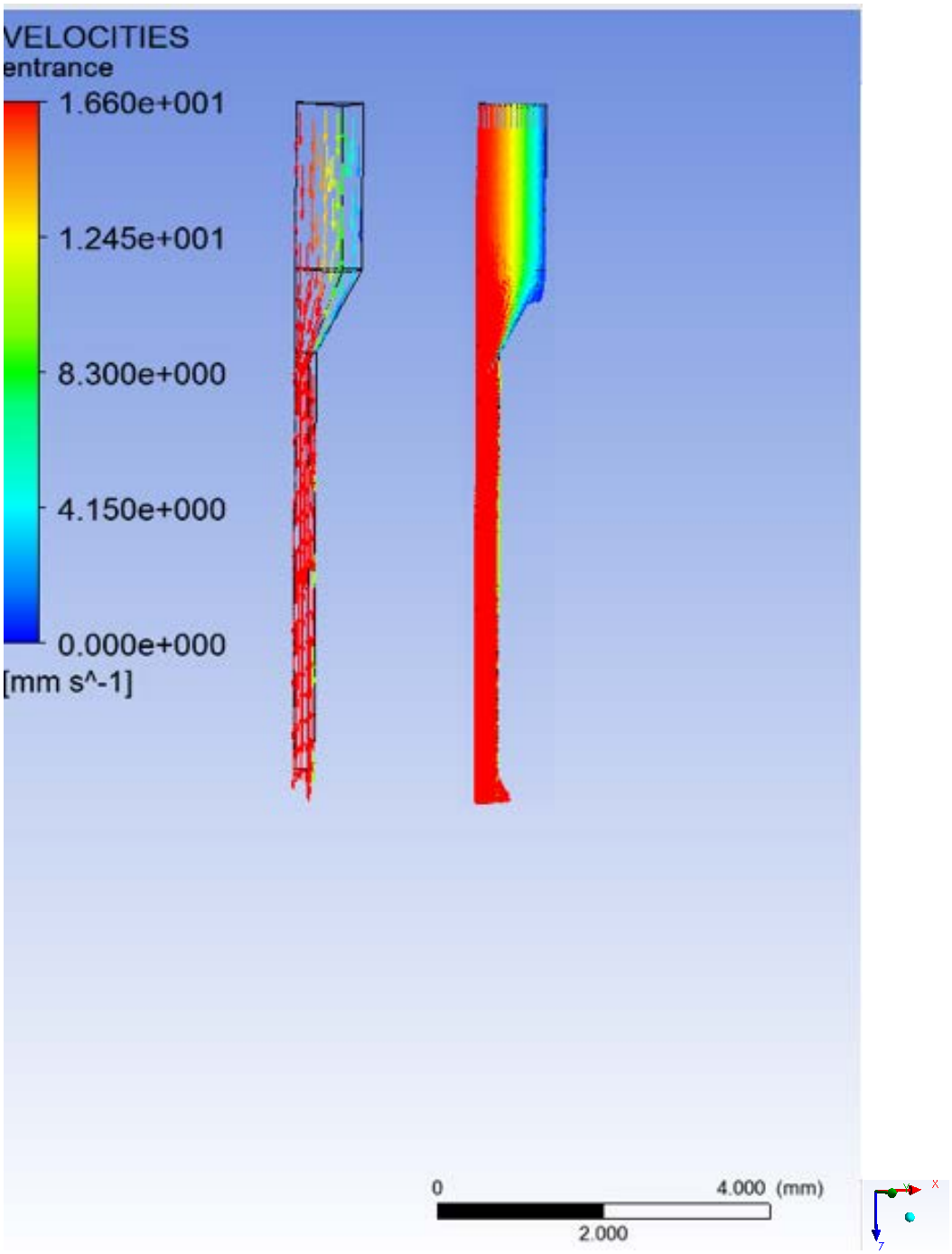

Figure 3.8: Velocity vectors from barrel to capillary at barrel diameter= 1.6 mm-visual on the right shows vector hundred fold denser

Modeling the single capillary fiber extrusion set up across various barrel diameters provided insight into the impact of the degree of contraction, from barrel to capillary. Lower contraction (i.e. smaller barrel diameter) resulted in higher computational accuracy as seen in declining centerline to wall shear rate ratio, in addition to reduced vortex formation areas, which are more desirable than large vortices. The counterbore served as a transition region between the barrel and capillary, to help alleviate the contraction effects, as indicated by capillary entrance profiles nearly overlapping. Overall, a good agreement was observed between ANSYS and analytically calculated pressure drops, fully developed velocities, and wall shear rates. Therefore, more complicated geometries were examined next.

3.3: Fiber Extrusion Including Filter

In melt-spinning, the addition of filters lead to added flow resistance. Sintered metal meshes lead to significant pressure drop, due to the reduction of area through fine filter pores. In this section, the effect of an added filter was examined by simplifying the geometry as a reduced flow area before the counterbore entrance.

The geometry consisted of 1.6 mm barrel, followed by a filter with 0.8 mm inner diameter and 0.1 mm thickness, then a counterbore starting at 1.6 mm diameter merging to the capillary. The diameter of the capillary was 0.5 mm, with L/Ds of 1, 3, 5, and 10. Fluid viscosity was set to 1 Pa.s and flow rate $Q=2.08 \times 10^{-9}$ m^3/s, hence an analytically calculated wall shear rate (equation 2-6) of 1358 1/s. Comparisons with the geometric counterparts not incorporating the filter were also carried out to assess the flow effects from its addition.

The centerline to wall shear ratio did not show significant change after adding the filter. Respectively, the centerline to wall shear ratios without and with the filter were 4 to 3% and 4 to 2.5% (Table 3.2). Thus, the presence of the new filter did not show a discernible effect on capillary wall shear rate. With longer capillaries, the centerline to wall shear ratio deviation decreased.

Table 3.2: Shear Rate Comparisons With and Without Filters

L/D	capillary length, Z (mm)	**Wall shear rate (1/s) w/ filter**	**Centerline Shear Rate (1/s) w/ filter**	**Wall shear rate (1/s) w/o filter**	**Centerline Shear Rate (1/s) w/o filter**
1	0.5	1328	52.70	1332	56.58
3	1.5	1328	40.95	1344	33.28
5	2.5	1334	41.03	1338	33.10
10	5.0	1338	41.12	1335	34.27

Analytical calculations applied to the fully developed region in capillary yield 170 mm/s center line velocity (equation 2-7), which showed a negligible difference from ANSYS calculations. A parabolic profile along the radius is maintained throughout the length of the capillary until the vectors spread apart at the exit (Figure 3.9).

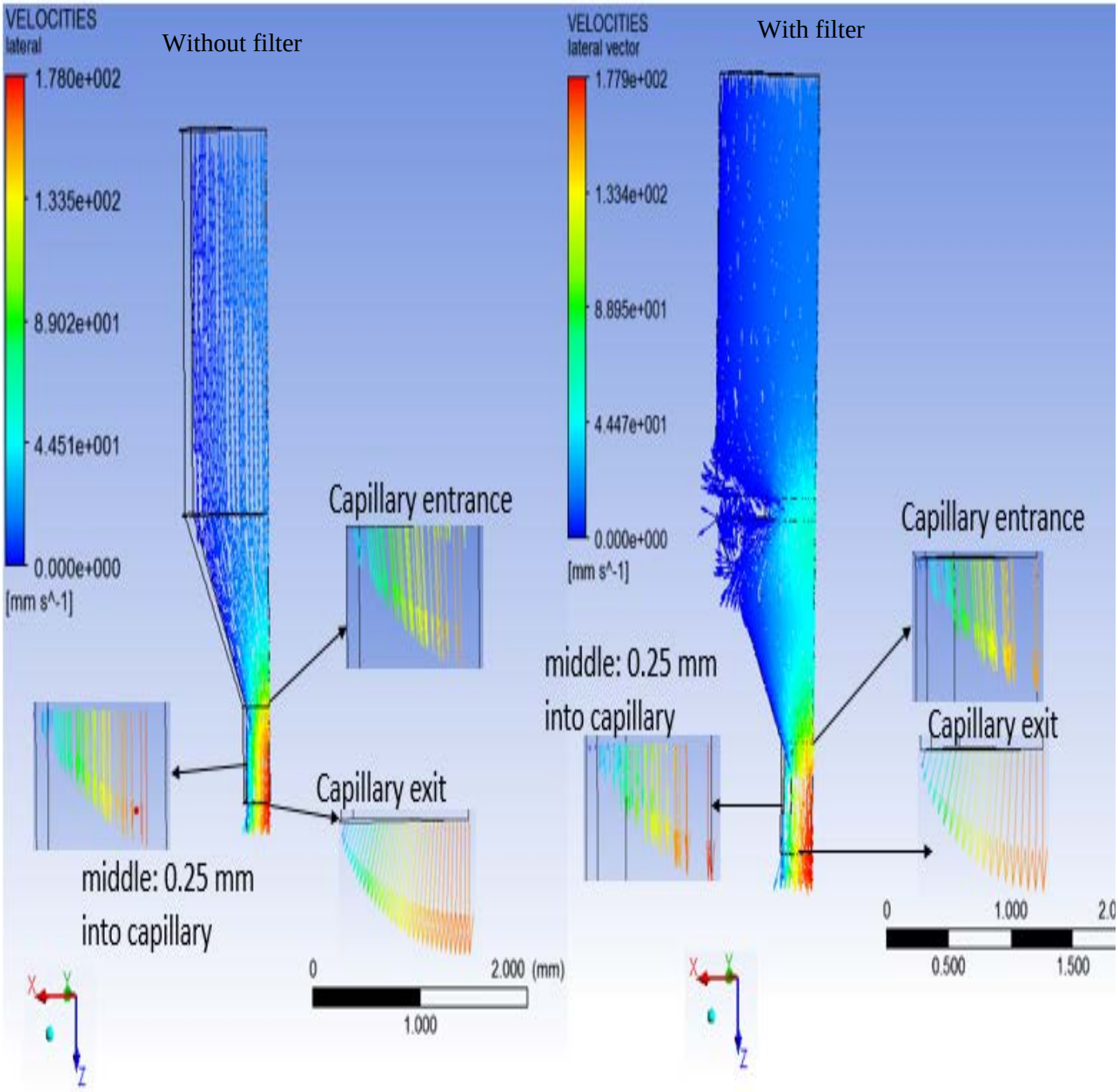

Figure 3.9: Velocity vectors focused on capillary region for geometries with and without filter at capillary L/D= 1

Pressure drop examined from the barrel entrance to capillary exit at the centerline showed similar profiles with and without a filter. A nearly negligible pressure drop was seen through the barrel, followed by a gradual decay through the filter contraction and counterbore, and concluded with a linear drop to zero from capillary entrance to exit . Barrel entrance pressure ranged from 7.58 to 57.2 kPa, and pressure in the capillary entrance ranged from 5.15 to 57.2 kPa, through all L/Ds (Table 3.3). The difference between ANSYS and analytically calculated capillary pressure drops (Equation 2-9), ranged from 0.8-11% through all L/Ds. Barrel to counterbore entrance pressure drop did not show any clear changes between L/Ds. However, it was ~30% larger with the filter, due to the extra contracted flow area.

Table 3.3: Pressure Comparisons With and Without Filters

L/D	capillary length, Z (mm)	Analytical Pressure Drop (kPa)	**Barrel Entrance Pressure (kPa) w/ filter**	**Capillary Entrance Pressure (kPa) w/ filter**	**Barrel Entrance Pressure (kPa) w/o filter**	**Capillary Entrance Pressure (kPa) w/o filter**
1	0.5	5.43	8.27	5.15	7.58	5.17
3	1.5	16.3	19.1	16.1	18.5	16.1
5	2.5	27.2	30.0	26.6	29.3	26.9
10	5.0	54.3	57.2	54.0	56.5	54.0

The barrel exit was a region of interest for comparison, since it directly shows the effect of the filter on the flow field. ANSYS velocity calculations, without the filter, yielded centerline velocities of 22.1 mm/s (Figure 3.10), whereas calculations with the filter showed an over two-fold increase in velocity of 55.6 mm/s. At the counterbore entrance, flow field visuals for the filter geometry showed longer velocity vectors compared to the geometry without it. Throughout the rest of the counterbore, the vectors merged closer together, toward the centerline. However, at similar lengths, the presence of a filter led to larger velocities as shown by the longer, lighter colored vectors (Figure 3.11).

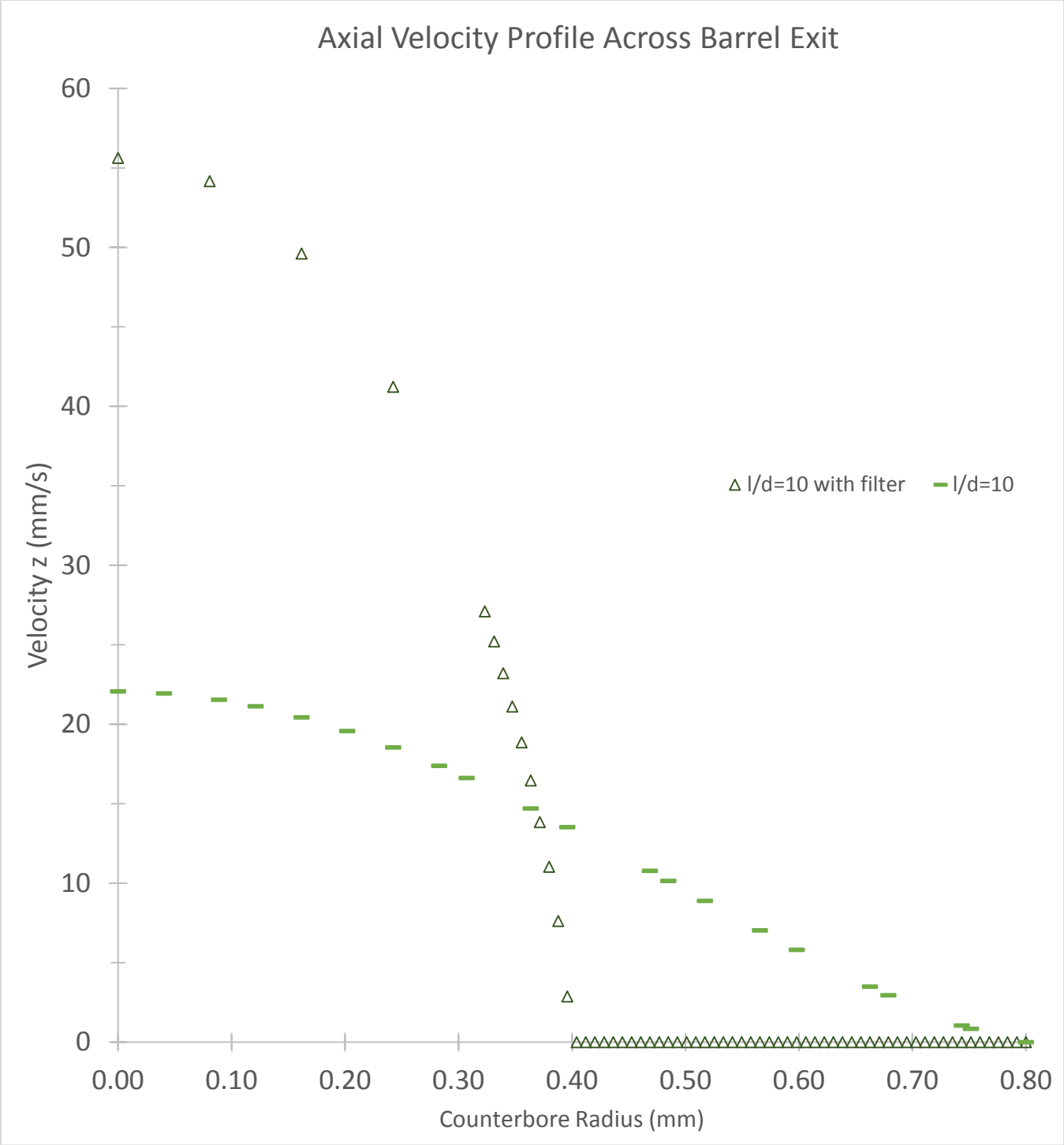

Figure 3.10: Z direction velocities along radius at the end of the barrel for geometries with and without filter

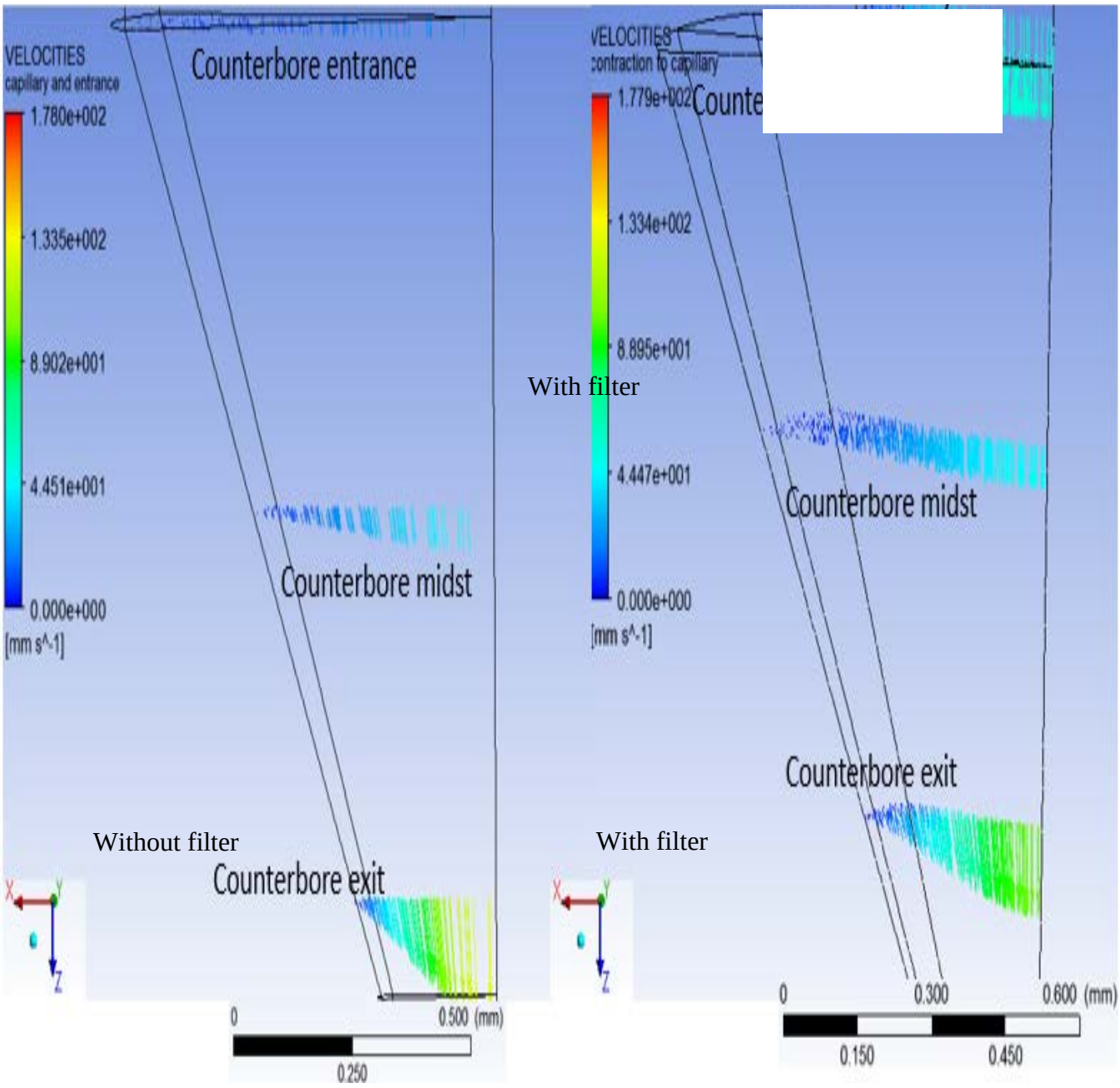

Figure 3.11: Velocity vectors in counterbore region for geometries with and without filter at capillary L/D=1

The predicted axial velocity along the barrel radius showed a peak velocity of 16.6 m/s , with negligible difference from the analytical calculations (Equation 2-7). For the setup without the filter, velocity vectors show flow mostly aligning with the geometry, due to the low barrel to counterbore to capillary diameter proportions (Figure 3.12). In addition, vortex formation was imperceptible (Figure 3.13). The modified geometry showed the flow converging right around the filter walls (Figure 3.12) and vortex formation was noted at the upper corners of the counterbore (Figure 3.13). The vortex formation resulted from the filter being modeled as a contraction. Thus, this simplification considered the filter porosity. However, the overall filter permeability was not factored into the flow.

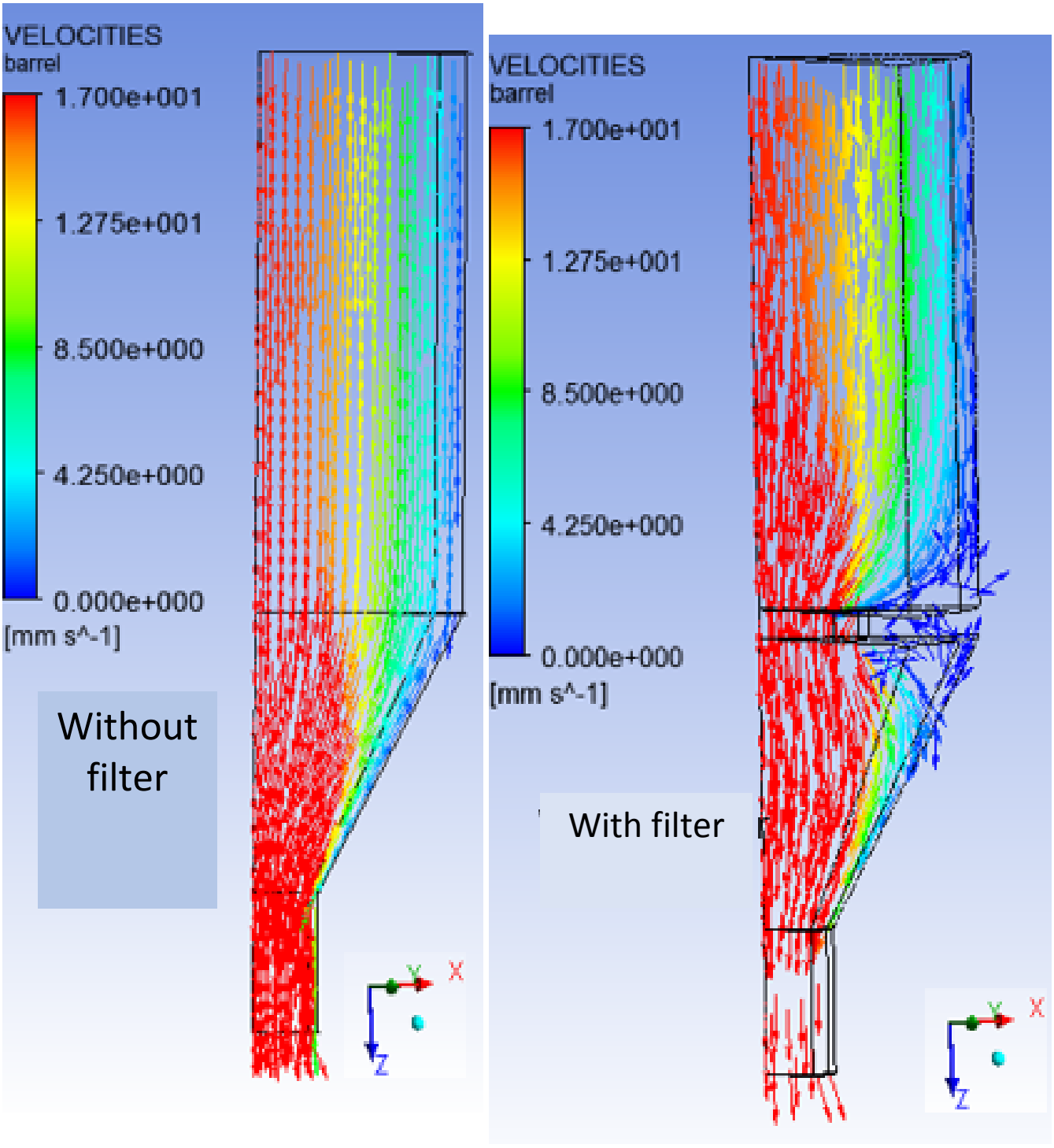

Figure 3.12: Lower density of vectors in flow field focused on barrel with capillary

L/D=1

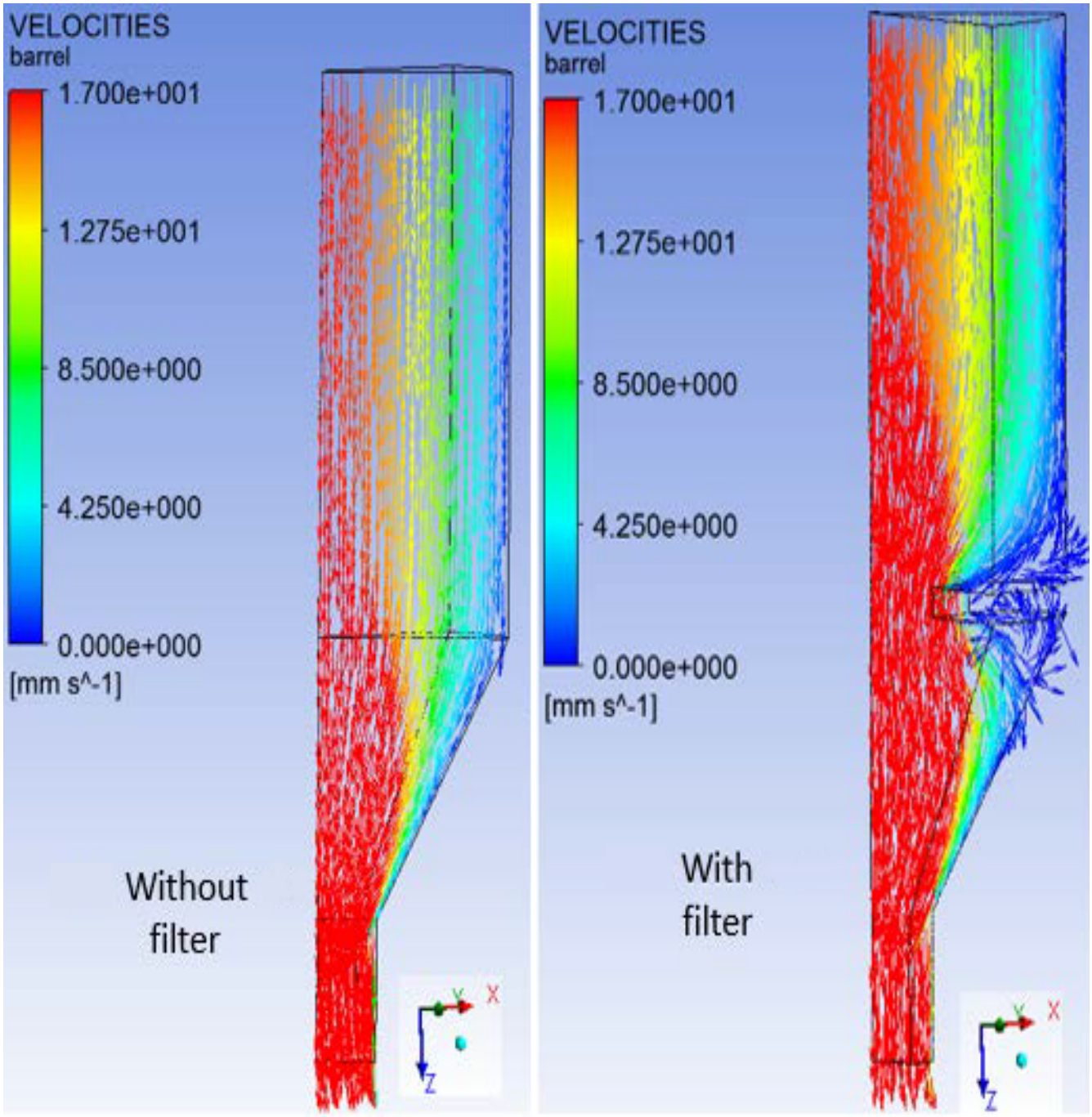

Figure 3.13: Higher density of vectors in flow field focused on barrel with capillary

L/D=1

Overall, incorporating the filter into the single capillary spinneret model resulted in a ~ 30% increase in pressure drop, from barrel to capillary entrance. No discernible impact of the filter on capillary pressure drop was indicated. Thus, there was good agreement between ANSYS and analytically calculated capillary pressure drops, centerline velocities, and wall shear rates.

3.4 Eccentric Counterbore-Capillaries

For high yield mesophase pitch fiber production, spinnerets consisting of multiple fine capillaries are used in melt-spinning. As a consequence of imprecise machining, these ultra-fine capillaries (50-150 μm diameter) can get drilled slightly off-center with respect to the counterbore. To determine the effects of such machining imprecision, simulations were conducted with eccentrically placed capillaries, with respect to the counterbore.

The spinneret consists of twelve positionally alternating capillaries. With the geometry reduced to a one-sixth sector, two capillary halves are positioned on the symmetry planes, as well as a whole one within the counterbore area. The capillaries halves remained in a fixed location (R_1), while the whole capillary was positioned at various points along the counterbore (R_2). The distance between R_1 and R_2 was denoted by X. Counterbore diameter was 3 mm, capillaries' diameter of 0.15 mm, unit viscosity (η= 1 Pa.s), and flow rate for a sixth of the geometry was $Q=5.11 \times 10^{-9}$ m^3/s (Figure 2.10.

Given that simulations were conducted for flow through multiple radial locations, it was of interest to compare the capillary entrance velocity profiles, considering all

component velocities. At capillary entrance, the velocities formed a parabolic profile along the diameter. The centerline velocity was 257 mm/s for all values of X. Thus no significant impact of capillary placement on its flow field was observed. The z-direction mid-capillary velocities at a given radial location displays no significant trend for various centerline displacements of capillaries. The ANSYS centerline velocities,290-293 mm/s, had a 0.2-1.1% difference from the analytically calculated velocity (equation 2-7). The proximity of ANSYS velocities at all values of X showed that capillary placement also had no observable effect on flow in the capillary mid-length.

Also of interest was the impact of inter-capillary distance on pressure drop. Pressure changed only along the axial direction, remaining constant radially throughout the counterbore and capillaries. Counterbore to capillary exit pressure drop was examined at the R_2 capillary centerline. Constant pressure was observed throughout the counterbore, and then started to gradually decline 0.02 mm from its exit. Capillary pressure plummeted at a linear rate to about zero at the outlet. The pressure drop profiles were similar for all inter-capillary distances. When the capillary length was shortened from L/D= 10 to 1 at, X=0.521 mm, the pressure drop was proportionally reduced by a factor of 10. ANSYS capillary pressure drop showed a small difference of 1.6%, from analytical calculations (Equation 2-9).

The vectors in Figures 3.14 showed that flow profile remains parabolic through the length of the capillary. At the entrance, the vectors slightly merged toward capillary centerline. In the mid-capillary region, the vectors are parallel to each other, with a rise in

centerline velocity. Once it reaches the exit, the vectors diverged from each other in open space.

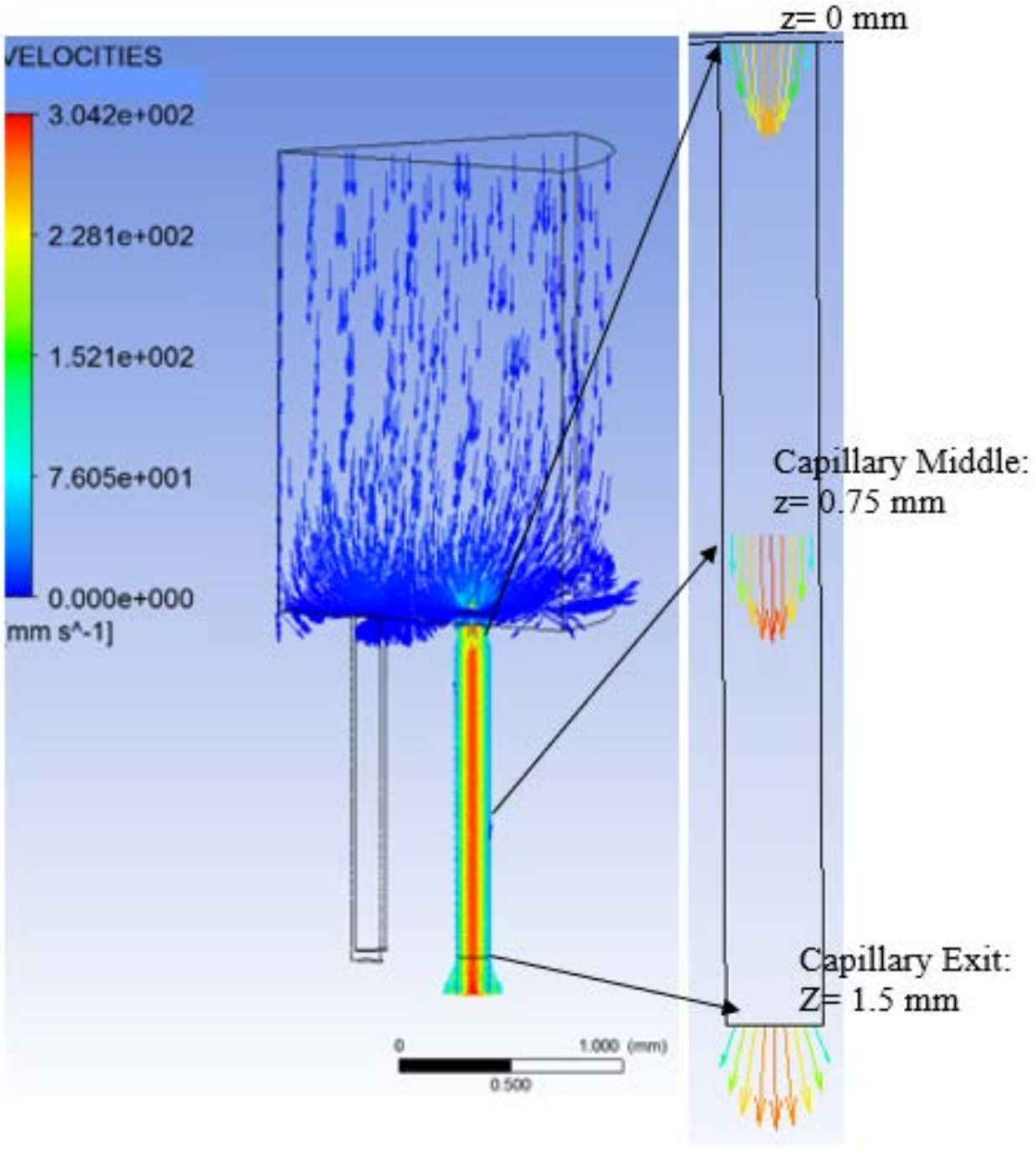

Figure 3.14: Capillary vectors at selected locations along its length

Since no significant impact of capillary placement on internal capillary flow was noted, flow near the end of the counterbore became of interest. Counterbore flow fields were initially examined on the plane dividing the geometry from a one-sixth to a one-twelfth sector, which cut through the R_2 capillary (Figure 3.15). The resulting flow fields highlight velocity vectors from the counterbore towards the R_2 capillary, at z =-0.2 mm (0.2 mm away from the exit) (Figures 3.16 and 3.17). The peak velocities showed a significant shift away from counterbore centerline. Instead, they approached closer to the radial location for the R_2 capillary, at that given value of X. The global maximum dropped from 34.8 mm/s to 28.2 mm/s at X=0.23 to 0.37 mm, and gradually decreased to 26 mm/s at X=0.79 mm (Figure 3.18).

Counterbore velocity vectors at X=0.231 and 0.374 mm was initially axial, and then merged toward the capillaries, with vortex formation at the corner of the two walls (Figure 3.16). The corresponding velocity profiles is parabolic for X= 0.231 mm, with different centerline and counterbore wall values. However, at X=0.374 mm, the beginning of the formation of another maximum, at the X=0.231 peak location, was observed (Figure 3.18).

At X=0.52 and 0.79 mm, the vectors formed a division in the flow (Figures 3.17), as shown by maxima formation in the velocity profiles, also at the X= 0.231 mm peak location. Flow division became more pronounced at X= 0.79 mm (Figure 3.18). The formation of these secondary maxima occur where more vortices develop in the space between the R_1 and R_2 , with the exception of X= 0.23 mm. At X=0.23 mm, the R_2

capillary was collinear with the R_1 capillaries, hence not providing enough room for additional vortex formation.

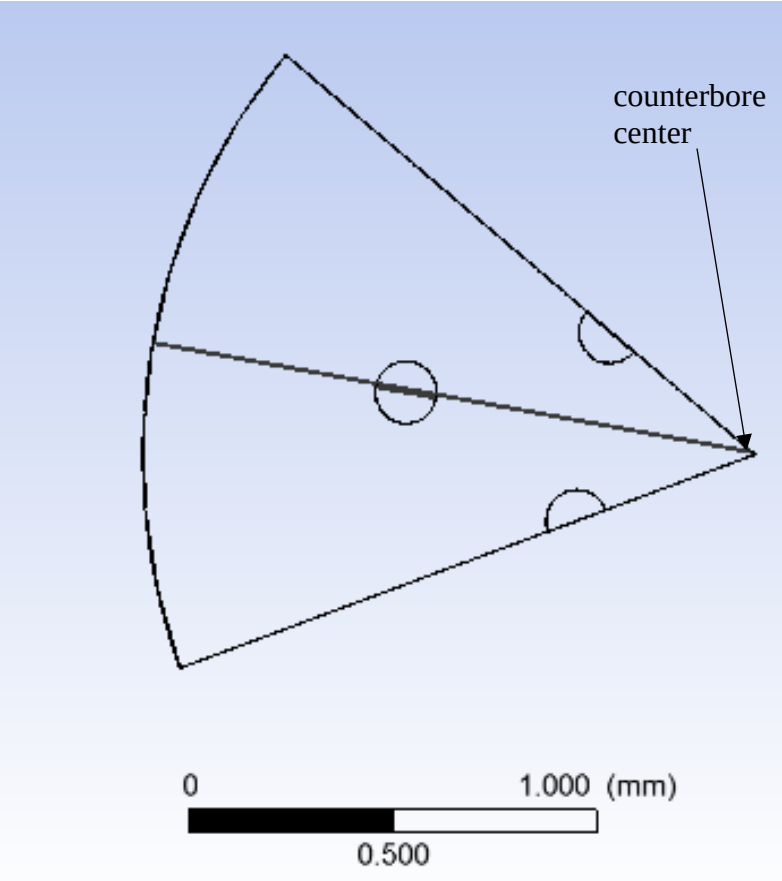

Figures 3.15: R_2 Plane-Cross-section of plane splitting through half of one-sixth geometry. Currently pictured is the R_2 capillary at X=0.52 mm from the R1 capillaries

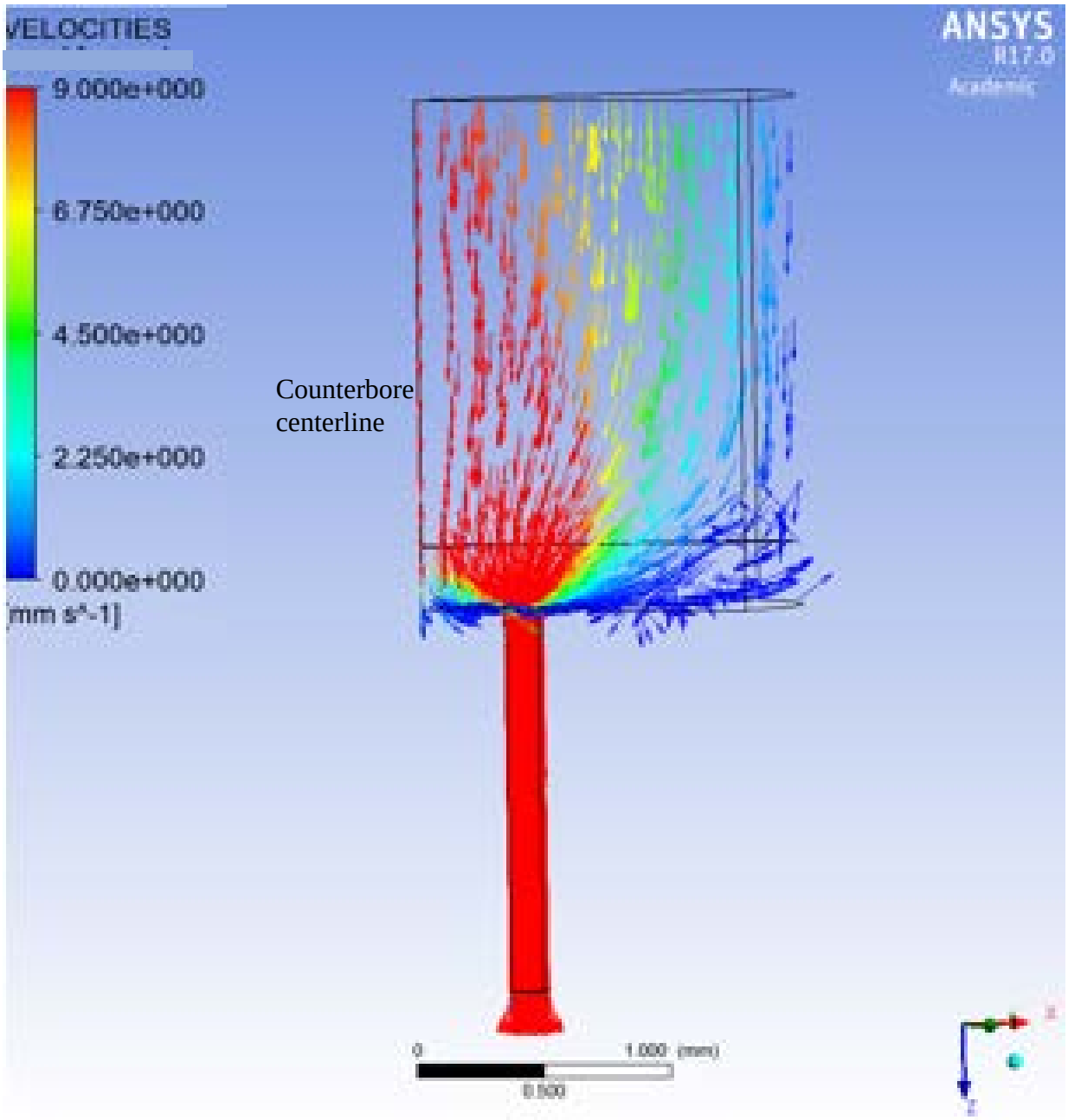

Figure 3.16: Vector flow field through R_2 at X=0.231mm

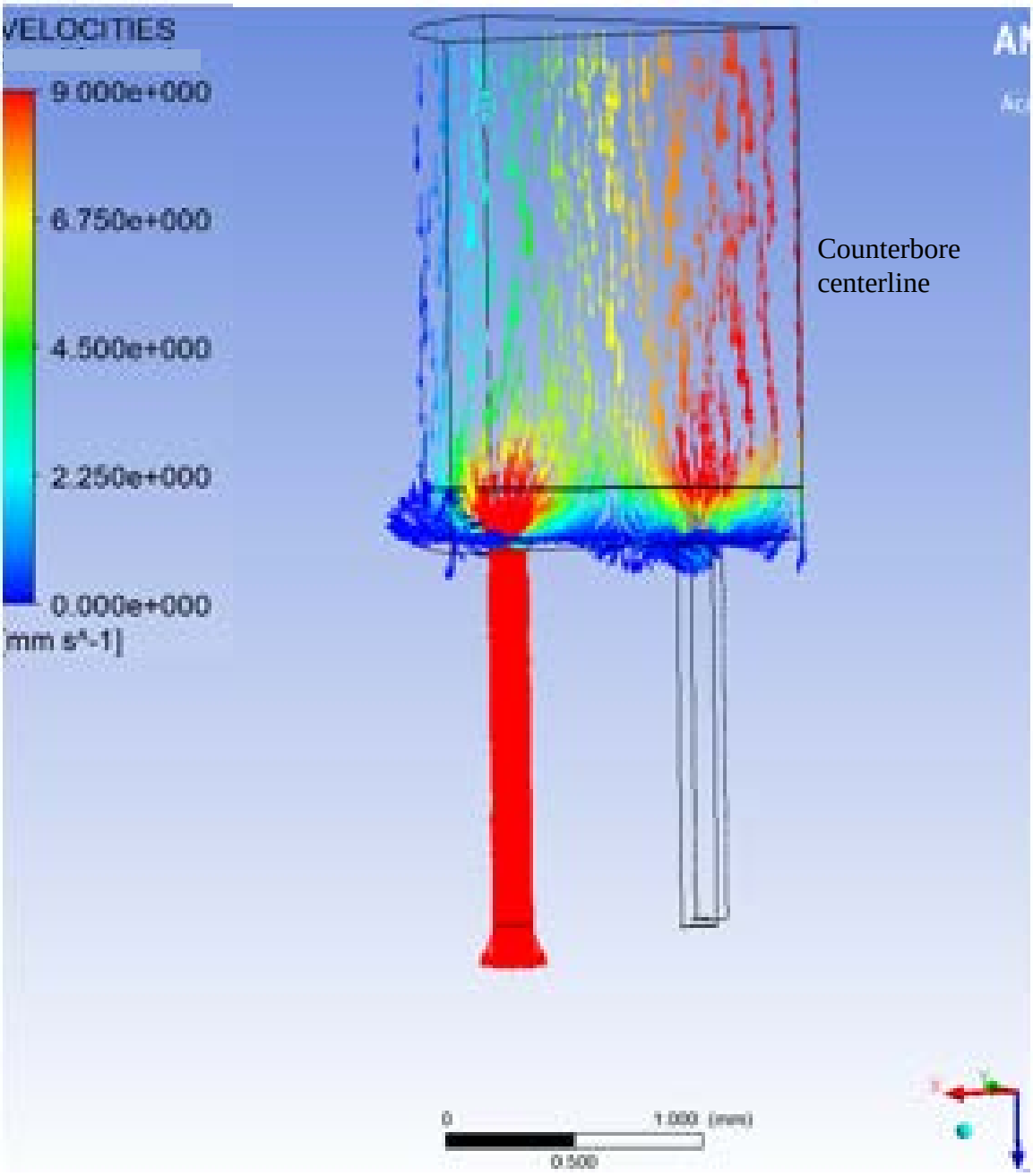

Figure 3.17: Vector flow field through R_2 at X=0.79 mm

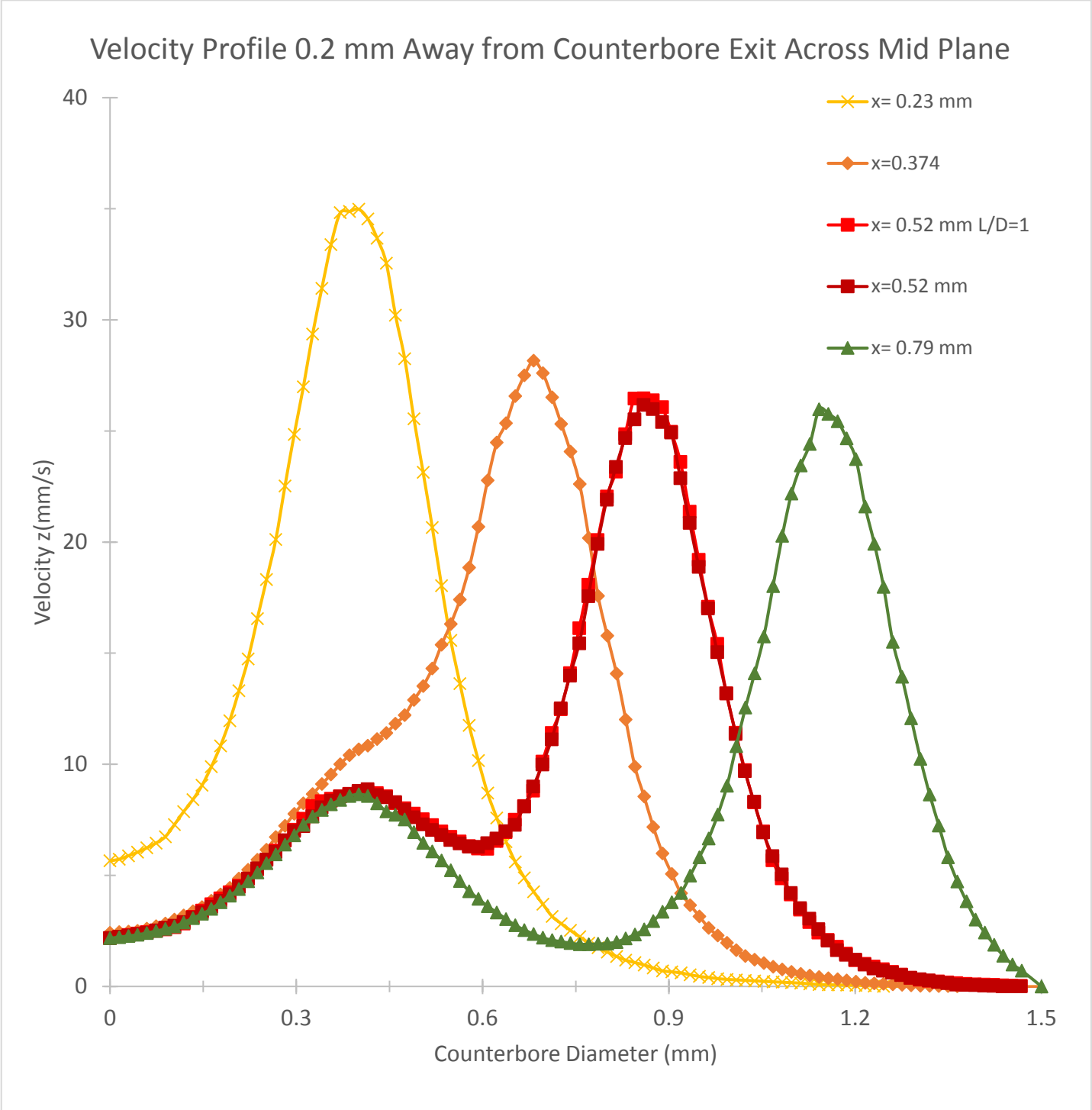

Figure 3.18: Axial velocity profiles through flow field on R_2 plane, 0.2 mm away from capillary entrance

Flow field through the counterbore was also examined on a plane of symmetry, where the full geometry was divided to one-sixth, and cut through an R_1 capillary (Figure 3.19). The maxima for all values of X shared the same radial location. The maximum velocity dropped from 36 to 29 mm/s at X=0.37 and 0.23 mm and showed an gradually decreased from 28 to 27 mm/s at X=0.52 to 0.79 mm (Figure 3.21). The reduced flow to R_1 is another indicator in flow division between the capillaries. The flow fields show that initial velocity vectors were axial and proceeded to merge toward the direction of the capillary, with vortex formation at the corner of the two walls (Figure 3.20). The absence of additional vortex and maxima formation in velocity profiles, on a plane of symmetry, showed that flow fields merging toward the fixed R_1 capillaries are not significantly affected by the R_2 capillary placement.

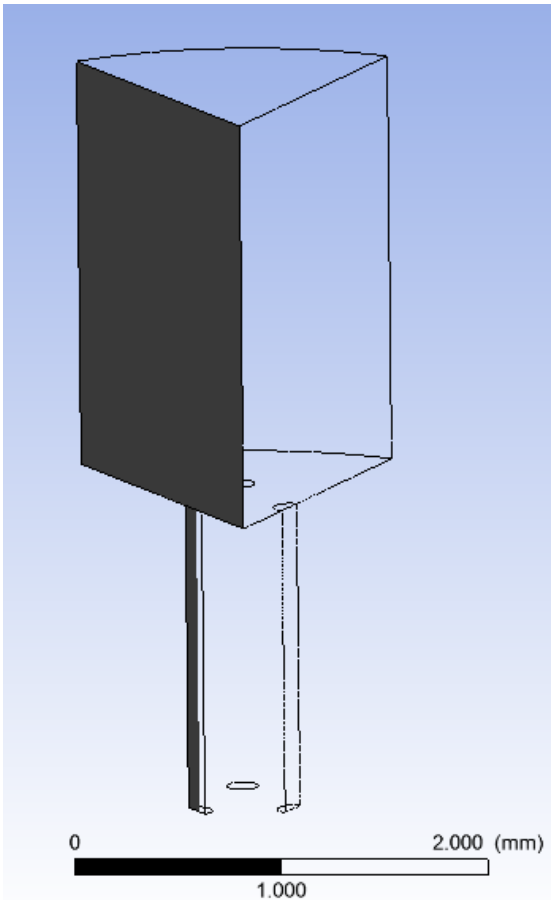

Figures 3.19: Plane of symmetry- one of the planes at which the full geometry is split into one-sixth. Currently pictured is the R_2 capillary at X=0.52 mm from the R1 capillaries

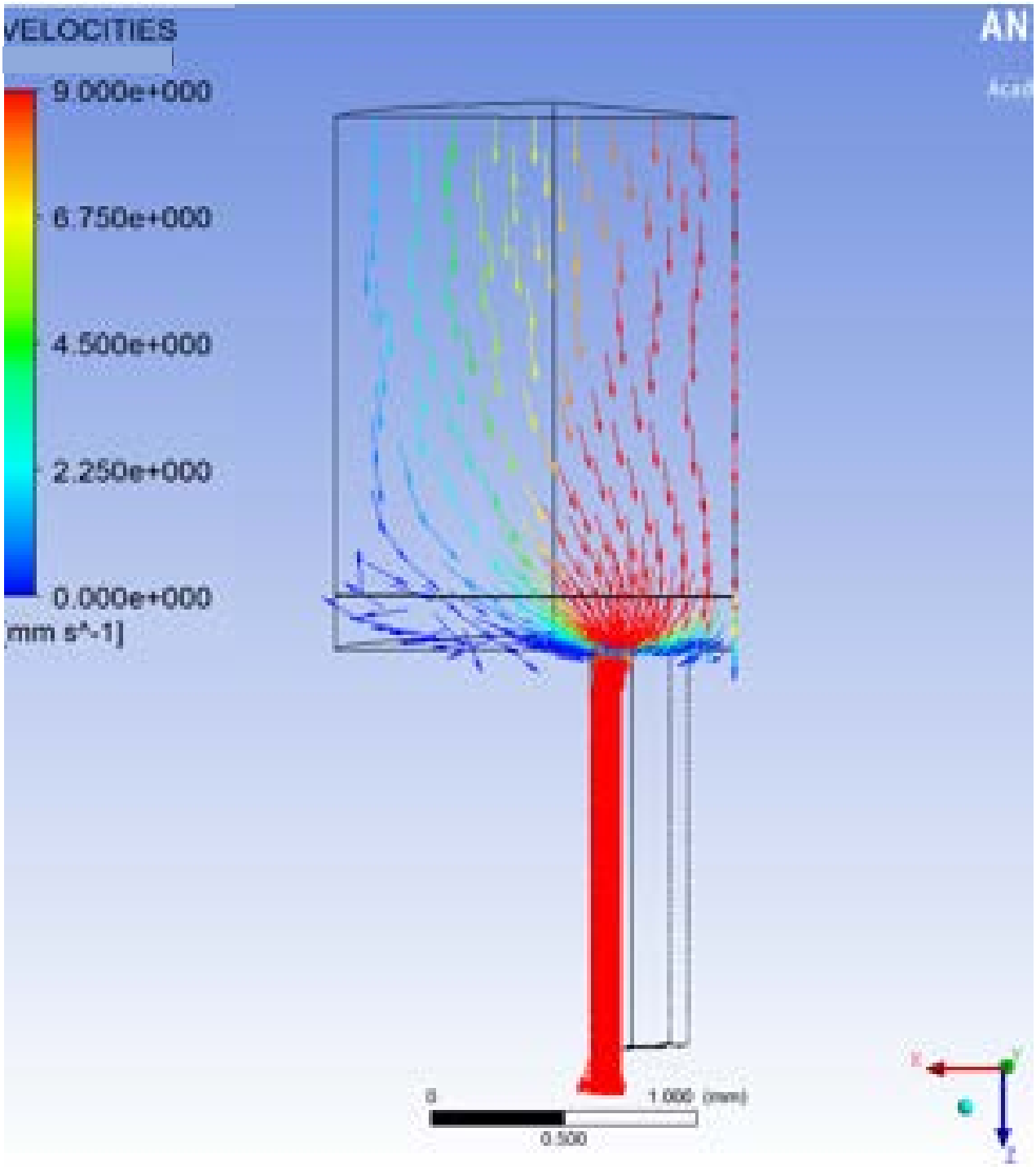

Figure 3.20: Vector flow field through R_1 at X=0.231mm

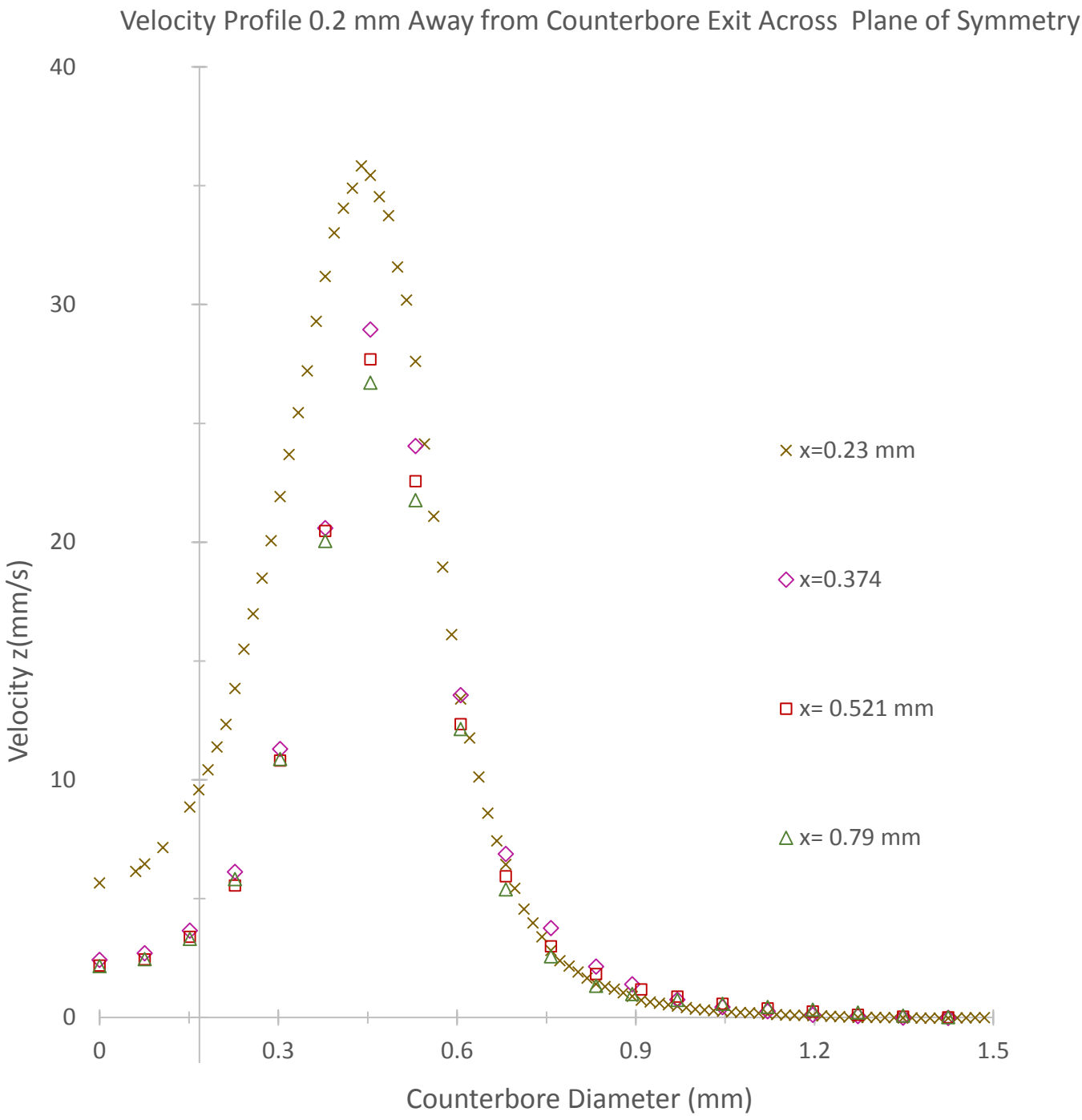

Figure 3.21: Axial velocity profiles through flow field on plane of symmetry, 0.2 mm away from capillary entrance

Modeling the eccentric counterbore-capillaries at various inter-capillary distances displayed more distinct flow divisions, with wider inter-capillary distance, on the velocity profiles. Once the capillaries were no longer collinear, an additional maximum in the counterbore velocity profiles before the R_2 capillary was formed. While the profiles of counterbore flow fields toward the R_1 capillaries did not change with increasing X, flow to R1 was slightly reduced. This was another indicator of flow division. A larger degree of flow division leads to larger areas of undesired vortex formation, hence the importance of maximizing precision in drilling capillaries.

CHAPTER 4
CONCLUSIONS AND FUTURE RECOMMENDATIONS

CONCLUSIONS

The primary objective of this study was to examine flow patterns through complex die geometries, using FEA-based simulations. This entailed modeling a single capillary spinneret, a spinneret including a filter, and off-center counterbore-capillaries The results of this study led to the following conclusions:

- The basic fiber-spinning model showed that reducing barrel to counterbore contraction (i.e. reducing barrel diameter) yielded more computational accuracy, as well as more desired flow patterns. The ratio of centerline-to-wall capillary shear rate ratio approached closer to zero, and velocity vectors displayed smaller area of vortex formation.
- Insertion of the annular filter at the barrel exit yielded ~30 % increase in pressure drop from barrel to counterbore exit. However, no significant change was observed in capillary pressure drop. Due to the additional contraction from the filter, vortices were formed at the upper corners of the counterbore.
- The eccentric counterbore-capillaries spinneret showed the flow field converging towards the capillaries. Larger distance between capillaries led to more pronounced multimodal velocity-radius profiles.
- ANSYS shear rates, pressure drops, and velocities showed good agreement with analytical calculations.

FUTURE RECOMMENDATIONS

This thesis approached modeling of complex flow geometries with a simple fluid model. However, it was not within the scope of this thesis to model complex fluid models through complex geometries. Thus, for future dissertation(s), complex flow geometries can be modeled using complex fluid models accounting for the discotic liquid crystalline behavior and microstructure of mesophase pitch, such as that based on constitutive equations developed by Singh and Rey [1998].

REFERENCES

Arai Y (1993). Structure and Properties of Pitch-based Carbon Fibers. Nippon Steel Technical Report No. 59 October 1993: 65–70.

Bird, R. B., Stewart, W. E., & Lightfoot, E. N. (2007). Transport Phenomena, 430.

Bermudez,Victor; Lukubira, Sam; Ogale, Amod (2018) 1.3 Pitch Precursor-Based Carbon Fibers. In: Beaumont, P. W.R. and Zweben, C.H. (eds.), Comprehensive Composite Materials II. vol. 1, pp. 41–65. Oxford: Academic Press

Brandao, J., Spieth, E., & Lekakou, C. (1996). Extrusion of polypropylene. Part I: Melt rheology. *Polymer Engineering & Science*, *36*(1), 49-55.

Castro, L. D. D. (2006). Anisotropy and mesophase formation towards carbon fibre production from coal tar and petroleum pitches: a review. *Journal of the Brazilian Chemical Society*, *17*(6), 1096-1108.

Cato, A. D., & Edie, D. D. (2003). Flow behavior of mesophase pitch. *Carbon*, *41*(7), 1411-1417.

Cato, A. D., Edie, D. D., & Harrison, G. M. (2005). Steady state and transient rheological behavior of mesophase pitch, Part I: Experiment. *Journal of Rheology*, *49*(1), 161-174.

Chang, Ping-Wu, Thomas W. Patten, and Bruce A. Finlayson. "Collocation and galerkin finite element methods for viscoelastic fluid flow—II. Die swell problems with a free surface." *Computers & Fluids* 7, no. 4 (1979): 285-93

Diefendorf, R.J (2000). “Pitch Precursor Carbon Fibers”. *Comprehensive Composite Materials*. Kelly, A., Zweben, C. Elsevier. pp. 44-50

Edie, D. D., & Diefendorf, R. J. (1993). Carbon fiber manufacturing. *Carbon-Carbon Materials and Composites*, 19-37.

Edie, D. D., Fain, C. C., Robinson, K. E., Harper, A. M., & Rogers, D. K. (1993). Ribbon-shape carbon fibers for thermal management. *Carbon*, *31*(6), 941-949.

Edie, D. D., & Dunham, M. G. (1989). Melt spinning pitch-based carbon fibers. *Carbon*, *27*(5), 647-655.

Figueiredo, J. L., Bernardo, C. A., Baker, R. T. K., & Hüttinger, K. J. (Eds.). (2013). *Carbon fibers filaments and composites* (Vol. 177). Springer Science & Business Media.

Fitzer, E.; Manocha, L. M (1998). Carbon Reinforcements and Carbon/Carbon composites; Springer: Berlin; pp 17-28.

Fleurot, O. (1998). The viscoelastic flow behavior of pitches.

Hurt, R. H., & Hu, Y. (1999). Thermodynamics of Carbonaceous Mesophase. *Carbon*, *37*(2), 281-292.

Jeon, Y. P., & Cox, C. L. (2008). Modeling of multifilament PET fiber melt-spinning. *Journal of applied polymer science*, *110*(4), 2153-2163.

Jeon, Y. P., & Cox, C. L. (2009). Simulation of Multifilament Semi crystalline Polymer Fiber Melt-Spinning. *Journal of Engineered Fabrics & Fibers (JEFF)*, *4*(1).

Jiang, Z., Jia, Z., Li, Z., Wang, J., Xiao, C., & Jin, J. (2014). A comparative study of rheological behavior of PET and PET/carbon black composite masterbatch. *Polymer bulletin*, *71*(12), 3197-3208.

Kulkarni, S. (2011). Quantitative analysis and structural characterization of carbonaceous pitches.

Kundu, S. (2006). Investigation of Flow and Microstructure in Rheometric and Processing Flow Conditions for Liquid Crystalline Pitch.

Liu, C. (2010). Mesophase Pitch-Based Carbon Fiber and Its Composites: Preparation and Characterization.

Matsumoto, T (1985). “Mesophase Pitch and Its Carbon Fibers.” *Pure and Applied Chemistry*, vol. 57, no. 11, pp. 1553–1562.,

Mochida, I., Korai, Y., Yoon, S. H., Fortin, F., Ling, L. C., & Kanno, K. (1993). High Performance, Moderate Cost Mesophase Pitch Based Carbon Fibers. *American Chemical Society Division Fuel Chemistry*, *38*, 436-436.

Mochida, I., Korai, Y., Ku, C. H., Watanabe, F., & Sakai, Y. (2000). Chemistry of synthesis, structure, preparation and application of aromatic-derived mesophase pitch. *Carbon*, *38*(2), 305-328.

Mochida, I., Yoon, S. H., & Korai, Y. (2002). Mesoscopic structure and properties of liquid crystalline mesophase pitch and its transformation into carbon fiber. *The Chemical Record*, *2*(2), 81-101.

Morgan, P. (2005). *Carbon Fibers and Their Composites*. CRC press. pp 189-190

Mu, Y., Zhao, G., Wu, X., & Zhai, J. (2011). Finite-Element Simulation of Polymer Flow and Extrudate Swell Through Hollow Profile Extrusion Die with the Multimode Differential Viscoelastic Model. *Advances in Polymer Technology*, *32*(S1), E1-E19.

Mu, Y., Zhao, G., Chen, A., & Wu, X. (2013). Modeling and simulation of three-dimensional extrusion swelling of viscoelastic fluids with PTT, Giesekus and FENE-P constitutive models. *International Journal for Numerical Methods in Fluids*, *72*(8), 846-863.

Nickell, R. E., Tanner, R. I., & Caswell, B. (1974). The solution of viscous incompressible jet and free-surface flows using finite-element methods. *Journal of Fluid Mechanics*, *65*(1), 189-206.

Park, S. J., & Heo, G. Y. (2015). Precursors and manufacturing of carbon fibers. In *Carbon Fibers* (pp. 31-66). Springer, Dordrecht.

Rand, B. (1985). Carbon fibres from mesophase pitch. *Elsevier Science Publishers B. V., Handbook of Composites.*, *1*, 495-575.

Singer, L. S. (1975). *U.S. Patent No. 3,919,387*. Washington, DC: U.S. Patent and Trademark Office.

Singh, A. P., & Rey, A. D. (1998). Microstructure constitutive equation for discotic nematic liquid crystalline materials. *Rheologica acta*, *37*(1), 30-45.

Villacorta, B. S., Hulseman, R., & Ogale, A. A. (2014). Viscoelastic Computational Modeling of Extruded Micro-textured Polymeric Films. *Procedia Materials Science*, *5*, 1460-1465.

Yang, C., & Li, Z. (2014). A study of wall slip in the capillary flow of a filled rubber compound. *Polymer Testing*, *37*, 45-50.

Yang, Kap Seung, et al (2014). “Pitch Based Carbon Fibers for Automotive Body and Electrodes.” *Carbon Letters*, vol. 15, no. 3, pp. 162–170.

Yoon, S. H., Korai, Y., Mochida, I., & Kato, I. (1994). The flow properties of mesophase pitches derived from methylnaphthalene and naphthalene in the temperature range of their spinning. *Carbon*, *32*(2), 273-280.

Yu, M., Luo, Y. S., Luo, W. B., & Peng, X. H. (2007). Numerical simulation and experimental study on rheological properties of polypropylene. *Journal of Central South University of Technology*, *14*(1), 151-153.

Appendix A: Off-center Counterbore Vectors Not Shown in Results Chapter

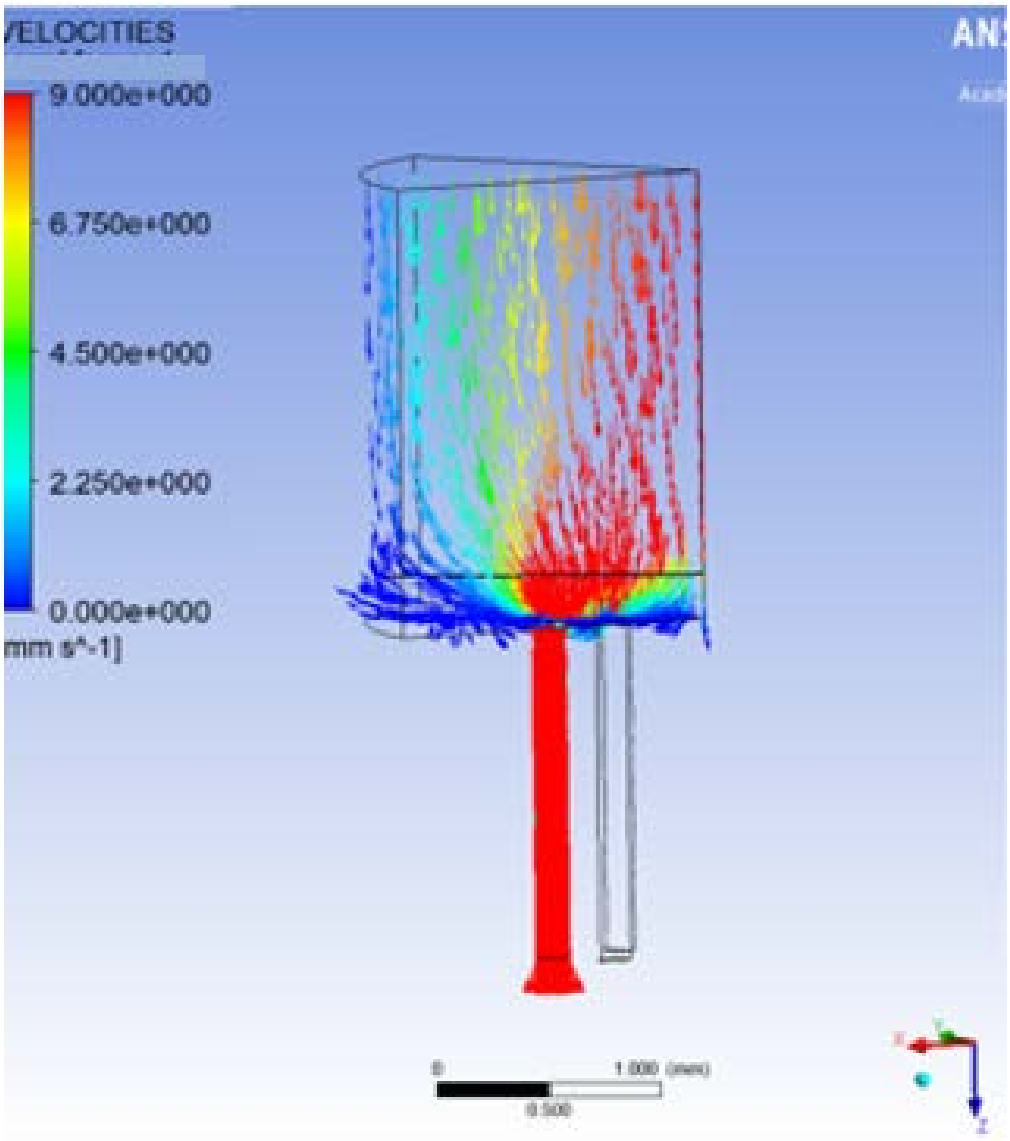

Figure A.1: Vector flow field through R_2 at X=0.374mm

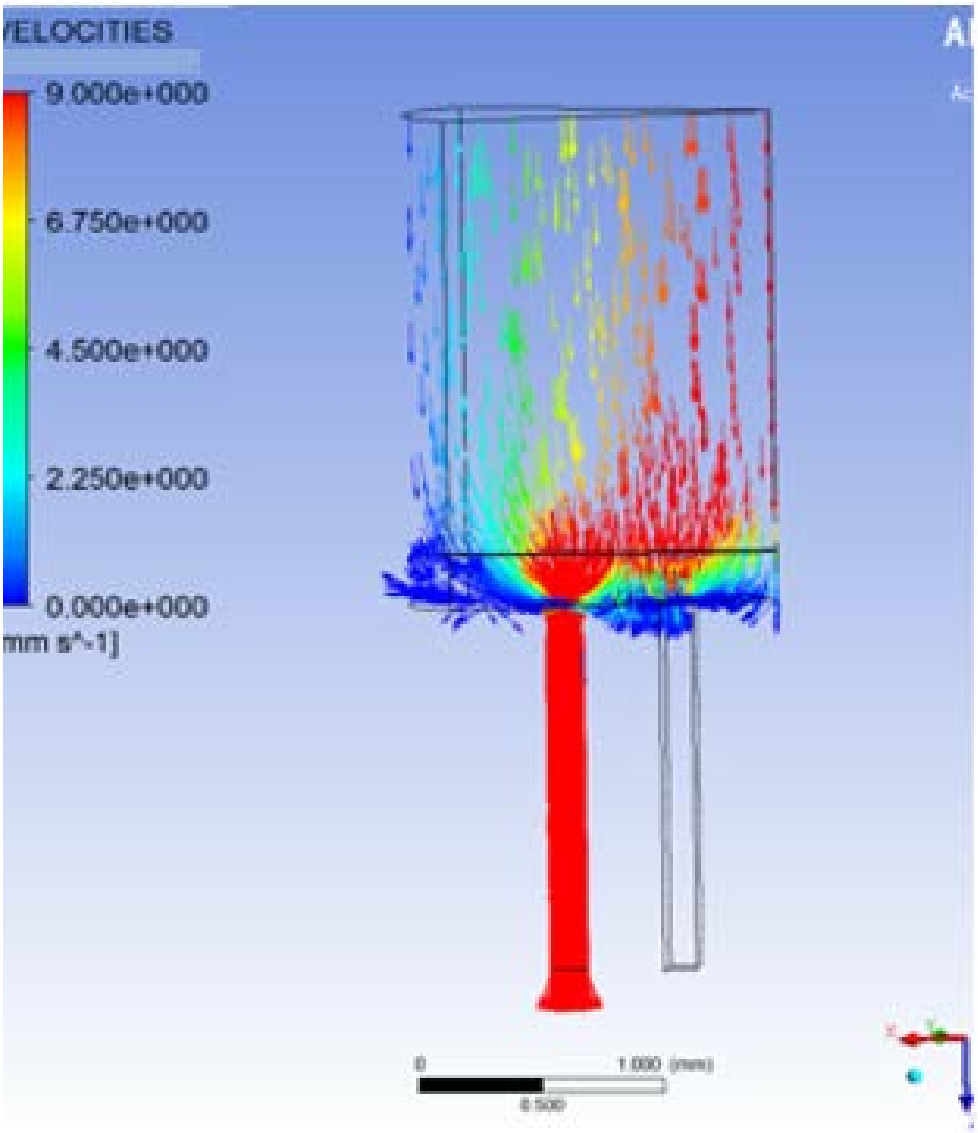

Figure A.2: Vector flow field through R_2 at X=0.52 mm

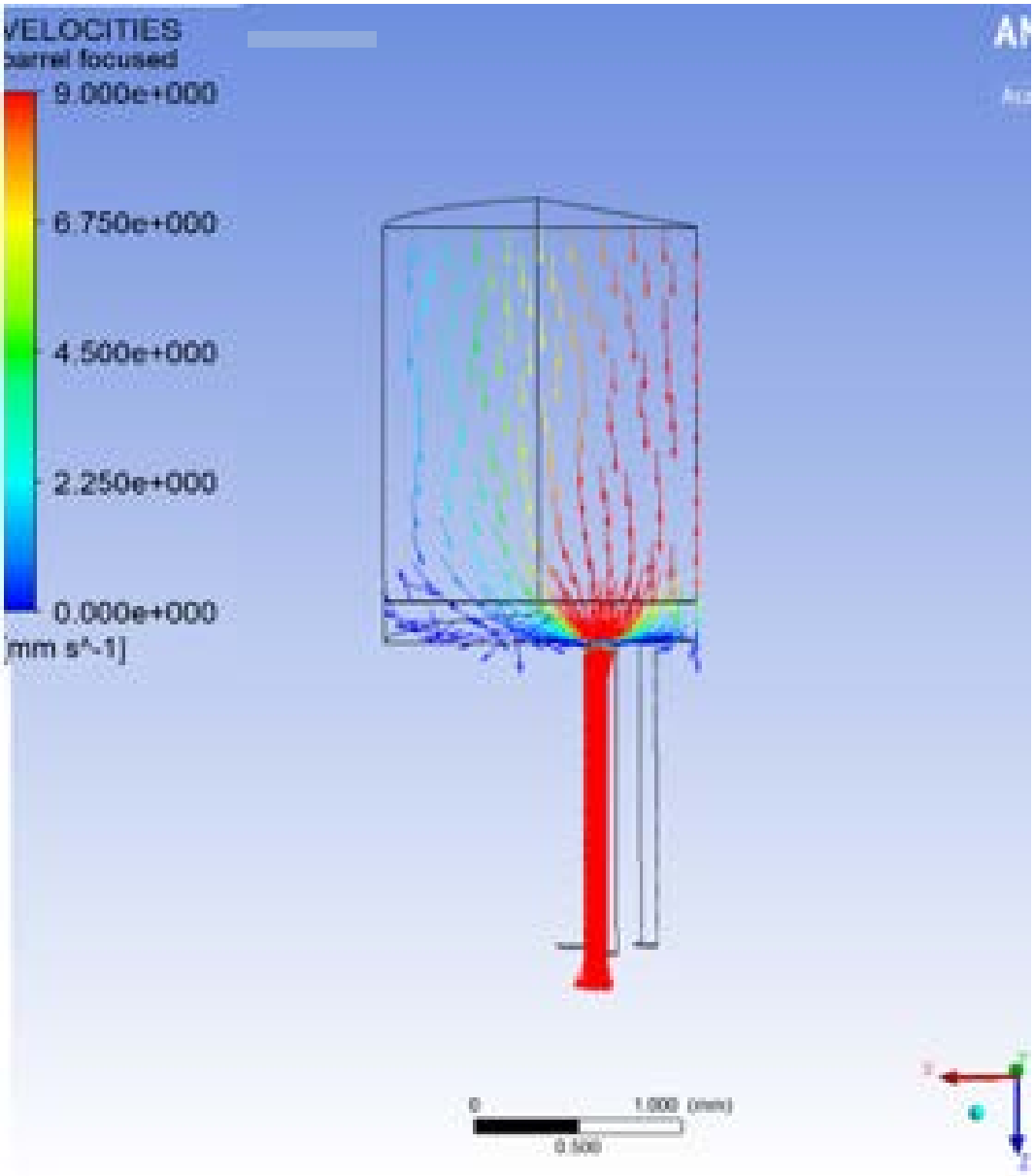

Figure A.3: Vector flow field through R_1 at X= 0.374 mm

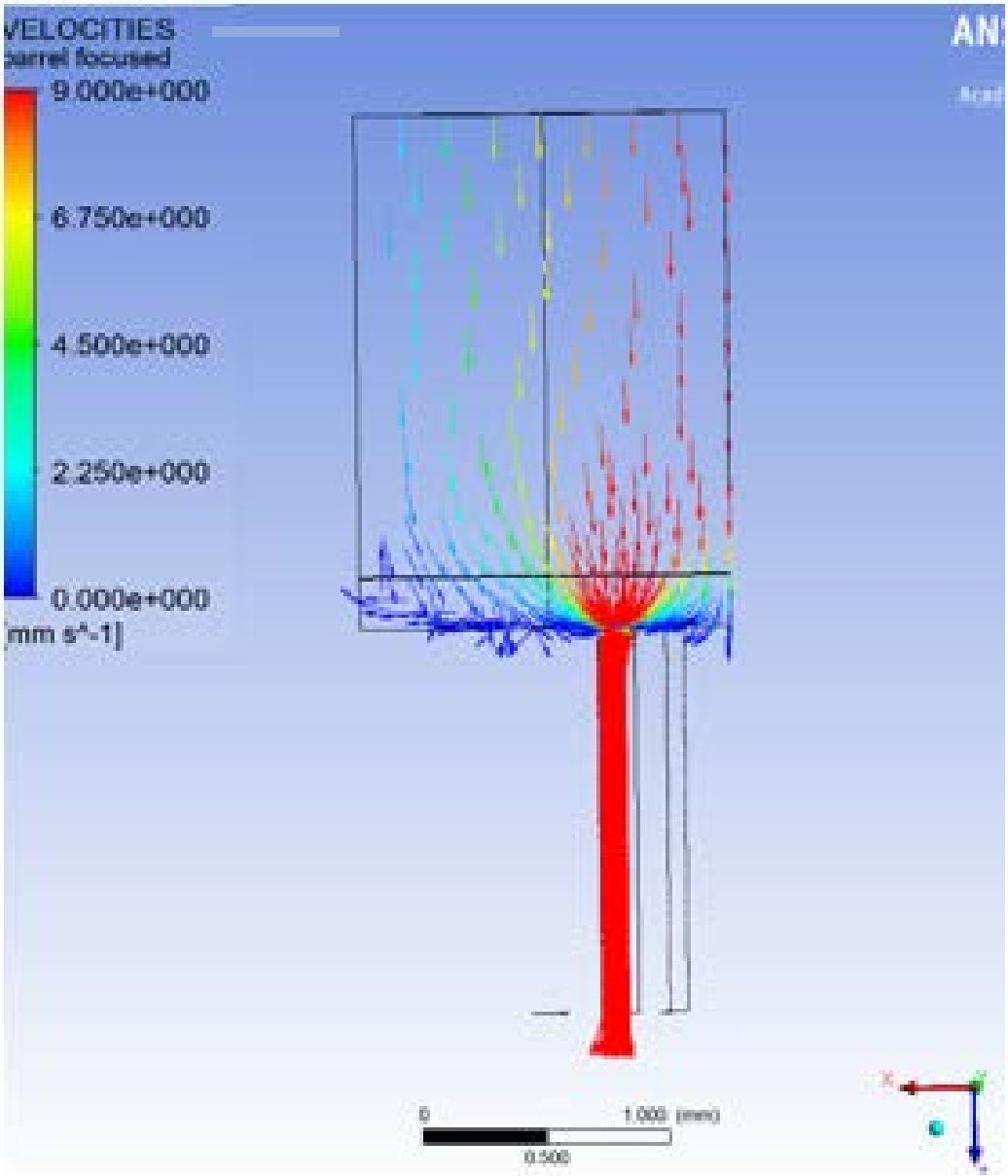

Figure A.5: Vector flow field through R_1 at X= 0.521 mm

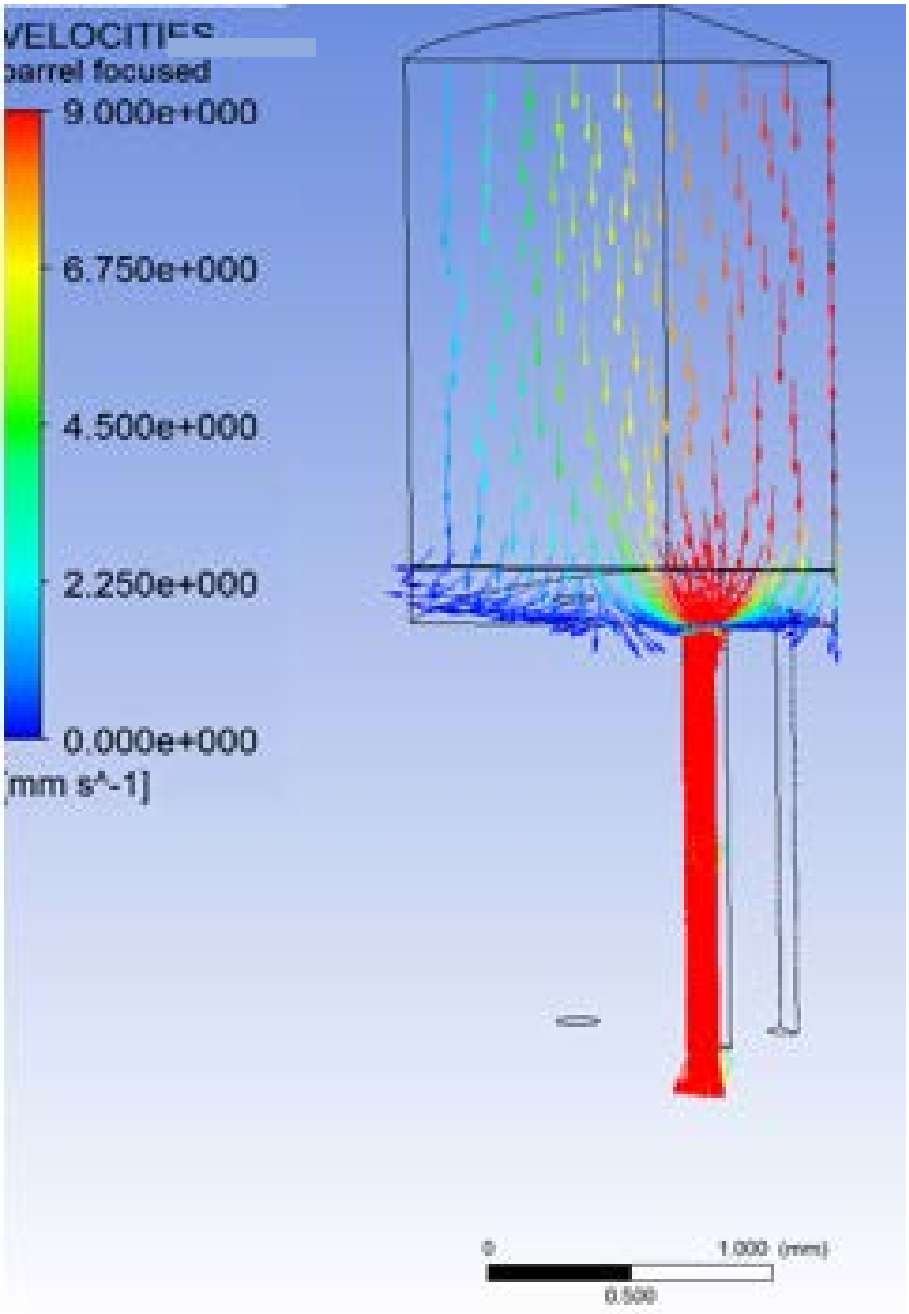

Figure A.6: Vector flow field through R_1 at X= 0.79 mm

Appendix B: Tabulated Results Including Other Barrel Diameters

Table B.1: Wall and Centerline Capillary Shear Rate Values for Single Capillary Spinneret, at Fixed Capillary Diameter

Barrel Diameter (mm)	Capillary L/D	**Wall shear rate (1/s) d=0.25 mm**	**Centerline Shear Rate (1/s)**
38	10	1301	105
30	10	1303	107
20	10	1323	67
10	10	1327	46
3	10	1344	32
1.6	10	1333	34
1.6	1	1333	55

Table B.2: Wall and Centerline Capillary Axial Velocity Values for Single Capillary Spinneret, at Fixed Capillary Diameter

Barrel Diameter (mm)	Capillary L/D	Element Size (mm)	Number of Elements	**Wall velocity (mm/s) d=0.25 mm**	**Centerline velocity (mm/s) d=0mm**
38	10	0.045	3,046,206	0	171
30	10	0.041	2,591,537	0	171
20	10	0.027	2,709,088	0	170
10	10	0.0185	2,511,497	0	170
3	10	0.0125	1,673,038	0	169.9
1.6	10	0.0135	1,068,552	0	169.9
1.6	1	0.0105	821,828	0	171.4

Table B.3: Pressure drop values for Single Capillary Spinneret 3.14 and 3.16

L/D	Barrel diameter (mm)	Number of elements	**Pressure Drop from Barrel Entrance (kPa)**	**Analytical Pressure at Capillary Entrance (kPa)**	**ANSYS Pressure at Capillary Entrance (kPa)**
10	38	3,046,206	56.6	54.3	53.6
10	30	2,591,537	56.6	54.3	53.6
10	20	2,709,088	56.5	54.3	53.5
10	10	2,511,497	56.4	54.3	53.4
10	3	1,673,038	56.3	54.3	53.4
10	1.6	1,068,552	56.5	54.3	53.4
1	1.6	821,828	7.58	5.43	5.14

Table B.4: Axial Velocity Profile at Capillary Entrance for Single Capillary Spinneret

Barrel Diameter (mm)	Capillary L/D	Element Size (mm)	Number of Elements	**Wall velocity (mm/s)**	**Center line velocity (mm/s)**
38	10	0.045	3,046,206	0	156
30	10	0.041	2,591,537	0	156
20	10	0.027	2,709,088	0	155
10	10	0.0185	2,511,497	0	154
3	10	0.0125	1,673,038	0	154
1.6	10	0.0135	1,068,552	0	154
1.6	1	0.0105	821,828	0	154

Table B.5: Axial Velocity Profile at Counterbore Entrance for Single Capillary Spinneret

Barrel Diameter (mm)	Capillary L/D	Element Size (mm)	Number of Elements	**Wall velocity (mm/s) d=0.25 mm**	**Center line velocity (mm/s)**
38	10	0.045	3,046,206	0	20.5
30	10	0.041	2,591,537	0	20.6
20	10	0.027	2,709,088	0	20.4
10	10	0.0185	2,511,497	0	20.3
3	10	0.0125	1,673,038	0	20.4
1.6	10	0.0135	1,068,552	0	22.1
1.6	1	0.0105	821,828	0	22.1

Table B.6: Axial velocity Profile at Barrel Entrance for Single Capillary Spinneret

Barrel Diameter (mm)	Capillary L/D	Element Size (mm)	Number of Elements	**Wall velocity (mm/s)**	**Center line velocity (mm/s)**
38	10	0.045	3,046,206	0	0.0291
30	10	0.041	2,591,537	0	0.0472
20	10	0.027	2,709,088	0	0.106
10	10	0.0185	2,511,497	0	0.424
3	10	0.0125	1,673,038	0	4.72
1.6	10	0.0135	1,068,552	0	16.6
1.6	1	0.0105	821,828	0	16.6

Table B.7: Mid Capillary Axial Velocity Comparisons With and Without Filters

L/D	capillary length, Z (mm)	Number of elements w/ filter	Number of elements w/o filter	**z center velocity (mm/s) w/ filter**	**z wall velocity (mm/s) w/ filter**	**z center velocity (mm/s) w/o filter**	**z wall velocity (mm/s) w/o filter**
1	0.5	2,495,818	474,912	170	0	171	0
3	1.5	2,548,297	606,832	170	0	170	0
5	2.5	2,623,194	738,752	170	0	170	0
10	5.0	2,796,348	1,068,552	170	0	170	0

Table B.8: ANSYS Wall and Centerline Capillary Shear Rate Values for Eccentric Spinnerets

Distance between capillaries at R_1 and R_2 (mm), **x**	Distance between Counterbore Centerline (mm)	L/D	Number of elements	Wall Shear Rate (1/s)	Center Shear Rate (1/s)
0	0.46	10		7404	544
0.231	0.400	10	857,162	7445	387
0.374	0.690	10	909,364	7455	388
0.521	0.867	10	934,934	7451	389
0.521	0.867	1	206,457	7391	537
0.790	1.156	10	947,212	7443	387

Table B.9: Wall and Centerline Capillary Z-Velocity Values for Eccentric Capillaries

Distance between capillaries at R_1 and R_2 (mm), **x**	Distance between Counterbore Centerline (mm)	L/D	Number of elements	Center axial velocity (mm/s)
0	0.46	10	_____	
0.231	0.400	10	857,162	290
0.374	0.690	10	909,364	290
0.521	0.867	10	934,934	291
0.521	0.867	1	206,457	293
0.790	1.156	10	947,212	290

Table B.10: Pressure Drop Comparisons from Counterbore Entrance to Capillary Outlet Corresponding to Profiles for Eccentric Capillaries in Figure 3.46

Distance between capillaries at R_1 and R_2 (mm), **X**	Distance between Counterbore Centerline (mm)	L/D	Pressure at Top of Counterbore (kPa)	Pressure at Top of Capillary (kPa)
0.231	0.400	10	318	308
0.374	0.690	10	319	309
0.521	0.867	10	319	308
0.521	0.867	1	40	31
0.790	1.156	10	318	309